Magnetic and electronic properties of oxides heterostructures probed with x-ray spectroscopy

Inauguraldissertation
zur
Erlangung der Würde eines Doktors der Philosophie
vorgelegt der
Philosophisch-Naturwissenschaftlichen Fakultät
der Universität Basel

von

Anna Zakharova

Basel, 2022

Genehmigt von der Philosophisch-Naturwissenschaftlichen Fakultät

auf Antrag von

Prof. Dr. Frithjof Nolting, Dr. Cinthia Piamonteze, Prof. Dr. Martino Poggio und Prof. Dr. Jean-Marc Triscone

Basel, 21.06.2022

Prof. Dr. Marcel Mayor

Abstract

Fundamental investigation of interfacial properties in complex oxide heterostructures is crucial to boost the development of modern electronics. Coupled degrees of freedom in transition metal oxides (TMOs) provide a rich playground to tailor precisely properties of artificial materials. Yet, entangling complex correlated behaviour is a very challenging task, although it is necessary for heterostructures application.

A variety of x-rays techniques allowed us to build a connection between magnetic properties and the electronic and structural behaviour of TMO as a function of the proximity layer. We applied x-ray absorption spectroscopy (XAS), x-ray magnetic circular dichroism (XMCD), and x-ray linear dichroism (XLD) to probe the magnetic and orbital properties of Mn in ultra-thin $La_{0.7}Sr_{0.3}MnO_3$ in proximity to $SrRuO_3$ in comparison to the interface with $SrTiO_3$. We have revealed the large impact of proximity and dimensionality, resulting in the magnetic dead layer in $La_{0.7}Sr_{0.3}MnO_3/SrRuO_3$ bilayers being drastically diminished. This restoration of magnetism in the ultra-thin $La_{0.7}Sr_{0.3}MnO_3$ layer could be evoked by strong hybridization between $La_{0.7}Sr_{0.3}MnO_3$ and $SrRuO_3$, hindering the quantum confinement effect. The orbital rearrangement at the $La_{0.7}Sr_{0.3}MnO_3/SrRuO_3$ interface, its origin and consequences are discussed. In addition to the strong magnetic and electronic coupling to $SrRuO_3$, the preservation of the mixed-valence and the remaining $d_{x^2-y^2}$ occupation still allows for a strong double exchange coupling in the plane. Based on quantitative analysis and theoretical simulation of the x-ray spectra, the magnetic stability mechanisms in $La_{0.7}Sr_{0.3}MnO_3/SrRuO_3$ are discussed.

Further, we explored phenomena of emerged ferromagnetism in $NdNiO_3$ using x-ray absorption spectroscopy (XAS) and x-ray magnetic circular dichroism (XMCD). When interfaced with $La_{0.7}Sr_{0.3}MnO_3$ we found a net ferromagnetic moment on $NdNiO_3$. Reduction of the layer averaged magnetic moment between 5uc and 10uc $NdNiO_3$ on $La_{0.7}Sr_{0.3}MnO_3$ demonstrated the interfacial nature of the effect. We have found a larger charge transfer between manganite and nickelate layers in compressively strained bilayers. In addition, compressive strain promotes ferromagnetism in the $NdNiO_3$ layer due to superexchange between Mn^{4+}-Ni^{2+} at the interface. On the other hand, films under small tensile strain were demonstrated to have almost no sizeable Mn^{4+}-Ni^{2+} charge transfer.

Resonant x-ray reflectivity reveals a complex coupling with antiferromagnetic components on $NdNiO_3$. It gradually decreases size of the magnetic moment causing still measurable net ferromagnetic moment on $NdNiO_3$. It may originate from antiferromagnetic superexchange between $Ni^{2+/3+}$ and $Mn^{3+/4+}$ planes.

When the manganite layer is insulating ($La_{0.88}Sr_{0.12}MnO_3$), $NdNiO_3$ ferromagnetic ordering is almost quenched. Indeed, the exchange between two insulating layers is blocked suppressing the appearance of ferromagnetism in the NNO layer. At the interface with $La_{0.88}Sr_{0.12}MnO_3$, Ni is in a weakly ferromagnetic or frustrated magnetic phase, in contrast to the Ni in $NdNiO_3/La_{0.7}Sr_{0.3}MnO_3$. By employing resonant x-ray reflectivity we have found different magnetic reconstructions at the $NdNiO_3/La_{1-x}Sr_xMnO_3$ interface.

Summarizing our investigation discovers the role of the proximity layer in TMO heterostructure. By presenting novel experimental data we found complex magnetic behaviour when uniting two dissimilar TMO utilizing x-ray resonant absorption spectroscopy and resonant x-ray reflectivity. We have explored switching between non-magnetic, ferromagnetic and antiferromagnetic phases revealing fine control over the magnetism in bilayers.

Contents

Chapter 1

Introduction: Transition Metal Oxides Based Heterostructures

The continuing increase in demand for more powerful and smaller electronic devices challenges 21st century scientists to develop new materials to replace existing technologies. Spintronics, which stands for spin-based electronics, has a great potential to rebuild a whole field of solid-state electronics to exploit magnetic materials i.e. spin degree of freedom in addition to conventional charge [1, 2, 3]. Magnetic multilayers can be utilized by analogy with semiconductors multilayers, where main functionalities are concentrated at the interface. Major challenges in this field are addressed to the search of suitable materials to create magnetic multilayers and their optimization to compete with efficiency, stability and size of mainstream electronic devices.

In recent years there has been a lot of activities related to magnetic thin films and multilayers based on perovskite transition metal oxides (TMOs) [4, 5], where transition metal is an element with partially filled d orbital. The interest rose due to complexity of their behaviour, and thus tunability of their properties. Phenomena such as metal-to-insulator transition (MIT), superconductivity, colossal magnetoresistance, ferro- and antiferromagnetism etc. are induced by interaction between partially filled d-shell of the transition metal and its oxygen environment [6, 7, 8, 9, 10]. Achievements in synthesis of TMO thin films provided by advanced growth techniques such as Molecular Beam Epitaxy, Pulsed Laser Deposition (PLD) or Magnetron Sputtering enable high-quality and monolayer-precise deposition as well as combination of dissimilar TMOs in one heterostructure with abrupt interfaces.

However, to engineer magnetic properties of the heterostructure it is essential to understand the effects governing the magnetic properties. These consist of interactions within and between the layers. Magnetic properties in 3d TMOs originate from virtual electron hopping (magnetic exchange) between metal cations directly or via oxygen ion

[7, 6, 11]. The competition between numerous correlated effects at the different interfaces reshapes electronic structure of adjacent TMOs via coupled spin, charge and lattice degrees of freedom. It provides great flexibility to configure magnetization and its direction via [12, 5, 13]:

- change in direction, type (antiferro- or ferro-) and strength of the magnetic exchange. It can be tailored by choosing structure of each individual TMOs in heterostructure or surface orientation of the substrate.

- altered interfacial charge transfer between two complex oxides. It occurs to compensate different chemical potential between two TMOs. The classic example of this effect is a manganite-nickelate interface [**?**]. The Ni in $LaNiO_3$ was shown to be strongly affected by $LaMnO_3$ proximity creating net ferromagnetic moment at the interface between paramagnetic and antiferomagnetic perovskites. The charge transfer phenomena is normally restricted to the interface.

- different lattice mismatch between adjacent TMO layers and the substrate octahedral distortions and rotations, which in an epitaxial grown layer leads to a strain imposed on the transition metal thin film. The strain effect is typically maintained within tens of nanometers. In addition, strain can modify d orbital polarization in the thin films possibly leading to changes in magnetism. It may result in a competition between ferromagnetic and antiferromagnetic ordering as a function of strain as it occurs in lanthanum manganites [14]. In addition to strain, octahedra rotation and distortion can be induced by symmetry mismatch. It occurs to maintain corner connectivity of BO_6 octahedra. Unlike strain this effect is maintained within a couple of unit cells. The influence on magnetism was shown by different rotation patterns in $LaMnO_3/SrTiO_3$ superlattices for instance [15].

- d orbital reconstruction. In contrast to orbital polarization due to the strain this reconstruction originates from orbital coupling between adjusted TMO layers resulting in different orbital occupancy between non-interfacial region and the interface. As demostrated in $BiFeO_3/La_{0.67}Sr_{0.33}MnO_3$ (LSMO33) interfacial ferromagnetism arises as a consequence of orbital rearrangement between antiferromagnetic and ferromagnetic TMO [16].

- symmetry breaking and orbital reconstruction effects. They can be provoked by reduced dimensionality of the heterostructrue. It was shown to move $LaNiO_3$ from being paramagnetic in bulk to become rather antiferromagnetic in a thin film of several monolayers [17, 18].

Obtaining reliable information on properties of low-dimensional magnetic heterostructures and understanding of driving forces are key points in the development of new magnetic materials and their implementation. The interplay between mechanisms presented above and its impact on magnetism in heterostructures were explored in this work by employing element selective techniques such as x-ray absorption spectroscopy (XAS) and resonant x-ray reflectivity (RXRR). Main probes were polarization dependant XAS techniques: x-ray magnetic circular and linear dichroism (XMCD and XLD respectively) enabling to investigate charge, orbital and spin degrees of freedom. In addition to XMCD, resonant x-ray magnetic reflectivity (RXMR) enables layer-by-layer examination of magnetism and structure. Detailed description of each experimental technique, experiment design and data fitting procedure are given in Chapter 3.

The main focus of this thesis are magnetic heterostrutures in form of bilayers. In Chapter 5 we address the origin of extraordinary magnetic stability in bilayers based on LSMO33 and $SrRuO_3$ (SRO). $La_{1-x}Sr_xMnO_3$ (LSMO) has diverse magnetic and electrical properties caused by Sr doping variation. The Sr content of x=0.33 is the most studied doping of LSMO. It attracted a lot of attention due to its half-metallic behaviour and colossal magneto-resistance effect. In addition, LSMO33 has relatively high ferromagnetic moment per Mn atom and transition temperature of 360K in bulk that makes it an excellent candidate for application. In the form of ultra-thin film its utilization, however, is limited due to quenching metal-to-insulator transition and loss of its ferromagnetic properties. Experimentally, SRO layer was found to stabilize magnetism in ultra-thin manganites down to few monolayers. We clarified correlation between such a change in magnetic properties and orbital and charge rearrangement based on quantitative analysis and theoretical simulation of the x-ray spectra.

Chapter 6 of this work aims to elucidate emergent ferromagnetism in usually antiferromagnetic $NdNiO_3$ (NNO) in proximity to LSMO as a function of strain, thickness and LSMO doping. NNO belongs to a family of rare-earth nickelate compounds featured by sharp metal-to-insulator transition. NNO has a special point in a phase diagram, where three different phases meet. Therefore its properties are extremely sensitive to any external change. Despite having AFM ordering in bulk Caputo *et al.*[19] has discovered MIT modification and ferromagnetic ordering in NNO induced by LSMO33 proximity. In the first part of this chapter we extend this research to study emergent ferromagnetism in NNO as a function of strain and NNO thickness to uncover nature of Ni magnetic behaviour. Thickness study on both type of substrates is crucial to understand if the observed Ni magnetism is purely interfacial phenomena. $NdGaO_3$ (NGO) and $LaAlO_3$ (LAO) substrates were chosen to induce compressive and tensile strain in NNO respectively.

In the second part of Chapter 6 ferromagnetic metal LSMO33 was replaced by ferromagnetic insulator $La_{0.88}Sr_{0.12}MnO_3$ (LSMO12) to study a comparison between NNO/LSMO33 and NNO/LSMO12 interfaces both on NGO substrate. The motivation of this study was to change from a metal to an insulator as proximity layer and see if this interferes with the magnetism of NNO. It has been shown earlier that in manganite-nickelate heterostructure magnetism is strongly affected by interfacial charge transfer. Therefore, reducing the content of Sr (Mn^{3+}) in LSMO should also have a direct influence on interfacial charge transfer and orbital reconstruction, i.e. magnetism. In this work evolution of the Ni magnetic behaviour as a function of LSMO doping helps to address complex origin of NNO magnetism. In addition, NNO layer thickness has been varied in order to identify mutual impact on magnetism and to compare with similar thickness dependence on NNO/LSMO33.

In Chapter 7 all results are summarized and main findings are highlighted. In order to make the reading of thesis easier in page 108 we have a list of all abbreviations and in page 110 we have a summary of the films composition with their respective names.

Chapter 2

Materials

In this chapter 3d TMO introductory concepts are presented regarding their structural, electronic and magnetic properties. Furthermore, theoretical and experimental background with focus on three particular compounds: LSMO, SRO and NNO is included in the three sections of this chapter respectively.

2.1 TMO perovskites basic concepts

Transition metal oxides (TMO) contains element with partially filled 3d: Ni, Mn, Ti..; 4d: Ru, Nb..; or 5d: Ir, Pt...The TMO perovskites are characterized by ABO_3 chemical formula, where the transition metal cation occupies the B-site forming BO_6 octahedra with six O^{2-} ions. The interstitial A-sites are occupied by a rare-earth or an alkaline earth metal, whose oxidation state determines the electron count on the B-site transition metal. The ideal perovskite has cubic $Pm\bar{3}m$ with a=b=c lattice constants. An example of cubic perovskite is $SrTiO_3$ (STO) at room temperature (RT), which is commonly used as a substrate for heterostructure synthesis. The 3d orbitals in an isolated TM atom consists of five degenerate states, whereas in a cubic crystal field TMO 3d and the O 2p electrons experience Coulomb repulsion lifting fivefold degeneracy (Fig. 2.1). In the case of an octahedral environment the 3d levels are split in lower t_{2g} (t_{xy}, t_{xz}, t_{yz}) and higher e_g (e_{x2-y2}, e_{3z2-r2}) orbitals by the crystal field splitting 10Dq. Owing to the Hund's rule of maximizing total spin value every electron occupies a single orbital until all orbitals are singly occupied and then continues with pairing of opposite spins. This is the so-called high-spin state. However, if the 10Dq crystal field splitting is too large, the high-spin state is not energetically favorable and a "low-spin" state becomes the ground state (Fig. 2.2).

Even though perfect perovskite is cubic, most perovskites are distorted and lower crystal symmetries are found. Structural transformation occurs upon changing the ion

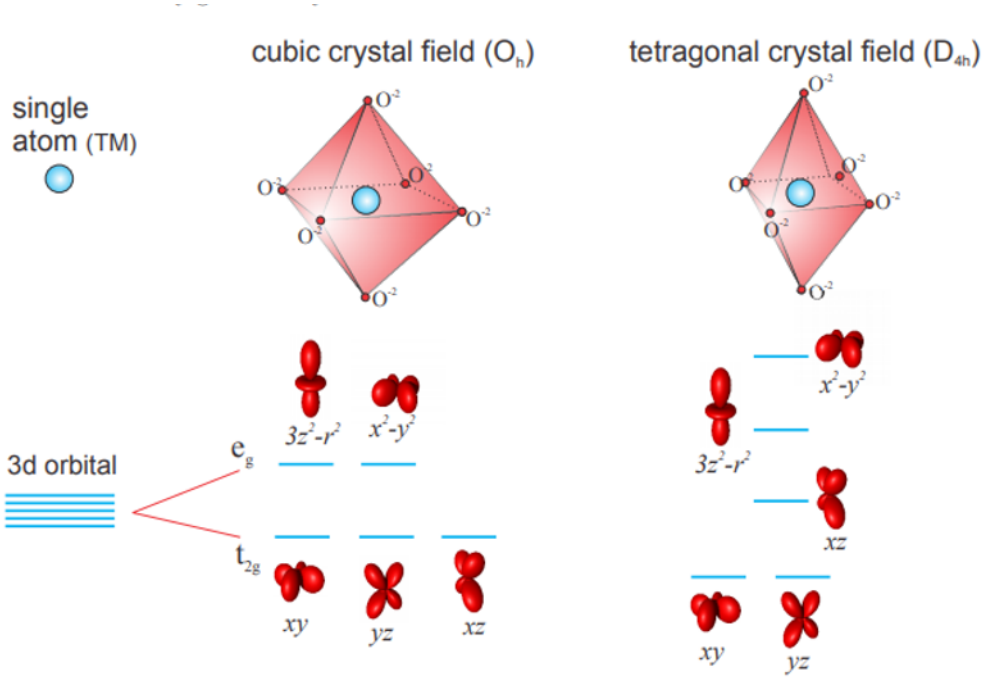

Figure 2.1: The lifting of the degeneracy of the five d-orbitals when placing the TM ion inside a regular octahedra with O ions at the corners (left) and a tetragonally distorted octahedra (right). Figure is taken from [20].

size. Such a change can be quantified by tolerance factor t:

$$t = \frac{(r_A + r_O)}{\sqrt{2}(r_B - r_O)} \tag{2.1}$$

where r_A, r_O and r_B are ionic radii of each element in ABO_3 and t=1 corresponds to the perfect cubic perovskite structure.

Another factor to affect perovskite structure is orbital filling. Having single electron on e_g level supports Jahn-Teller effect caused by tendency of the system to lower its energy by tetragonal distortion. Such a Jahn-Teller ion (Mn^{3+} and Ni^{3+} for instance) has lifting of the degeneracy of t_{2g} and e_g orbitals as shown in Fig. 2.1(right). Thus, Jahn-Teller distortion elongates or compresses TM-O distance in one direction [7, 6].

One expect free atom with a half filled band to be metallic. However, TMO oxides often are insulators. Metallic state can be described by effective electron hopping of the electron from one to the other occupied site. In TMOs it can occur between d orbitals, hence the excitation energy needed for electron-electron transfer $d_n d_n \rightarrow d^{n-1} d^{n+1}$ is given as U_{dd}. Insulating state occurs when U_{dd} overpowers hoping amplitude t quantifying the probability of an electron occupying adjacent sites. This insulating state is called Mott-Hubbard insulator featuring compounds with early 3d metals such as V or Ti.

In addition to the d-d electron excitation in the oxides interaction between full O 2p

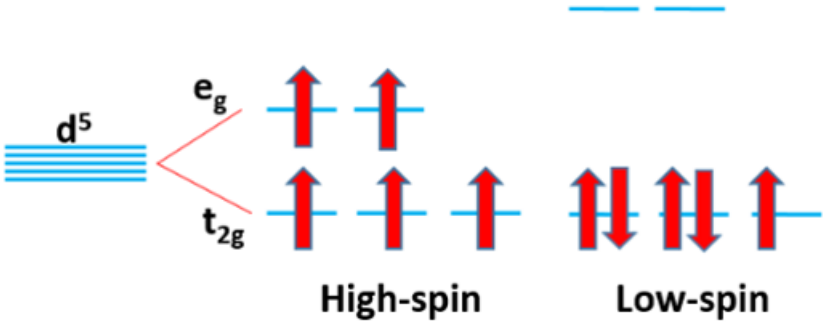

Figure 2.2: Possible high and low-spin configurations for five electrons on d orbital (d^5).

(ligand) and half-full 3d TM should be included. The direct overlap between d-d orbitals often is small and effective hopping occur through intermediate oxygen. Energy difference between initial and final states $d^n p^6 \rightarrow d^{n+1} p^5$ is denoted as charge-transfer energy Δ_{ct}. Extra hole on the ligand is denoted as $d^{n+1}\underline{L}$. If $U > \Delta_{ct}$, then the system can be called charge-transfer insulator. The charge-transfer insulator functions for heavy 3d elements. In the heavy 3d elements with a high valence Δ_{ct} can be very small or even negative as in the case of Ni^{3+}. Owing to negative Δ_{ct} Ni^{3+} is better represented by $Ni^{2+}\underline{L}$ state. Negative Δ_{ct} is likely to happen for 4d and 5d elements as in the case of Ru based oxides [7, 8].

Next, we will discuss the different types of magnetic ordering in these systems. Magnetism originates from the local interatomic spin arrangement as a consequence of Coulomb repulsion. The magnetic interaction can be described by Heisenberg Hamiltonian as:

$$H = -2J_{ij}s_i s_j \tag{2.2}$$

that expresses an electron-electron interaction between two magnetic spins s_i and s_j. J_{ij} is the exchange energy. Positive value of the exchange energy yields a ferromagnetic alignment of the spins, whereas negative value results in an antiferromagnetic alignment [11].

The simplest scenario of the exchange interaction is a direct exchange. It is a ferromagnetic exchange arising from a direct electron hopping between metal cations [21]. However, in TMO the direct overlap between d orbitals is negligible and hybridization between metal 3d and oxygen 2p orbitals allows virtual electron hopping from one ion to another via non-magnetic neighboring oxygen in so-called indirect exchange. The exchange sign (ferromagnetic (FM) or antiferromagnetic (AF)) is governed by Pauli exclusion principles between metal cation and O^{2-} ion. In turn, it depends on relative d orbital occupation of the metal cations and B-O-B bond angle. Additionally, the strength of the exchange interaction is influenced by the orientation of occupied d orbital.

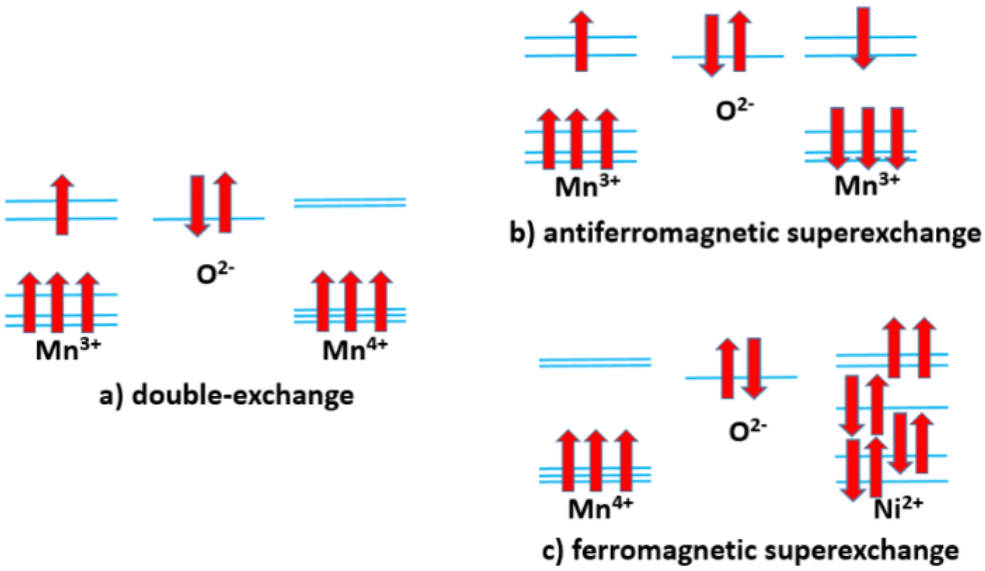

Figure 2.3: Types of magnetic indirect exchange: a) double-exchange between Mn^{3+} and Mn^{4+} cations, superexchange between b) two Mn^{3+} ions and c) between Mn^{4+} and Ni^{2+} .

Introduced by Zener the double-exchange (DE) occurs in doped TMO compounds between transition metal ions of the same kind in different valence state [22]. This exchange is always strongly FM, because electron hopping between one electron and empty orbital via oxygen occur without spin flip to satisfy the Hund's rule (Fig. 2.3(a)). The hopping probability of the electrons depends on the d orbitals overlap, orthogonal orbitals have zero hopping probability (for instance between d_{3z2-r2} and d_{x2-y2}). DE also produces high conductivity .

A more general case of indirect exchange introduced by Kramers is superexchange (SE) [23]. Straightforward rules were derived by Goodenough and Kanamori to predict the sign of the SE following Pauli exclusion principle [24, 25, 26]. From the Goodenough-Kanamori rule (GKR) exchange between two half-filled orbitals would be strongly AF, whereas exchange between half-filled and empty or filled and half-filled orbitals would be FM (Fig. 2.3 (b,c)). However, it is true only when the angle between cation orbitals is nearly 180°. In a special case of SE with metals connected at 90° SE would be weakly FM [7, 27].

In the Heisenberg Hamiltonian of Eq. (2.2) energy seems to be independent of the magnetization direction. Nevertheless, in ferromagnets all spins tend to align with respect to the preferential crystalline axis and/or to the external shape of the body, which is most energetically favorable for spontaneous magnetization. Small relativistic corrections to the Hamiltonian due to the dipole-dipole interaction and spin-orbit coupling give rise to so-called magnetic anisotropy. It arises from a combination of several factors:

shape anisotropy due to the form-dependent demagnetizing field and magneto-crystalline anisotropy due to crystalline symmetry together with spin-orbit coupling [28].

So far only bulk properties of TMO materials were described. However, physics of thin films differs from that of the bulk and needs to be specified. In a epitaxial growth the thin film follows the crystal structure of the substrate. An epitaxial growth implies low mismatch between the lattice parameter of the film a_{film} and that of the substrate a_{subs} along in-plane direction. The strain can be introduced as $\epsilon = (a_{sub} - a_{film})/a_{film}$ and can be tuned from in-plane compressive ($\epsilon < 0$) to in-plane tensile ($\epsilon > 0$) state affecting TM-O bond. The unit cell stays constant so a compressive/tensile strain in-plane implies that the out-of-plane distances go to the other direction, which causes a break in the symmetry of the the TM-O bonds and orbitals. Compressive/tensile strain lifts the degeneracy of t_{2g} and e_g orbitals leading to a tetragonal distortion as exemplified in Fig. 2.1 lowering in energy in-plane (out-of-plane) orbitals for in-plane tensile (compressive) strain. Such a change in TM-O distance results in altered magnetic properties in comparison to the bulk [13, 9]. Moreover, different strain state affects magneto-elastic anisotropy through the spin-orbit coupling favoring specific direction of the magnetization [28].

2.1.1 $La_{1-x}Sr_xMnO_3$

Mixed valence manganite $La_{1-x}Sr_xMnO_3$ (LSMO) is a large family of oxides, where a rich variety of phases were discovered as a function of La and Sr doping. Variation of La and Sr substitution controls content of electrons and holes respectively, i.e Mn^{3+} /Mn^{4+} ratio. The electronic configuration for Mn^{3+} is $t_{2g}^3\ e_g^1$ with total spin S = 2 and for Mn^{4+} is $t_{2g}^3\ e_g^0$ with S = 3/2. As a consequence, LSMO is a perfect compound to illustrate different indirect exchange interactions below the magnetic ordering temperature. The competition between AF SE and FM DE exchange mechanisms takes place in LSMO owing to relative $3d^4$ Mn^{3+} and $3d^3$ Mn^{4+} content. In a bulk, transition from FM double-exchange between $3d^4$ Mn^{3+} and $3d^3$ Mn^{4+} to AF typically occurs at 50%:50%, where the negative superexchange between two $3d^3$ Mn^{4+} ions start to prevail (Fig. 2.4) [13, 10, 29]. Strong DE in LSMO is typically accompanied by metallicity. LSMO was found to be metallic for $0.2 < x < 0.5$ and insulating otherwise.

In thin films, strain imposed by the substrate affects orbital polarization and thereby the magnetic state of LSMO. The preferential occupation of the d_{x2-y2} orbitals induced by tensile strain allows for FM in-plane interactions between full and empty d_{x2-y2} states and AF out-of-plane interactions between full t_{2g} states resulting in A-type antiferromagnetism. In contrast, d_{3z2-r2} preferential occupation induced by compressive strain promotes out-of-plane FM interactions and in-plane AF interactions, leading to C-type

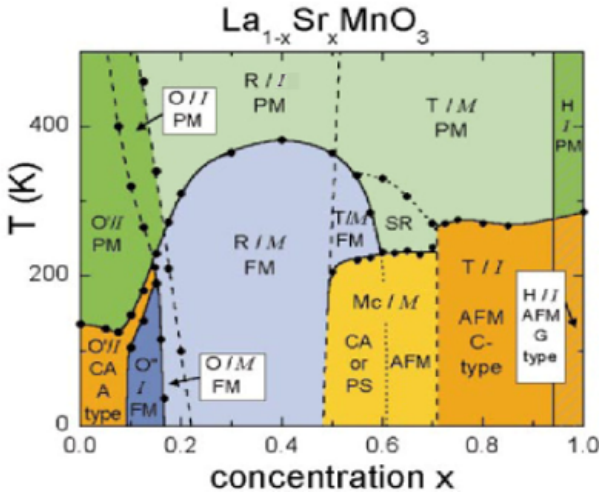

Figure 2.4: T_C Temperature versus LSMO doping. Figure is taken from [29].

antiferromagnetism. The magnetic phases produced by different combinations of LSMO composition and strain states are summarized in Fig. 2.5 [14]. The suppression of DE in one direction affects transport properties of the films.

In Chapter 5 and 6 LSMO33 (x=0.33) was employed as a part of LSMO/SRO and NNO/LSMO heterostructures. LSMO33 exhibits the highest Curie temperature among the manganites (370K) with a $3.2\mu_B$/Mn and metallic state below T_C. Moreover, LSMO33 exhibits colossal magneto-resistance (CMR) effect. The CMR effect is related to a change of its transport properties under external magnetic field [30]. Since the ferromagnetism in this system is driven by DE, which creates a link between ferromagnetism and metallicity.

The magnetism and transport in thin films are altered due to reduced dimensionality and applied stress. In this work LSMO33 thin film was deposited on three types of substrates: STO(001), LAO(100) and NGO(110). LAO and NGO have a similar effect on LSMO33 inducing compressive strain. However, NGO places LSMO33 magnetic easy axis in-plane, while LAO places LSMO33 magnetic easy axis out-of-plane. In contrast to NGO and LAO, STO substrate generates tensile strain with magnetic easy axis in-plane (Tab. 2.1) [31].

Another fascinating state of LSMO appears in a low-doping region x=0.12 (LSMO12), where the exotic ferromagnetic insulating phase is established below T_c=200K [30, 32].

Additional feature of the LSMO12 is charge ordering (CO) state that was observed to occur around T_{co}=160K between paramagnetic to ferromagnetic transition. Formation of CO is closely associated with lattice deformation by structural phase transition.[33, 34, 35, 36]

For thin film LSMO12 reduced thickness was shown to lower T_C to 80K. The lower value of magnetic moment $2\mu_B$ was found in comparison to LSMO33 [37]. The absence

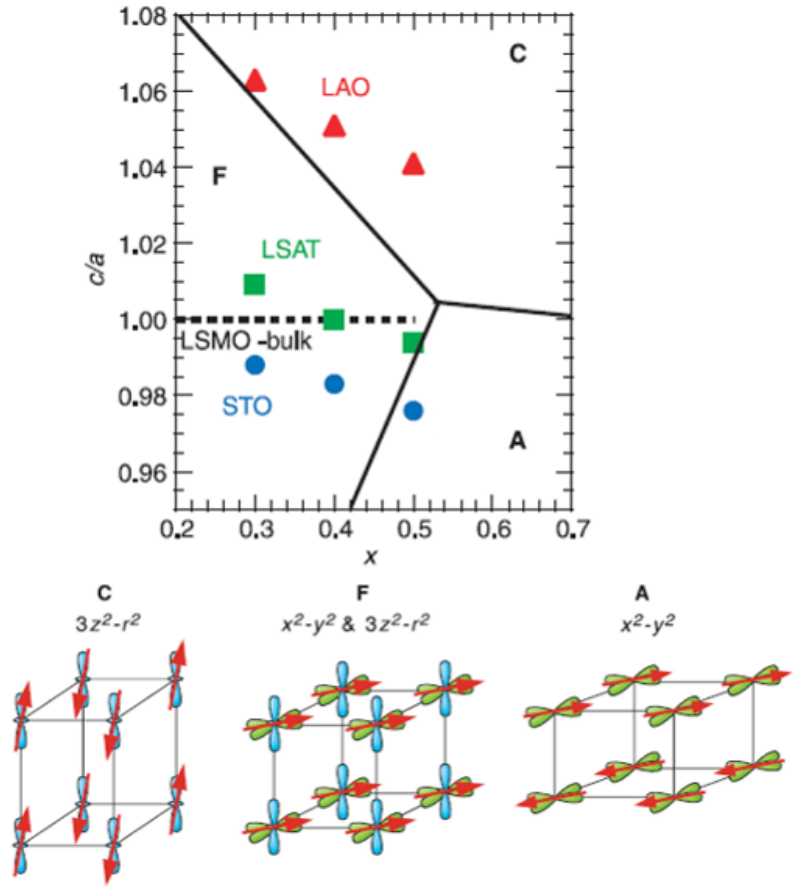

Figure 2.5: Various magnetic states realized as a function of LSMO strain and Sr doping. Figure is taken from [14].

of CO transition was experimentally demonstrated for LSMO12 film under compressive strain [38]. In Chapter 6 LSMO12 was used as proximity layer to a thin layer of NNO on NGO susbstrate. Similar to LSMO33 NGO substrate induces compressive strain on LSMO12 (Tab. 2.1).

Further details on LSMO33 and LSMO12 thin films will be uncovered in Chapter 5 and 6 of this thesis.

2.1.2 $SrRuO_3$

Another remarkable example of TMO is $SrRuO_3$. It is a highly conducting metal that is very often used as an electrode and represents the only known 4d ferromagnet. SRO has orthorhombic structure and ferromagnetic transition occurring at around 160K with reported magnetic moment of $1.6\mu_B$ in bulk. As opposed to other 3d materials presented in this chapter Ru is a 4d compound having more itinerant character. At the same time, 4d elements present stronger spin-orbit coupling, and therefore stronger magneto-

Table 2.1: Strain state derived as $\epsilon = (a_{sub} - a_{bulk})/a_{bulk}$ for used films and substrates with corresponding in-plane cubic lattice constants a_{bulk} and a_{sub} respectively [31, 38, 39, 40]

film	STO (3.905)	NGO (3.858)	LAO (3.789)
LSMO33 (3.892)	0.33%	-0.8%	-2.6%
LSMO12 (3.915)	•	-1.4%	-3.2%
SRO (3.903)	-0.64%	•	•
NNO (3.803)	•	1.5%	-0.4%

crystalline anisotropy. More extended nature of 4d orbital causes itinerant character of SRO ferromagnetism in addition to a strong hybridization between Ru 4d and O 2p. Due to a large crystal field splitting Ru^{4+} is expected to be in a low spin state t_{2g}^4 [41, 42]. Furthermore, SRO ground state is characterized by $d^5\underline{L}$ rather than d^4 owing to negative charge transfer value [43].

In thin films SRO undergoes thickness-driven MIT that occurs at 4uc becoming non-magnetic Mott insulator below this thickness. In addition, the electronic configuration of SRO film is influenced by epitaxial strain bringing one of the d_{yz}, d_{xz} (d_{xy}) level lower in energy for compressive (tensile) strain [44, 45, 46, 47]. Despite the most probable low-spin configuration of Ru, there has been many attempts to stabilize high-spin state of Ru in order to enhance SRO magnetism. The high-spin state $t_{2g}^3 e_g^1$ of Ru was successfully demostrated for compressive (110) oriented film in contrast to compressive SRO (100) [48].

SRO deposited on STO(001) was used in Chapter 5 as a proximity layer to ultra-thin LSMO33, where SRO is in compressive strain state with out-of-plane magnetic easy axis (Tab. 2.1).

2.1.3 $NdNiO_3$

The NNO belongs to rare-earth perovskite nickelates family $RNiO_3$ (RNO) (Fig. 2.6), where R= La, Pr, Nd, Sm...Lu. The RNO family sparked an enormous interest in the scientific community due to an early prediction of superconductivity [50]. The rich phase diagram of RNO can be described by structural transformation upon changing the size of rare-earth ion. Such a change can be quantified by tolerance factor t from Eq. (2.1) or equally by the deviation of Ni-O-Ni angle away from 180°. The RNO family is characterized by t<0.94, because R is not large enough to accommodate in a cubic unit cell. The RNO symmetry is lowered to rhombohedral ($R\bar{3}c$), then to orthorhombic (Pbnm) down to monoclinic ($P2_1/n$) structure upon decreasing t. At the same time, deviation of Ni-O-Ni angle from 180° reduces the overlap between Ni 3d and O 2p promoting insulating

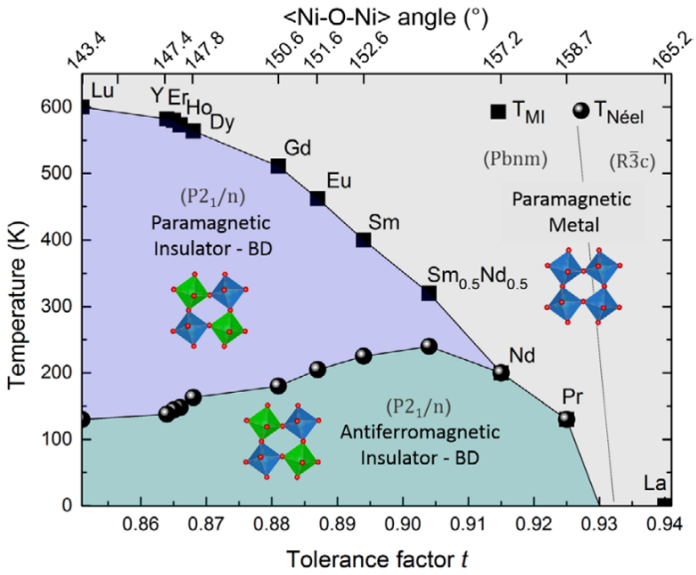

Figure 2.6: RNO phase diagram illustrating evolution of structure, magnetism and transport properties as a function of temperature, tolerance factor and Ni-O-Ni angle. Figure is taken from [49].

state over the metallic. Whereas $LaNiO_3$ remains in paramagnetic (PM) metallic state, other members of RNO undergo sharp MIT and PM-AF Néel transition accompanying structural transformations. The structural, transport and magnetic properties of RNO as a function of t and Ni-O-Ni angle are summarized in Fig. 2.6.

Formally, in all RNO compounds Ni is in 3+ valence state with 7 electrons in the d shell. Ni is in low spin state with a configuration $t_{2g}^6\ e_g^1$. However, RNO family was shown to have a negative value of charge transfer changing Ni ground state to admixture of Ni^{3+} d^7 and Ni^{2+} $d^8\underline{L}$. Such a occurrence of the holes at O 2p is referred as self-doping. Although Ni^{3+} is expected to be Jahn-Teller active, no experimental evidence of such a distortion was observed. Instead, charge ordered or charge disproportional ground state has been revealed by diffraction experiments varying valence state from site to site in the form $Ni^{3+\delta}$-$Ni^{3-\delta}$ [51, 52, 53].

Nd and Pr are the only R ions, where MIT and Néel transition coincide. Below T_N AF ordering in insulating phase can be formed by non-collinear ($\uparrow\rightarrow\downarrow\leftarrow$) stacking planes with four monolayer periodicity along (111): $q_{Bragg} = (1/4\ 1/4\ 1/4)$ in pseudocubic (pc) or $(1/2,\ 0,\ 1/2)_{or}$ in orthorhombic notation. It occurs as a result of competition between equal number of ferromagnetic and antiferromagnetic exchange interactions [54, 55, 56, 49, 57].

The heterostructure in Chapter 6 contains RNO with R=Nd, where $T_N = T_{MIT} =$ 200K in bulk. In thin films the NNO transition temperature can be tailored by imposing different epitaxial strain: from tensile to compressive, the MIT transition of NNO films

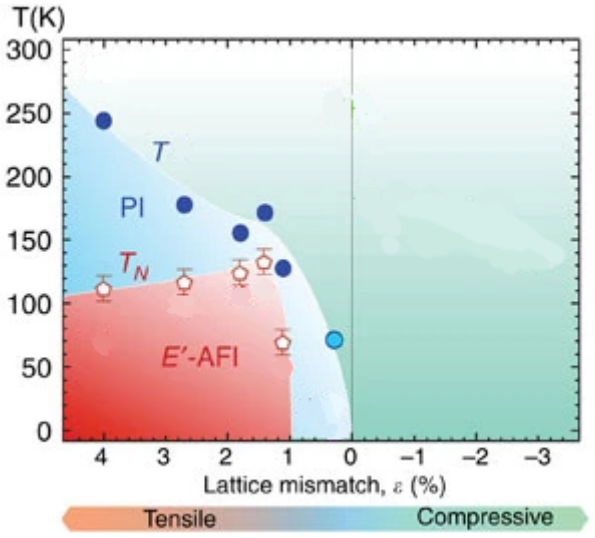

Figure 2.7: NNO (110) thin film phase diagram as a function of temperature and lattice mismatch. Closed blue and open red circles indicate T_{MIT} and T_N respectively. Green area of the phase diagram corresponds to spin-disordered non-Fermi-liquid behaviour, red area to AF and blue area to PM. Figure is adapted from [39].

shifts to low temperatures quenching the MIT at large compressive strain [58]. The evolution of T_{MIT} is illustrated in Fig. 2.7 by blue closed circles. This effect on MIT is accompanied by phase separation of T_N and T_{MIT} and magnetic ordering degradation ending in a spin-disordered state (green area in Fig. 2.7). In general, significant decrease in T_N in thin films was observed [39].

In Chapter 6 NNO was deposited on LAO (100) and NGO $(110)_{or}$ substrates. LAO introduces compressive strain on NNO, whereas NNO on NGO is tensile (Tab. 2.1).

Chapter 3

Synchrotron techniques and Instrumentation

In this work we mostly focused on using synchrotron techniques for material study. Low concentration, different composition and complex behaviour of TMOs impose certain limits on investigation of the thin films. X-ray absorption spectroscopy (XAS) has become one of the fundamental techniques to address local geometry or electronic structure in such systems. As a main advantage XAS enables separated study of each element in the heterostructure by tuning the energy of incident photons to correspond to a binding energy of electrons of the probed element (atomic absorption edge). In this work x-rays were tuned in a soft regime to reach the $L_{2,3}$-edge of transition metals and the K-edge of oxygen allowing to probe the unoccupied states of 3d valence shell and the 2p shell, respectively. By selecting polarization of the x-rays: circular for x-ray magnetic circular dichroism (XMCD) and linear for linear dichroism (XLD), different XAS techniques can be realized to determine spin, orbital and charge configuration in heterostructure specifically for each element. Further, XAS can be combined with specular reflectivity (resonant x-ray reflectivity, RXRR) to gain information on structural parameters such as density, thickness and roughness of each individual layer. Using circular polarization, information on magnetism can be accessed similarly to XMCD by resonant x-ray magnetic reflectivity (RXMR), but with layer-by-layer precision.

This chapter is dedicated to a description of implemented techniques including approach to data analysis, data interpretation and a description of the experimental setup.

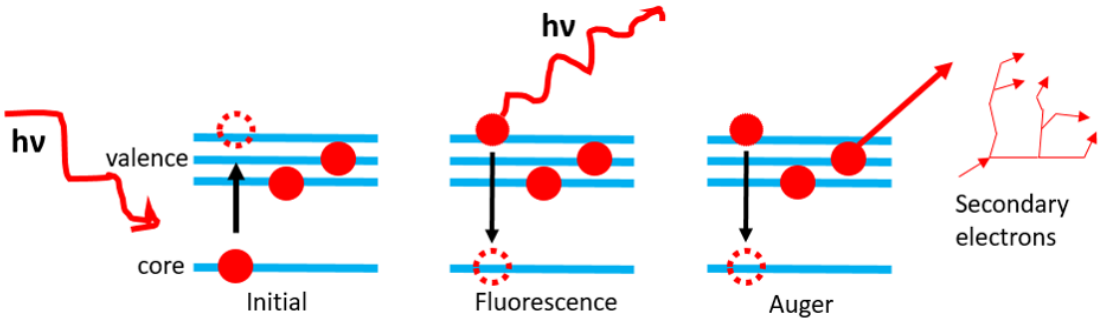

Figure 3.1: The initial event of photoexcitation and subsequent de-excitation events: fluorescence, Auger and secondary (inelastically scattered) electrons emission.

3.1 X-Ray Absorption

Experimentally, when interacting with matter intensity of incoming x-rays I_0 decay exponentially:

$$I = I_0 e^{-\mu t} \tag{3.1}$$

where t is the sample thickness, μ is the absorption coefficient and I is the intensity of transmitted x-rays. The μ is specific for each element number Z. Therefore XAS technique measures absorption coefficient as a function of energy giving x-ray absorption (XA) spectrum.

In the x-ray absorption event core electrons are excited to unoccupied states (resonant absorption process) or to the continuum (non-resonant absorption process) followed by one of the de-excitation processes: emission of photons, Auger or secondary electrons (Fig. 3.1). Non-resonant absorption process contributes to the background intensity of the spectra, while resonant process causes a jump in the absorption coefficient corresponding to an absorption edge. In turn, the absorption intensity is proportional to the density of unoccupied states (holes h). Thus, the integrated XAS intensity I is derived as:

$$I = Ch \tag{3.2}$$

where C is a proportionality constant. The proportionality of the x-ray absorption intensity with the number of holes is well represented in Fig. 3.2 for the x-ray absorption of metals with different number of electrons on d level.

From the theoretical point of view, the μ absorption coefficient is proportional to the absorption cross-section σ. The absorption cross-section σ is defined as a measure of the probability of interaction between photons with the material via photoabsorption normalized by the incident photon flux Φ_0 [11]:

$$\sigma = \frac{P_{fi}}{\Phi_0} \tag{3.3}$$

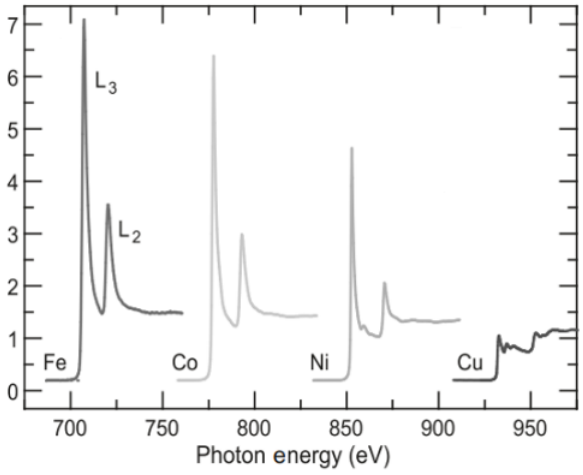

Figure 3.2: Examples of XAS at $L_{2,3}$-edges for Fe, Co, Ni and Cu. Figure is taken from [11].

where P_{fi} is the transition probability from initial state $|i\rangle$ to a final state $|f\rangle$. P_{fi} can be expressed by Fermi golden rule with density of the unoccupied final states $\rho(E_f)$ as:

$$P_{fi} \propto |\langle f|H_{int}|i\rangle|^2 \rho(E_f) \tag{3.4}$$

where H_{int} is the time-dependent perturbation that drives the electronic transition. H_{int} can be simplified in a framework of dipole approximation. Dipole approximation assumes that the size of the absorbing atom shell is small relative to the x-ray wavelength, which drives the electronic transition over the atomic volume. This is a reasonable approximation in soft x-rays because λ is $\lambda \approx$1.2nm and $|\vec{r}| \approx 0.01$nm, so $|\vec{r}| << \frac{1}{|\vec{k}|} = \frac{\lambda}{2\pi}$. Then P_{fi} can be rewritten as:

$$P_{fi} \propto |\langle f|\vec{\varepsilon}\vec{r}|i\rangle|^2 \rho(E_f) \tag{3.5}$$

with polarization dependant dipole operator $\vec{\varepsilon}\vec{r}$. Resulting intensity depends on x-ray propagation direction with respect to to the electron orbit and electric polarization ε of x-rays. The photon transfers angular momentum $q\hbar$ to the electron, where q = 0 refers to linear polarized light while q = +1 and q = -1 refer to c+ and c- circularly polarized light.

In dipole approximation the allowed transitions to unoccupied states follow quantum mechanical dipole selection rules, where orbital quantum number difference between initial and final state is Δ l=$\pm$1 and Δ s=0. It implies that by choosing the excited level, one also chooses which band to probe. It explains our interest mostly in measuring p$\rightarrow$d transition known as $L_{2,3}$ edges probing valence d orbital of the transition metals and 1s$\rightarrow$2p transition known as K-edge probing O 2p orbital involved in hybridization with the metal.

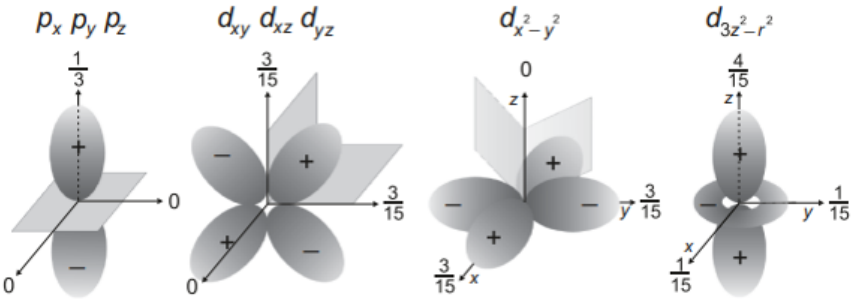

Figure 3.3: Polarization dependent core to valance transition intensities for $\vec{E}$ along the principal coordinate axes. Listed are the intensities for the four basic symmetry cases: p→d_{ij} (i≠j = x, y, z), p→d_{x2-y2} and p→d_{3z2-r2}. Figure is taken from [11].

Due to spin-orbit coupling 2p level splits into two levels corresponding 2p ($j = |l \pm s|$): $p_{\frac{1}{2}}$ and $p_{\frac{3}{2}}$. They are reflected as two peaks in XAS intensity in d spectrum corresponding to L_2 and L_3 edges with branching ratio 1:2 [11].

3.2 X-Ray Linear Dichroism

The absorption process is polarization-dependant as can be seen from Eq. 3.5. Linearly polarized x-rays interacts with non-spherical charge distribution around the absorbing atom probing the unoccupied states along electric field vector $\vec{E}$. XLD spectra is obtained as a difference between two XA spectra measured with two orthogonal x-ray linear polarizations.

For TMOs and especially in strained thin films, we are usually interested in probing d orbital occupation in non-cubic crystal field. Let us look into detail of how the p-d transition looks like when considering the different d orbital symmetries in a cubic crystal field. There are three p orbitals: p_x, p_y, p_z, where p→d transition can be initiated by three orthogonal polarization direction x,y and z to five d orbitals (3x5=15 possible transitions in total). Transition probability is equal to zero for orbitals orthogonal to $\vec{E}$ and non-zero for orbitals parallel to $\vec{E}$. Therefore the polarization-dependant transition probability $\langle p_x|x|d_{x^2}\rangle$ and $\langle p_y|y|d_{y^2}\rangle$ have intensity of 3/15, whereas transition probability $\langle p_z|z|d_{3z^2-r^2}\rangle$ has 1/15 intensity (Fig. 3.3). The intensity ratio of 3:1 is a result of x/y polarized light inducing transition to both $x^2 - y^2$ and $3z^2 - r^2$, while z polarized light enabling transition only to $3z^2 - r^2$ [11, 59, 60].

Finally, for a system with tetragonal symmetry D_{4h} XA integrated intensity along x, y and z directions can be written for all possible 2p→3d transitions with h number of

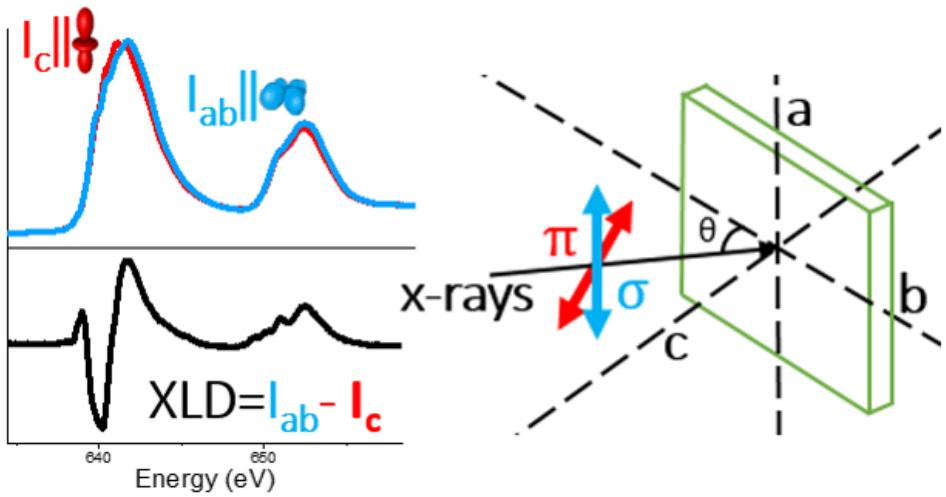

Figure 3.4: (right) Geometry of the XLD experiment in grazing with $\vec{E}$ (σ and π polarization) parallel to two crystallographic axis c and ab and (left) corresponding XA and XLD intensity at Mn $L_{2,3}$-edge.

holes [61]:

$$I_x = I_y = \frac{1}{h}(\frac{1}{2}h_{xy} + \frac{1}{2}h_{xz} + \frac{1}{6}h_{3z^2-r^2} + \frac{1}{2}h_{x^2-y^2}) \tag{3.6}$$

$$I_z = \frac{1}{h}(\frac{1}{2}h_{xz} + \frac{1}{2}h_{yz} + \frac{2}{3}h_{3z^2-r^2}) \tag{3.7}$$

Therefore the hole distribution on e_g level for Mn^{3+} ion with a single electron on e_g can be approximately represented by the ratio X defined as:

$$X = \frac{h_{3z^2-r^2}}{h_{x^2-y^2}} \approx \frac{3I_c}{4I_{ab} - I_c} \tag{3.8}$$

Expression (3.8) allows a quantitative relation of XLD spectra measured with linear polarization parallel to z ($\|I_c$) and x($\|I_{ab}$). The XLD spectra is then defined as XLD=I_{ab}-I_c that is illustrated in Fig. 3.4.

In grazing geometry (Fig. 3.4(right)), the measurement with linear horizontal (σ polarization) corresponds directly to I_{ab}. The linear vertical (π polarization) polarization contains both I_c and I_{ab} components. In order to obtain I_c we can disentangle the components by the expression:

$$I_c = \frac{I_\pi - I_\sigma sin^2 30°}{cos^2 30°} = \frac{4}{3}(I_\pi - \frac{1}{4}I_\sigma) \tag{3.9}$$

We have discussed so far the linear dichroism resultant from charge anisotropy. It is called x-ray natural linear dichroism (XNLD). Furthermore, x-ray magnetic linear dichroism (XMLD) probes magnetism below the magnetic orderding temperature (T_N or T_C) of the sample. It is possible due to deformation of the charge relative to the magnetization

of the sample via spin-orbit coupling and exchange interaction [11, 62, 63]. Asymmetrical absorption arises from the difference between measurements parallel and perpendicular to the magnetization. The XMLD intensity is propotional to the square of magnetic moment $I_{XMLD} \propto \langle \vec{m}^2 \rangle$. The XMLD technique is featured by the ability to detect antiferromagnetic ordering unlike XMCD technique explained in the Section 3.3.

3.2.1 Multiplet XLD simulations using CTM4XAS software

The one-electron approximation given in the previous sections fails to describe the richness of XA spectral features in TMOs denoted as multiplet structure. The multiplet structure is caused by the electron correlations influencing the number of final states. Electron correlations in 3d systems are well described by ligand field multiplet theory, where XA spectra is modelled as combination of atomic correlations and the symmetry imposed by the surrounding ligands.

Atomic effects are included as the Hamiltonian of n electrons in a sub-shell of the free atom:

$$H_{atom} = \sum_{i=1}^{n} (\frac{p_i^2}{2m} - \frac{Ze^2}{r_i}) + \sum_{i=1}^{n} \xi(i) l_i s_i + \sum_{i,j} \frac{e^2}{8\pi\varepsilon_0 r_{ij}} \tag{3.10}$$

where the first term of the hamiltonian is the electron interaction with the nucleous. It gives just the average energy of the transition. The second term is the spin-orbit coupling H_{SO}. The last term is the Coulomb repulsion of the n electrons H_{ee} in the partially filled shell. The sum is not over all electrons in the systems but only those in the partially filled shells.

For a $3d^n$ configuration, the number of microstates is described by their spin moment S, orbital moment L and total angular moment J, combined into the so-called term symbol $^{2S+1}L_J$. One can calculate the matrix elements of the different terms with the electron-electron interaction (H_{ee}) to obtain the relative energies, and the matrix elements are given as:

$$\langle {}^{2S+1}L_J | \frac{e^2}{r_{12}} | {}^{2S+1}L_J \rangle = \sum_k f_k F^k + \sum_k g_k G^k \tag{3.11}$$

where F^k and G^k are the Slater parameters of the Coulomb repulsion and exchange interaction respectively.

The effects caused by the surrounding ligands have to be introduced in TMOs by including crystal field as electrostatic influence of the neighboring atoms on the central TM ion:

$$H_{CF} = -e\phi(\vec{r}) \tag{3.12}$$

Hence, the ligand field accounts for the symmetry of the absorbing atoms given by the surrounding ligands (Fig. 3.5(left)). Furthermore, in TMOs charge transfer effects often

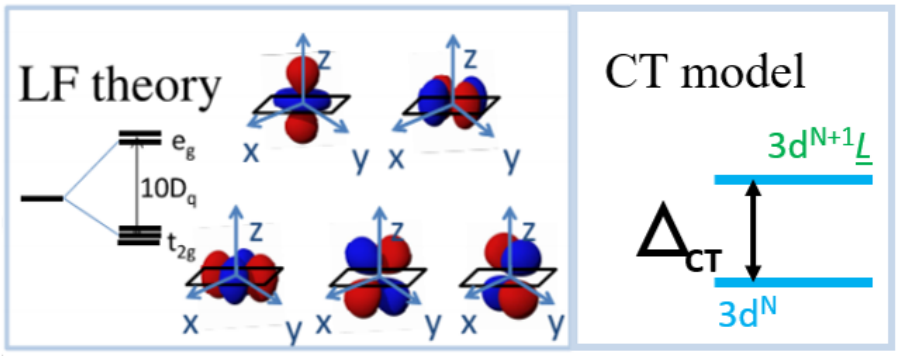

Figure 3.5: Illustration of LF (left) and CT (right) model to describe XA spectra.

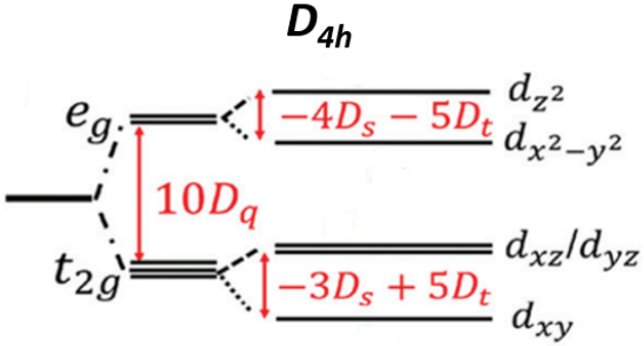

Figure 3.6: Orbital splitting of d level in tetragonal coordination D_{4h}, where energy splitting between $e_g$and t_{2g} is parametrized by 10Dq and further splitting of each level is parametrized by Δ_{eg}=4Ds+5Dt and Δ_{t2g}=3Ds-5Dt.

need to be considered. The charge-transfer (CT) model adds a configuration $3d^{n+1}\underline{L}$ to the $3d^n$ ground state (Fig. 3.5(right)) [64, 65].

To interpret the XLD spectra, simulation of the experimental data were performed using the CTM4XAS software package developed by E. Stavitski and F. de Groot [67]. The CTM4XAS code is based on charge transfer and ligand field effects. For D_{4h} type of symmetry as shown in Fig. 3.6 the following parameters need to be given: Coulomb repulsion energy U_{pd}-U_{dd}, charge transfer energy Δ_{ct}, crystal field splitting 10Dq and splitting between e_g/t_{2g} by changing Ds and Dt [67]. The atomic Slater integrals were reduced by 80% and the atomic spin-orbit coupling were used. In addition, Lorentzian and Gaussian broadening are included. Lorentzian broadening represents the core hole lifetime broadening, which is typically 0.2eV half-width half-maximum for L_3 edge and 0.4eV for L_2. A Gaussian broadening of 0.2 eV due to the experimental resolution was used by default.

In Chapter 5 two basic ligand field multiplet simulations of XLD were used. They represent the single Mn^{3+} e_g electron occupying either the $3d(x^2-y^2)$ orbital (Fig. 3.7(a))

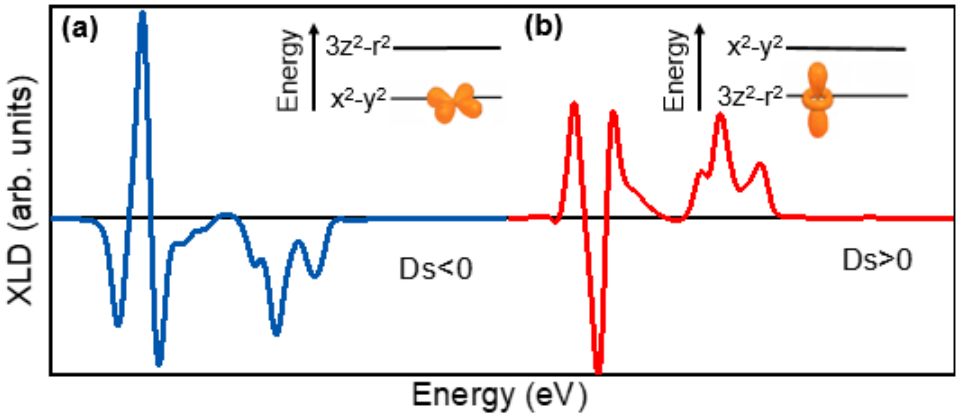

Figure 3.7: Ligand field multiplet simulations of x-ray linear dichroism (XLD) spectra for Mn^{3+}. Parameters are given in Tab. 3.1, where a single e_g electron occupies a) the x^2-y^2 orbital or b) the $3z^2-r^2$ orbital. Figure is taken from [66].

Table 3.1: CTM4XAS parameters used for calculation in Fig. 3.7

e_g occupancy	10Dq	Dt	Ds	Δ	U_{pd}-U_{dd}
x^2-y^2	1.7	-0.01	-0.16	4	2.5
$3z^2-r^2$	1.7	0.01	0.16	4	2.5

or the $3d(3z^2-r^2)$ orbital. These simulations are shown in Fig. 3.7(a,b). The simulations are for Mn^{3+} only since Mn^{4+} does not exhibit linear dichroism. The simulations were done in D_{4h} symmetry with the parameters shown in Tab. 3.1. The $3z^2-r^2(x^2-y^2)$ preferential orbital occupation is induced by positive (negative) sign of Ds and Dt. Δ gives the energy difference between the nominal state d^4 and the charge transfer state $d^5\underline{L}$. The dependence on LSMO thickness in Chapter 5 was obtained by linear combination of the simulations shown in Fig. 3.7, where the sum of scale factors = 1.

3.3 X-Ray Magnetic Circular Dichroism

The magnetic moment of a system comes from the imbalance between spin-up and spin-down states for example in the valence band. This spin polarization can be measured by making XAS spin dependant. This is done by the XMCD technique. We can probe unoccupied states in spin-up and spin-down band by mean of circularly polarized light due to collinearity or non-collinearity (corresponding to two helicities c+ and c- of the x-rays polarization) of transferred angular momentum $\vec{L}_{ph}$ of the incoming x-rays in relation to the sample magnetization $\vec{M}$ (Fig. 3.8):

$$\Delta I_{XMCD} = I^- - I^+ = I^{\vec{L}_{ph}\downarrow\uparrow\vec{M}} - I^{\vec{L}_{ph}\uparrow\uparrow\vec{M}} \tag{3.13}$$

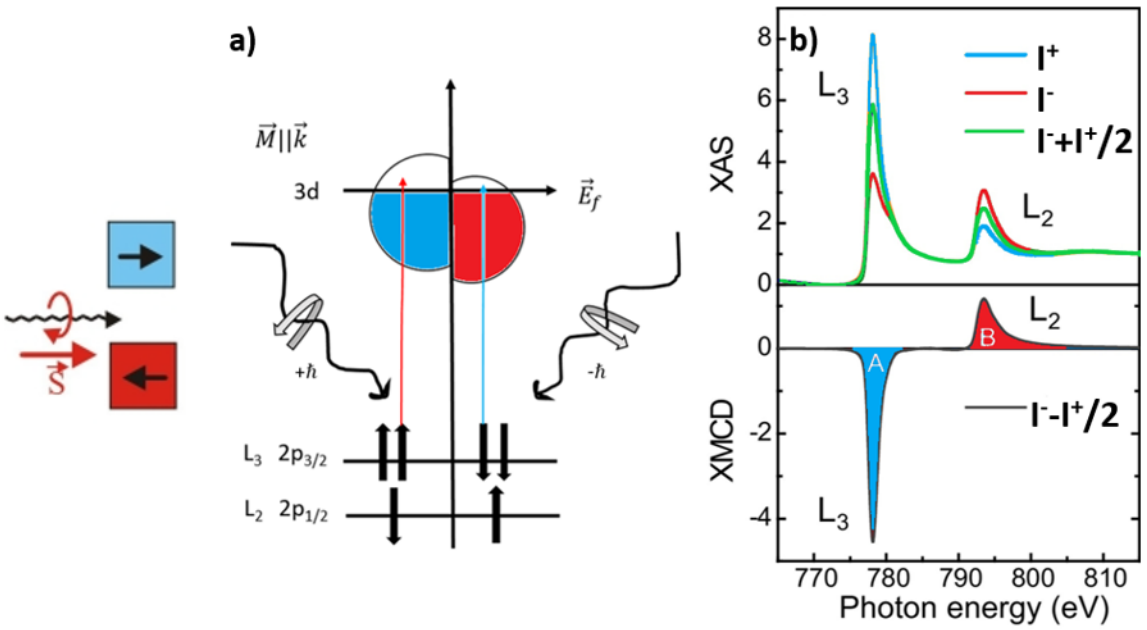

Figure 3.8: Illustration of a) the two-step model of XMCD for a single-electron in the resonant excitation process for a magnetic material. In the first step, a circularly polarized photon with helicity $+\hbar(-\hbar)$ excites a spin polarized electron from the spin–orbit split 2p level. From the $2p_{3/2}$ level (L_3-edge) $+\hbar$ excites 62.5% spin up electrons and $-\hbar$ excites 37.5% spin-up electrons, while the $2p_{1/2}$ level (L_2-edge) yields 25% spin-up and 75% spin-up respectively. In the second step the spin polarized electrons have to find a place in the unoccupied 3d band, resulting in a difference if the 3d electron are spin polarized. b) Two XAS spectra at Co $L_{2,3}$-edge measured with two opposite circular polarization I^+ blue and I^- red and their difference (XMCD), where A is the L_3 intensity and B is the L_2 intensity. Figure is adapted from [68].

from where we see that the I_{XMCD} maximum is achieved when $\vec{L}_{ph}$ is along the magnetization of the sample.

This process can be explained by the so-called two-steps model: as it was mentioned the p states split into two with $j = |l \pm s|$. As a result of opposite spin-orbit coupling spin polarization is reversed for L_3 and L_2 edges. As a first step spin-up (spin-down) states can be excited by utilising c+(c-) polarization. As a second step the d band acts as the spin momentum detector due to unequal population of the spin-up and spin-down states excited from the p levels (Fig. 3.8). The c+(c-) mainly cause the absorption to the states in the minority (majority) band. If no orbital moment is included, the XMCD signal at L_2 and L_3 edges are the same in amplitude, but with different sign as a consequence of opposite spin polarization. However, it is only true, when spin-orbit coupling is zero. Spin-orbit coupling induces imbalance between states with the different m_l affecting intensity

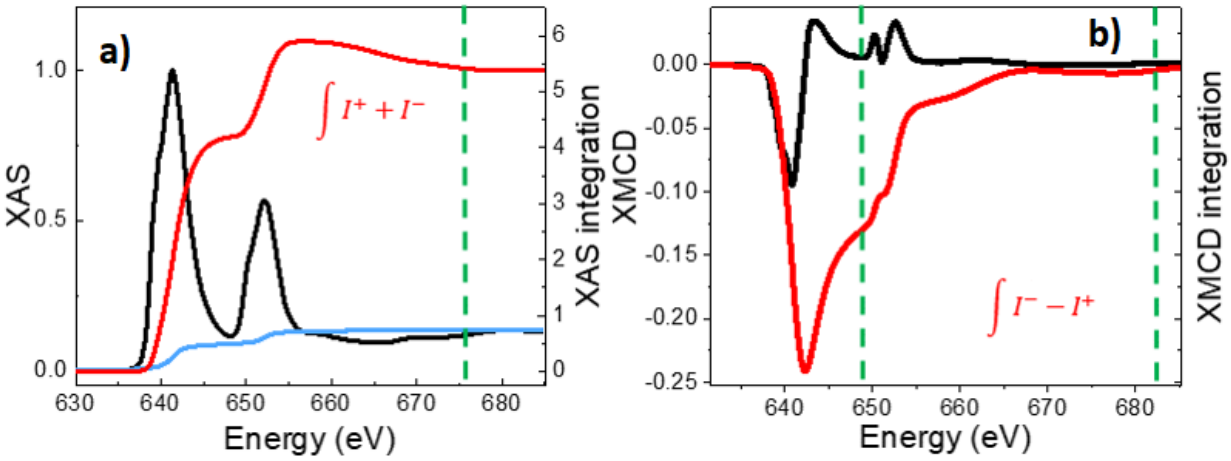

Figure 3.9: Illustration of sum rule analysis at the Mn $L_{2,3}$ edges (a) XA spectra as sum of two polarizations (black) spectra, corresponding step function (blue) and XA integrated intensity after step-function removal (red) (b) XMCD spectrum (black) and corresponding integrated intensity (red). Green dash lines mark positions where the integrals were taken for the calculation of the sum rules.

of L_2 and L_3 XMCD signal. As a consequence m_l and m_s can be quantified separately by applying sum rules, as explained in the following section [11, 69, 70].

3.3.1 Sum rules

As mentioned above the difference between A and B intensities of XMCD spectra comes from the m_l (Fig. 3.8(b)). Hence, simple sum rules can be derived to find exact m_l and m_s contribution as $m_s \propto$A-2B and $m_l \propto$A+B. If normalized, XMCD intensities are linked to size of the magnetic spin and orbital moment per atom as [71, 72, 73]:

$$m_l = -\frac{4\int_{L_3+L_2}(I^+ - I^-)\mathrm{d}\omega}{3\int_{L_3+L_2}(I^+ + I^-)\mathrm{d}\omega}(10 - n_{3d}) \tag{3.14}$$

$$m_s = -\frac{6\int_{L_3}(I^+ - I^-)\mathrm{d}\omega - 4\int_{L_3+L_2}(I^+ - I^-)\mathrm{d}\omega}{\int_{L_3+L_2}(I^+ + I^-)\mathrm{d}\omega}(10 - n_{3d})(1 + \frac{7\langle T_z\rangle}{2\langle S_z\rangle})^{-1} \tag{3.15}$$

where $10 - n_{3d}$ is number of holes at the probed element, $\langle T_z\rangle$ is the expectation value of the intra-atomic magnetic dipole operator term and $\langle S_z\rangle$ is the spin moment. The latter provides a measure of the anisotropy of the field of the spins, when the atomic cloud is distorted by crystal field effects or spin-orbit interaction. In our case Mn and Ni have negligible $\langle T_z\rangle$ in the orthorhombic environment and thus $\frac{7\langle T_z\rangle}{2\langle S_z\rangle}$ [74].

Spin sum rules requires that L_2 and L_3 edges are very well separated being pure $p_{1/2}$ and $p_{3/2}$. However, often L_2 and L_3 are mixed requiring a correction factor. The higher

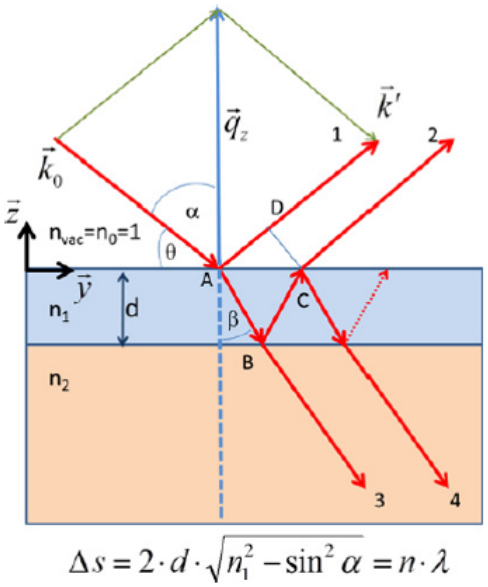

Figure 3.10: Geometry of refraction and reflection taking place at the surface of a thin film, where k_0 is the incident wavefront, k' is the reflected wavefront, Q_z is the momentum transfer in the z-direction, θ is the angle which the ray makes with the film surface, α is the angle of incidence (angle between the incident ray and the normal) and β is the angle of refraction (angle between the refracted ray and the normal). Figure is taken from [76].

the atomic number of the 3d element, the larger the 2p spin-orbit coupling and therefore the L_3 and L_2 separation. Therefore, Ni has both edges well resolved, while for the Mn 1.5 correction factor is needed [75].

Eq. (3.14) and (3.15) denominator require the resonant part of the XA spectrum, therefore a baseline needs to be removed from the XA spectrum (blue line in Fig. 3.9(left)). The baseline was subtracted from the $L_{2,3}$ XA spectra (Fig. 3.9(blue)) as a step function that represents 2/3 (1/3) of the complete edge jump due to the degeneracy of these states.

3.4 Resonant Reflectivity

The description in this chapter follows [76].

Three events can occur when the light interact with the surface of the thin film with index of refraction n_1: refraction, reflection and absorption of the light. As presented in Fig. 3.10 at the interface air-film incident beam is partially reflected by the film conserving the angle θ with the film surface and partially refracted at the depth d and at the angle β of refraction with the film normal. The refracted beam is, in turn, again partially reflected and partially refracted at the interface with index of refraction n_2 (Fig. 3.10). Reflected beams from different interfaces will interfere constructively or destructively

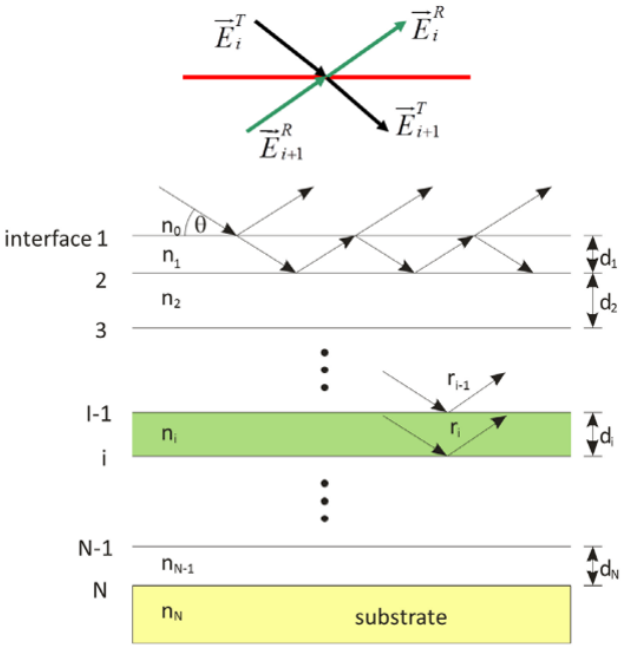

Figure 3.11: Reflection and refraction at multiple interfaces scheme. Figure is taken from [76].

forming a pattern with oscillating intensity as a function of incidence angle known as Kiessig fringes. This fringe pattern contains information on thickness, density profile and roughness of each individual layer.

The refraction is governed by Snell's law:

$$n_1 sin\alpha = n_2 sin\beta \tag{3.16}$$

According to the Bragg's law the phase difference for constructive interference is:

$$2dsin\theta = n\lambda \tag{3.17}$$

where the momentum transfer in z-direction can be calculated as:

$$q_z = \frac{4\pi sin\theta}{\lambda} \tag{3.18}$$

Fresnel equation expressing intensities of reflected r and transmitted t light with two polarization π perpendicular and parallel σ to the sample surface were derived [77, 78]:

$$t_\sigma = \frac{E_t}{E_i} = \frac{2n_1 cos\alpha}{n_1 cos\alpha + n_2 cos\beta}, r_\sigma = \frac{E_r}{E_i} = \frac{2n_1 cos\alpha - n_2 cos\beta}{n_1 cos\alpha + n_2 cos\beta} \tag{3.19}$$

$$t_\pi = \frac{E_t}{E_i} = \frac{2n_1 cos\alpha}{n_2 cos\alpha + n_1 cos\beta}, r_\pi = \frac{E_r}{E_i} = \frac{2n_1 cos\beta - n_2 cos\alpha}{n_2 cos\alpha + n_1 cos\beta} \tag{3.20}$$

where E_r, E_i and E_t are reflected, incident and transmitted components of the electric field. α and β angles are shown in Fig. 3.10. As it can be seen, the reflection intensity is higher the larger the contrast between the different refractive index is and that reflectivity decreases rapidly with increasing incident angle. The reflection intensity is also connected with the polarization of the incident photon beam.

However, in the Eq. (3.19) and (3.20) multiple reflections from the different interfaces in the heterostructure are not considered. It is taken into account by the Parrat model, where the Fresnel equations are solved at every interface (Fig. 3.11) [79]:

$$E_i^R e^{ik_i z} = rE_i^T e^{ik_i z} + (1-r)E_{i+1}^R e^{ik_{i+1} z} \tag{3.21}$$

$$E_{i+1}^T e^{-ik_{i+1} z} = -rE_i^T e^{ik_{i+1} z} + (1+r)E_{i+1}^R e^{-ik_i z} \tag{3.22}$$

This model calculates amplitude of the reflected E_i^R/E_{i+1}^R and transmitted E_i^T/E_{i+1}^T waves for i/i+1 layers with wave vector k at the depth z_i with amplitude ratio R_i:

$$R_i = \frac{r_i + R_{i+1} e^{2ik_{i+1} d_{i+1}}}{1 + r_i R_{i+1} e^{2ik_{i+1} d_{i+1}}} \tag{3.23}$$

where r is the reflectivity of one light beam, R is the total electric field ratio in a layer $R_i = E_i^R/E_i^T$, k_i is the normal wave vector component in layer i and d_i is the thickness of layer i.

The total reflectivity is then given by:

$$\frac{I_R}{I_0} = |R_0|^2 \tag{3.24}$$

Roughness of the interface in the multilayer system is another important factor influencing the intensity of the total reflection. A change of reflected intensity due to a rough interface can be described as an exponential decay of the Frensel coefficients: The total reflectivity is then given by:

$$r_{i,i+1}^{rough} = r_{i,i+1} e^{-k_{z,i} k_{z,i+1} \sigma^2} \tag{3.25}$$

where σ is the roughness factor.

Initially the Paratt formalism was developed only for linearly polarized light. To apply this scheme to the circularly polarized light the polarization vectors have to be converted as:

$$\vec{e}_- = \frac{1}{\sqrt{2}}(\vec{e}_\sigma + i\vec{e}_\pi), \vec{e}_+ = \frac{1}{\sqrt{2}}(\vec{e}_\sigma - i\vec{e}_\pi), \tag{3.26}$$

for circular left and right respectively.

RXRR combines normal reflectivity with x-ray absorption spectroscopy that is explained in previous section. In this work, energy of the x-rays is tuned to match $L_{2,3}$-edges

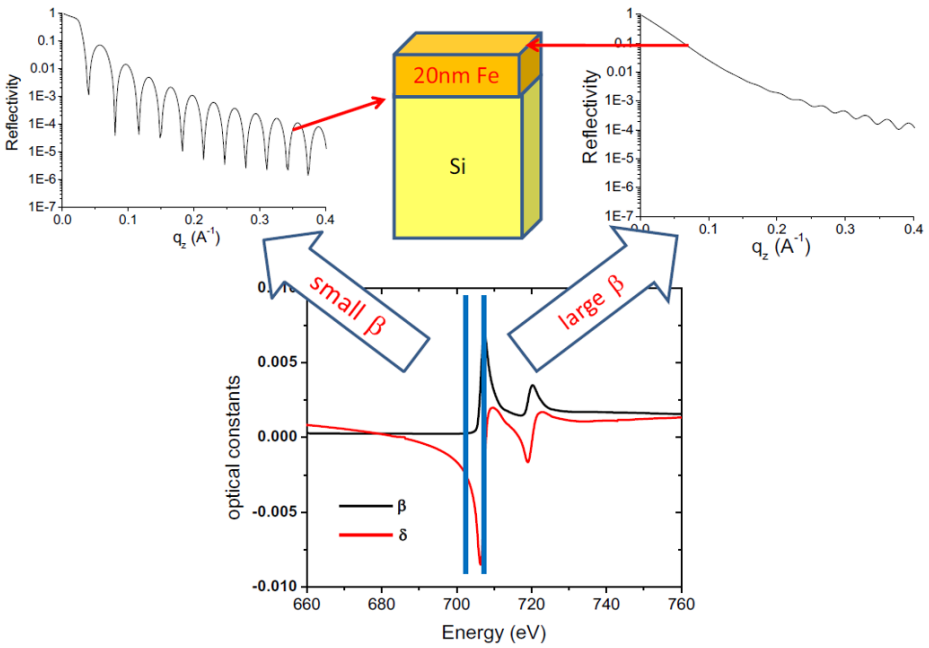

Figure 3.12: Influence on scattering intensity of β and σ values is illustrated at Fe edge from Fe film on silicon. Figure is taken from [76].

resulting in an enhancement of scattering process due to resonance. From the index of refraction n:

$$n = 1 - \delta + i\beta \tag{3.27}$$

this enhancement can be clearly seen from Fig. 3.12. In Eq. (3.27) the real part δ is associated with refraction, while imaginary part β is associated with absorption.

In analogy with XMCD technique, resonant scattering can also give magnetic contrast in so-called X-Ray Magnetic Reflectivity (XRMR). The total resonant scattering intensity is proportional to the square of atomic scattering factor $I \propto |\sum_j f_j e^{i\vec{Q}\vec{r_j}}|^2$. Then the scattering form factor on the basis of the two polarization vectors $\vec{e}_f$ and $\vec{e}_i$ is [80]:

$$f = (\vec{e}_f^{\,*} \times \vec{e}_i)[f_0 + f'(E) + if''(E)] + i(\vec{e}_f^{\,*} \times \vec{e}_i)\vec{b}[m'(E) + im''(E)] \tag{3.28}$$

that describes several types of scattering. f_0 is related to Thomson scattering, while factors f" and f' are associated with the anomalous scattering. Anomalous scattering consists of two processes explained in Section 3.1: the excitation of the bound states to unbound continuum states (background step-like structure) and dipole selected excitation of the core electrons to an unoccupied state (absorption edge). These scattering factors are isotropic and do not alter the polarization of the scattered beam. The anisotropic factors m' and m'' govern the magnetic scattering. The vector defines the direction of

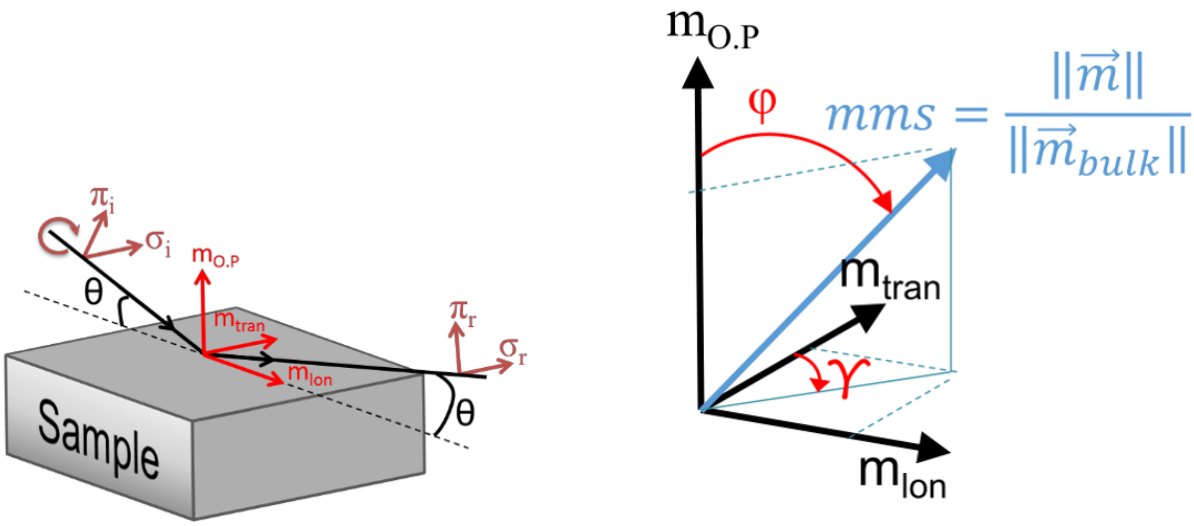

Figure 3.13: Illustration of the magnetic transverse (m_{tran}), longitudinal (m_{lon}) and polar ($m_{o.p}$) components relative to the scattering geometry. Figure is taken from [82].

the magnetic moment and can be expressed in spherical coordinates as:

$$\vec{b} = \begin{pmatrix} sin\varphi sin\gamma \\ sin\varphi cos\gamma \\ cos\varphi \end{pmatrix} \tag{3.29}$$

where φ and γ angles are illustrated in Fig. 3.13(right).

f'' and m'' correspond to the XA and XMCD and can be obtained experimentally. After scaling XA spectrum to the tabulated value from the Chantler table [81], the Kramers-Kronig relation can be applied to derive the dispersive part f' [11]:

$$f'(w) = \frac{2}{\pi} \int_0^\infty \frac{w' f''(w')}{w^2 - w'^2} dw' \tag{3.30}$$

The same procedure can be applied to the magnetic term treating XA spectra for each polarization separately. XMCD spectra corresponds to m'' and the difference between Kramers-Kronig transforms f' of two different polarizations corresponds to m'.

Angstrom-resolved magnetic profile can be estimated from the angular dependency of the asymmetry calculated as:

$$R = \frac{I^- - I^+}{I^- + I^+} \tag{3.31}$$

where I^- and I^+ are the intensity of reflected circularly polarized light.

3.4.1 RXRR simulation

In this work RXRR and RXMR quantitative analysis is performed employing DYNA software in Matlab environment. DYNA combines fitting of layers model and a matrix

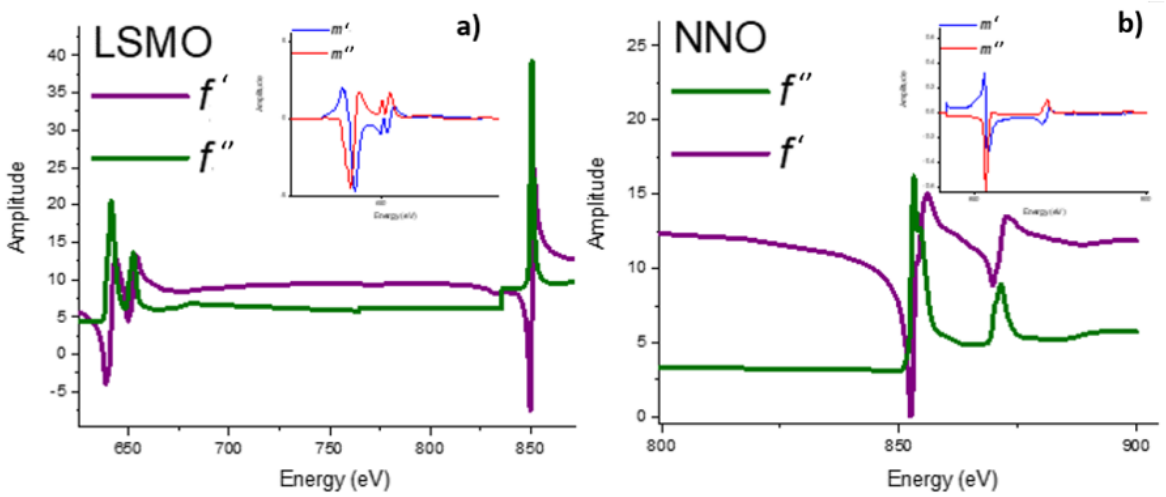

Figure 3.14: Examples of charge and magnetic terms of optical constant calculated for a) LSMO33 and b) NNO.

formalism developed by M. Elzo *et al.* [83] that is able to reproduce non-resonant and resonant curve with and without magnetic contribution.

Various experimental parameters affect the simulated curve as well as purely structural parameters for reflectivity such as density, roughness and thickness. The structural parameters are obtained from the out-of-resonance measurement or from on-resonance measurements above the magnetic ordering temperature. Additionally, the parameters related to the magnetic moment are: mms, φ and γ values. mms value is defined as a relation between magnetic moment of fitted layer divided by magnetic moment per atom extracted from magnetic scattering constant m'' mms=$||\vec{m}||/||\vec{m}_{bulk}||$. φ is an angle between sample normal and magnetic moment, wheras γ is an angle between projection of the magnetic moment and scattering plane as shown in Fig. 3.13. Therefore three possible magnetic configurations are enabled: transverse (m_{tran}, it exists mostly for linear polarization), longitudinal (m_{lon}) and polar ($m_{o.p}$) [82]. Qualitatively, oscillations at low angles in R appear in presence of the longitudinal component of the magnetic moment, while at high angles it is an indication of polar magnetic contribution.

In order to fit reflectivity data the DYNA software requires to load information on the optical constants: $f', f", m', m"$, explained in the previous section. Fig. 3.14 shows the results for our data. However, in our case we encountered certain difficulties due to the XA baseline. XA baseline imperfection brings a large error. In our case this was especially difficult because the insulating NNO gives a large non-linear slope for the spectra measured in TEY mode.

Moreover, the XA at Ni edge from NNO/LSMO heterostructure suffers from large contribution of La M_4. For a correct analysis the La contribution has to be removed from

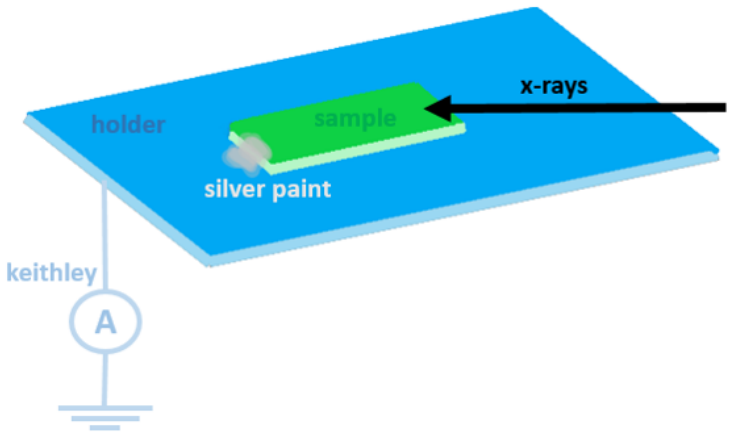

Figure 3.15: Schematic experimental setup of TEY mode measurements.

the measured Ni data and added to the Mn data, since it belongs to the LSMO layer and not to the NNO layer. La M_4 peak was fitted by linear combination of Lorentzian and Gaussian functions and then subtracted from NNO. Furthermore, Mn XAS from LSMO and La peak from fitting were scaled using non-resonant data from the Chantler table for the single atom [81] and added to each other corresponding to the nominal LSMO composition. Ni XAS from NNO was scaled following the same procedure. Finally, the Kramers-Kronig transformation was performed for each compound: LSMO and NNO. The substrate contribution (NGO) was considered as negligible since only non-resonant part was taken into account. XMCD measured in 6.5T at 10K was analyzed to get the magnetic part (Fig. 3.14(inset)).

Fitting of the reflectivity data was performed in collaboration with Dr. Jean-Marc Tonnerre from Institut Néel, who gave me the training and assisted during the process.

3.5 Instrumentation

3.5.1 Soft x-ray absorption detection modes

Different detecting techniques are available for recording XA spectra. The most direct way of measuring absorption is measuring the intensity of the x-ray beam before and after the transmission through a thin film. However, for the soft x-rays the penetration length of the photons is very short (up to 100 nm) limiting the use of transmission detection. Therefore indirect yielding techniques such as Total Electron Yield (TEY) [84] and Total Fluorescence Yield (TFY) [85] are used.

In TEY, secondary electrons are detected providing the surface sensitiveness due to the short electron mean free path in solids. The depth-resolved XAS TEY signal for i-th

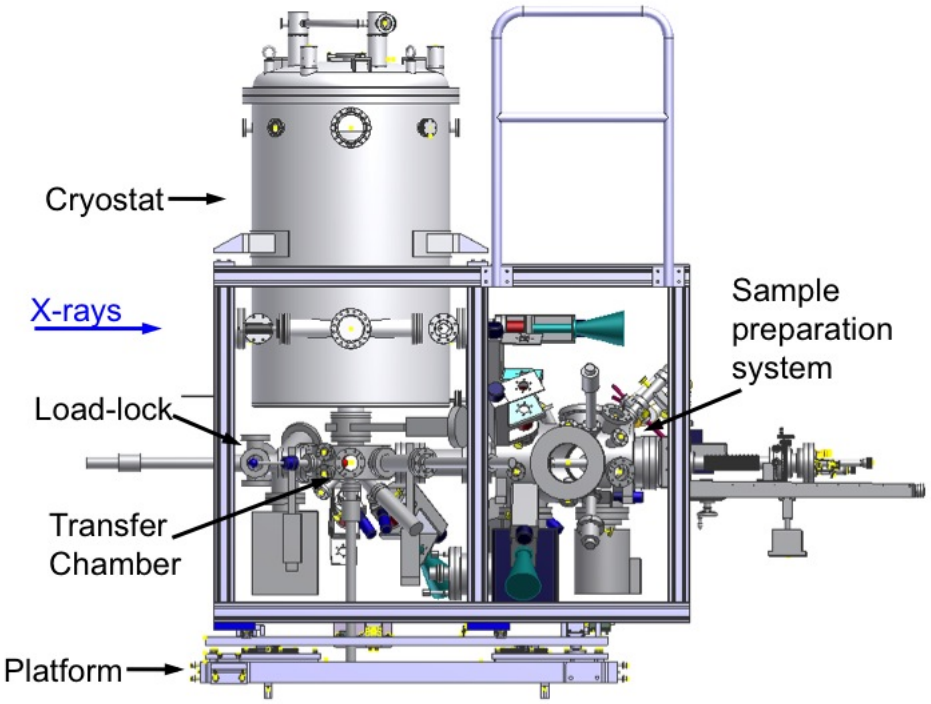

Figure 3.16: Side view drawing of the end-station showing the sample preparation system, load-lock, transfer chamber and the main cryostat where the measurements are performed. Figure is taken from [89].

layer I_i to the normalized XAS spectrum can be expressed as:

$$I_i = \frac{\sum_{i=1}^{n} exp[-t_i/\lambda]}{exp[-t/\delta]} \tag{3.32}$$

where δ is attenuation length (probing depth), t is total thickness of the sample and t_i is thickness of i-th layer [86, 87]. For the TEY it is required that the surface of the sample is conducting. At X-Treme beamline TEY is measured using drain current, while the sample is mounted on electrically conducting holder. Electrical contact is created by applying conductive silver paint from the holder to the sample surface (Fig. 3.15).

In TFY photons emitted from the sample are recorded as a function of photon energy. It is not required for the sample to be conducting. Due to penetration depth of photons TFY probing depth runs up to 100nm providing bulk sensitivity unlike TEY. However, this technique suffers from self-absorption and does not allow use of sum rules [88].

3.5.2 X-Treme end-station

Most of the measurements were performed at the X-Treme beamline at Swiss Light Source [89]. This beamline is specialized in absorption spectroscopy measurements at high magnetic field and at low temperature. The end-station shown in Fig. 3.16 operates in ultra

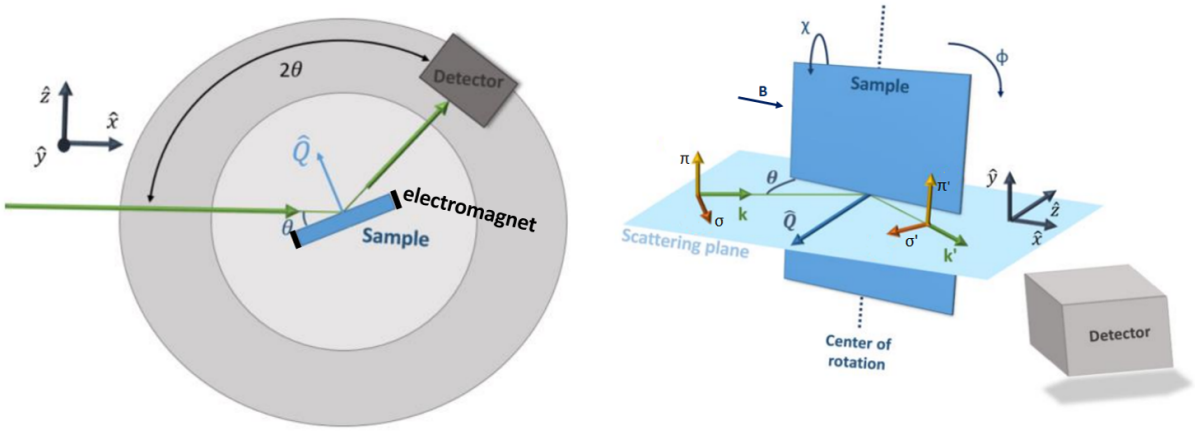

Figure 3.17: (left) Top view of RESOXS of the inside part and (right) sketch of RESOXS chamber geometry and rotation movements. Figure is adapted from [90].

high vacuum, in soft x-ray range from 400 to 1800 eV and in temperature range between 2K and 360K. Fully polarized x-rays are produced by an elliptical undulator that enables change of polarization between circular right/left and linear 0/90. The end-station is equipped with a superconducting vector magnet producing fields up to 7T along the beam and up to 2T perpendicular to the beam. The sample has an electrical contact connected to a feedthrough allowing X-ray absorption detection through the TEY current measured between sample and ground. Additionally, TFY mode is measured by a photodiode perpedicular to the x-ray beam.

3.5.3 RESOXS end-station

Resonant scattering measurements were obtained at RESOXS end-station of the SIM beamline at the Swiss Light Source [91]. The SIM beamline has two elliptical undulators as source. The x-ray energy can be varied in 90-2100eV range and polarization can be changed between circular right/left and linear 0/90. RESOXS chamber is equipped with 4-circle diffractometer, which operates under high vacuum conditions. Sample is placed in He flow cryostat that enables achieving temperature down to 5K. Measurements are taken using photodiode detector (Fig. 3.17). The chamber has three motorized translations (x, y and z) and three rotational axes (θ, χ and φ), as shown in Fig. 3.17. Magnetic field is applied along x using an electromagnet with a field up to 0.2T.

Resonant scattering experiments were supported by staff of SIM beamline: Dr. Urs Staub, Dr. Nazaret Ortiz Hernández and Dr. Elizabeth Skoropata.

Chapter 4

Sample fabrication and characterization

Performing high quality growth of ultra-thin layers in heterostructure is a challenging task. Thickness of each layer needs to be controlled with unit-cell resolution, crystallinity needs to be maintained and abrupt interfaces achieved. Additionally, ultra-thin heterostructures require after-growth detailed characterization of their properties to examine strain state, unit cell parameters and magnetic properties. In this chapter growth and characterization methods are presented.

4.1 Pulsed Laser Deposition

The Pulsed Laser Deposition (PLD) technique is one of the best techniques for growth of high-quality oxides thin films, their multilayers and heterostructures. During the growth process a stochiometric target is ablated by a short laser pulse in high vacuum and in oxygen ambiance. Each laser pulse transfers a small quantity of target material to the heated substrate that is mounted at a certain distance and angle from the target (Fig. 4.1). Growing layer mimics crystal structure of the target [92]. The laser plum and therefore the growth can be optimized by laser fluence (defined as the ratio between the laser energy and the area of the laser pulse), oxygen pressure (that is required for oxides growth), temperature of the substrate, pulse repetition rate etc.

Different growth mode can be realized depending on the free energy of the film surface, substrate surface and the interface between them. Strong adhesion between film and substrate induces layer-by-layer growth mode featured by completion of each layer before growth of the next one. In case of the weak bonding between substrate and film three dimensional structure is formed in so-called island growth mode. This mode results in higher probability of structural disorders and defects. A combination of both modes can

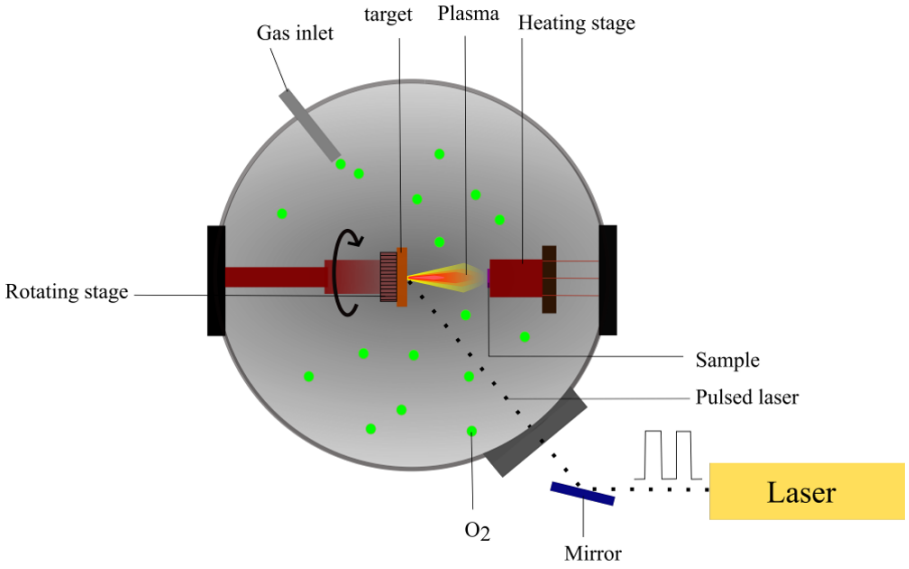

Figure 4.1: Schematic PLD setup view. Figure is adapted from [93].

occur in thin film growth. The growth mode is controlled by the elastic energy i.e. the lattice mismatch between substrate and the growing film: first, growth occurs in layer-by-layer mode (strained film) until it starts to relax minimizing then elastic energy by forming islands [92].

Reflection high-energy electron diffraction (RHEED) is a surface-sensitive grazing angle technique and was used to monitor the thin film growth *in-situ*. The electron diffraction pattern is generated by the high energy electron beam ($\approx 30KeV$) at the surface of the sample. According to the Laue diffraction equation spots occur when the incident and diffracted wave vectors differs by a reciprocal lattice vector. All possible diffraction points are given by the Ewald sphere. The atomically flat surface of a crystal is a two-dimensional lattice. Thus, the reciprocal lattice consists of rods extending out of the 2D plane of the crystal surface infinitely in the out-of-plane direction. The diffraction pattern is made visible on a phosphor screen (Fig.4.2(left)). For a non-flat surface, the loss in crystallinity or island growth mode will cause these rods to be broadened or shifted. The intensity of a single rod is monitored as a function of time. When one full layer is completed the intensity shows a maximum, while during the growth the intensity is lower. These are the so called RHEED oscillations (Fig. 4.2(right)). Therefore, thickness, growth rate and crystallinity control of the film can be performed *in-situ* owing to RHEED [92].

For the films grown in this thesis, the fourth harmonic of a Nd:YAG laser at a repetition rate of 2 Hz was used to ablate the target and proceed with the growth of heterostructures. All samples were prepared by PLD using stoichiometric targets of LSMO33, LSMO12, SRO and NNO. An oxygen pressure of 10^{-1} mBar and substrate temperature of 720C°

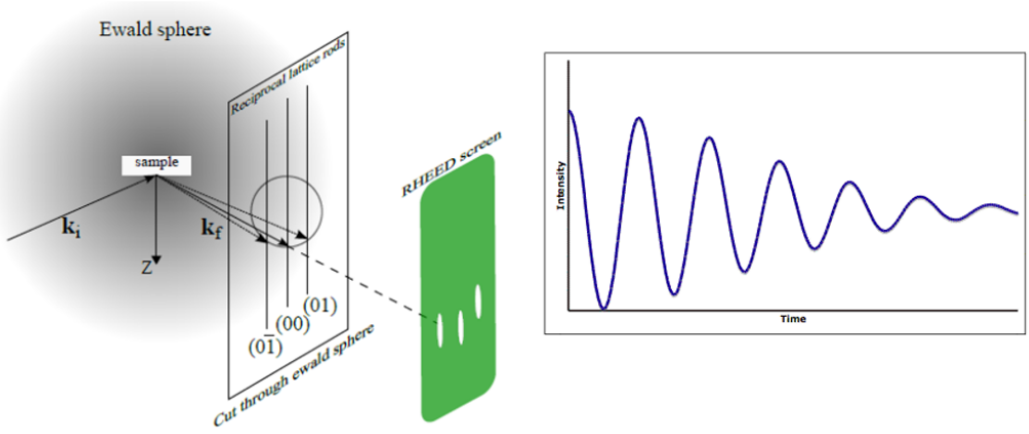

Figure 4.2: (left) An Ewald sphere and a set of RHEED diffraction maxima for a two dimensional lattice (figure is taken from [94]) (right) RHEED oscillations intensity over the time.

were used during deposition. Sample growth was performed at PSI by me in collaboration with Dr. Milan Radovic, Dr. Marco Caputo, Dr. Teguh C. Asmara and Dr. Eduardo Guedes from the Spectroscopy of Novel Materials Group, PSI.

4.2 X-Ray Diffraction (XRD) and Reflectivity (XRR)

X-Ray Diffraction (XRD) is a fundamental technique for crystalline material characterization. For a detailed review see for example [95, 96]. Information on lattice parameters, surface and epitaxy can be obtained from the diffraction pattern from x-ray scattering by thin film lattice. Lattice planes are separated by interatomic distance d_{hkl} determined by:

$$n\lambda = 2d_{hkl}sin\theta \tag{4.1}$$

here d is the spacing between diffracting planes, θ is the incident angle, n is any integer, and λ is the wavelength of the beam. XRD experiment requires cathode tube, monochromator with various slits and filters to shape the beam and vary its intensity and minimize undesired effects, sample stage and detector. During the XRD experiment λ is known and in a table top source typically corresponds to Cu K_α with λ=1.5418Å.

In θ-2θ scanning mode the position of the x-ray tube is fixed, while the intensity of the diffracted beam is obtained by moving the sample and detector maintaining θ and 2θ ratio for sample and detector, respectively. XRD is the most straightforward technique to examine atomic parameters of the film and growth mode. Samples grown on crystalline substrates are expected to be crystalline that is supposed to give a sharp diffraction peak

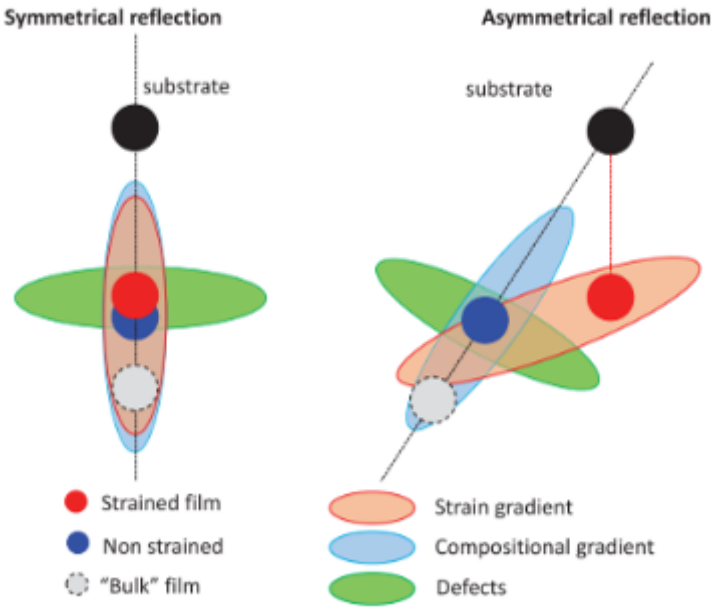

Figure 4.3: Possible RSM configurations. Figure is taken from [97].

and symmetric fringes. Epitaxy between the film and the substrate can be evaluated based on extracted lattice parameters using Bragg's law.

Reciprocal Space Mapping (RSM) is an alternative scanning mode, when scans are collected while varying ω angle between x-ray source and the sample surface around one Bragg reflection in so-called coupled (i.e. the scattered q-vector fixed) ω-2θ scan. RSM gives most detailed information on the in-plane and out-of-plane lattice parameters of the sample, film relaxation, defects etc. It can be seen as intensity gradient, composition gradient or asymmetry of the intensity maxima (Fig. 4.3).

Main principles of X-Ray Reflectivity (XRR) were already given in Chapter 3. In this case pre-characterization was conducted by non-resonant XRR using lab-source of x-rays. Despite lower resolution and intensity comparing to synchrotron reflectivity, laboratory XRR is a powerful tool to quickly examine thickness and roughness of the heterostructure with enough accuracy. Here, the grazing incident angle θ is changed between 0.5°-5°, while reflected beam is detected in specular direction obtaining Kiessig fringes.

In this thesis XRD and XRR experiments were performed at BRUKER D8 Discover diffractometer of the Mesoscopic Systems Group, PSI. XRR reflectivity curves were then further analyzed using LEPROS and EVA software packages to extract structural parameters. Most of the measurements were done by me after initial training on how to operate XRD and XRR setup from Dr. Laura Maurel, PSI, otherwise data was obtained by Dr. Maurel directly.

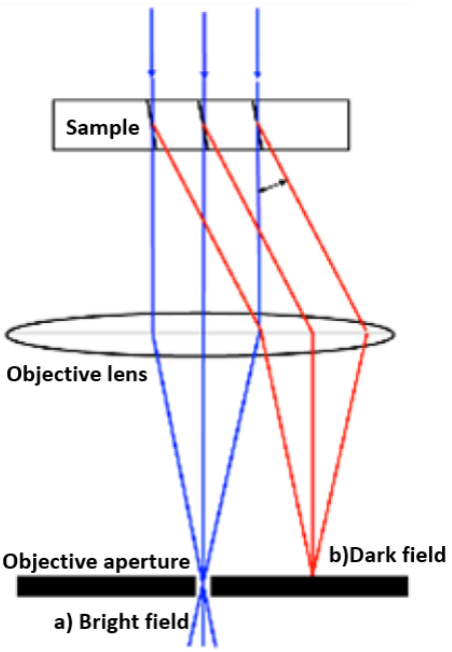

Figure 4.4: Schematic TEM configuration with two aperture positions for imaging in a) bright field and b) dark field modes. Figure is adapted from [98].

4.3 Transmission Electron Microscopy (TEM)

Transmission Electron Microscopy (TEM) can be used to learn about material structure at the atomic level. For a detailed review see for example [99]. Conventional setup includes electron source, anode and magnetic lenses (to shape the electron beam and minimize unnecessary aberrations), sample holder, fluorescence screen and a detector. In TEM an image is formed by transmitting electrons through the sample atomic position, level of crystallinity and interface quality of the multilayer structures. Two detection options are possible: Dark Field (DF) and Bright Field (BF) imaging. Those two modes of TEM differ by the objective aperture position. In the BF imaging aperture is placed in a back focal plane such that only direct beam is involved in the image formation, whereas the DF includes only scattered electrons (Fig. 4.4). For BF imaging mode an area detector is used, while it is a ring detector for the DF image. DF image, therefore, appears as a very dark image due to big contribution of undiffracted beam blocked by the aperture.

TEM imaging can be complemented by element specific probe of the sample to better understand chemical composition of each layer. Elements are mapped by energy dispersive x-rays (EDX) spectroscopy.

In this thesis TEM and EDX experiments were performed at JEM 2200FS microscope of Electron Microscopy facility, PSI. Measurements were done by Dr. Elisabeth Muller, PSI.

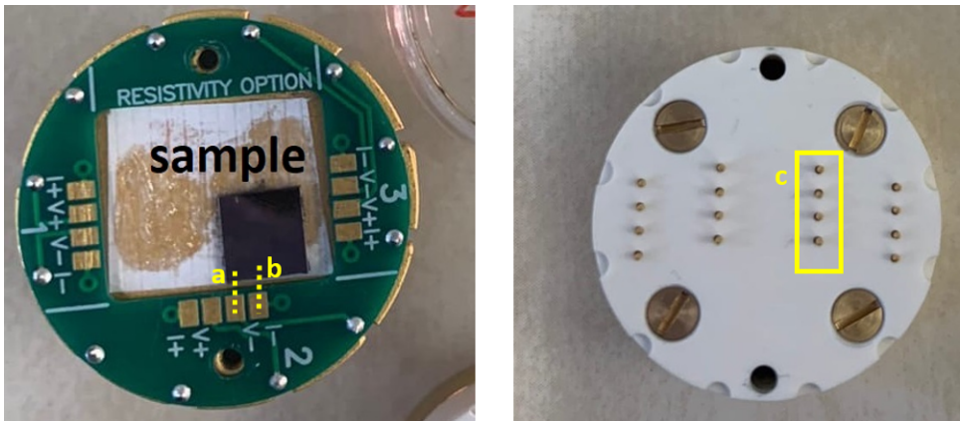

Figure 4.5: (left) A four-point sample puck (right) Copper pins mask. As a, b and c contacts to the puck and to the sample surface are labelled respectively.

4.4 Electrical transport

Electrical transport measurement provides information on carrier densities, mobility, resistivity (resistance) and conductance(conductivity) as a function of temperature. Our aim was to characterize the MIT evolution in our films. For this experiment a resistivity sample puck was used which is shown in Fig. 4.4(left). It has a four-point contacts enabling measurements of both current and voltage (one positive and one negative contact) drop across the sample with a high accuracy for each user bridge board channel. Each channel is connected to the sample surface with the copper pins at the mask (Fig. 4.4(right)). Resistance then is defined by the Ohm's law as DC voltage divided by current.

In this thesis a PPMS 9T from Quantum design of the Physical Properties of Materials Group, PSI was used to perform resistance measurements by Dr. Maria Luisa Medarde from PSI.

4.5 DC magnetometry

Superconducting Quantum Interference Device (SQUID) measures DC magnetization curve using a superconducting magnet, pickup coil and magnetic shield. For a detailed review see [100, 101]. Pickup detection coil is made from superconducting wire that forms second-derivative gradiometer (four coils are wound: two outer are counter-clockwise, two inner coils are clockwise Fig.4.6(left)) to cancel magnetic field fluctuation coming from the superconducting magnet. While moving the sample relatively to the pickup coil, it generates oscillating voltage that is proportional to the change in magnetic flux (Fig. 4.6(right)) [100, 101].

SQUID is normally included in Magnetic Properties Measurements system (MPMS)

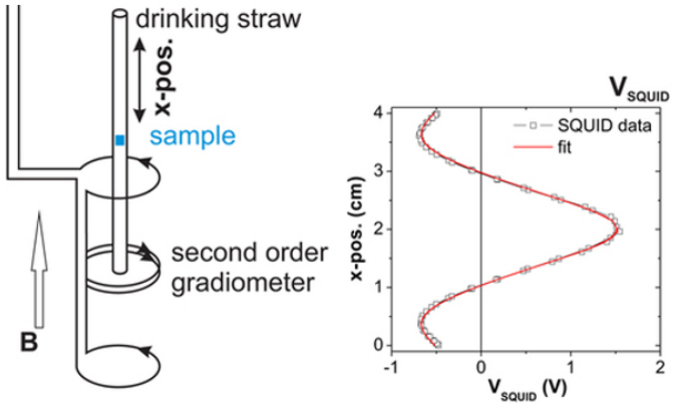

Figure 4.6: (left) SQUID sketch that illustrates detection coil in applied magnetic field and sample position (right) corresponding SQUID voltage response V versus sample position x. Figure is adapted from [100].

XL 7T. In this work magnetization measurements were done by me at Mesoscopic Systems Group, PSI after training by Dr. Maurel from PSI.

4.6 AC susceptibility

AC susceptibility measurement is another option that can be realized on MPMS. Unlike DC magnetization, where magnetic moment is time independent, AC mode is able to capture a change in magnetization dynamics. The field of the time-dependent moment induces a current in the pickup coils, allowing measurement without sample motion. AC susceptibility χ simply is a slope of M(H) curve $\chi = dM/dH$. In a small AC applied field given by h_{ac}, the time-dependent change in magnetic moment M can be expressed as:

$$M_{ac} = \chi h_{ac} sin(\omega t) \tag{4.2}$$

where ω is the driving frequency.

While at low frequencies it follows DC M(H) behaviour, at the high frequencies dynamic effects contribute. χ has a complex behaviour:

$$\chi = \chi' + i\chi'', \tag{4.3}$$

where real component χ' is related to the reversible magnetization process and imaginary χ'' is related to the irreversible magnetization process and energy absorbed from the field.

In this work AC susceptibility was used to access irreversible spin dynamics or spin-glass state by measuring χ' and χ'' as a function of temperature for different driving frequencies. AC susceptibility measurements were done by Dr. Maria Luisa Medarde, PSI at the PPMS 9T of the Physical Properties of Materials Group, PSI.

Chapter 5

Interplay between magnetism and interface-induced effects in ruthenate-manganite heterostructure

In this chapter, we investigate the origin of magnetism stabilization in LSMO33/SRO bilayers. A thorough investigation of bilayers properties combines magnetism study by XMCD as well as electronic and orbital occupation study by XAS and XLD. The text, figures and results described in this chapter are adapted from [66] [1].

5.1 Introduction

In the ultrathin films of LSMO33, it was reported that the magnetic and electronic properties are dramatically affected [102, 103, 104, 105]. This effect in LSMO33 film is attributed to a so-called magnetic dead layer with critical thickness of 5–7uc on STO [106, 107, 108]. Different possible explanations for the absence of magnetism have been reported as orbital modification at the interface and surface [109, 110, 111, 112, 113], octahedral rotation [114, 115], and charge redistribution [116]. XLD has been widely used to identify the impact of orbital occupation and orbital modification on magnetism in ultrathin LSMO33 films [112, 113, 114, 115, 116, 117].

[1] For this project, LSMO33/SRO and LSMO//STO samples were grown by me in collaboration with Dr. Milan Radovic, Dr. Marco Capuro and Dr. Eduardo Guedes from the Spectroscopy of Novel Materials Group at PSI. The XRD and XRR experiments were performed by me and Dr. Laura Maurel from the Mesoscopic Systems Group at PSI. XA, XMCD and XLD data were obtained at the X-treme beamline by Dr. Cinthia Piamonteze, Dr. Marco Caputo, Dr. Eduardo Guedes and me. CTM4XAS simulations were performed by me. I contributed to the paper published based on this project as the main author.

Nonetheless, it has been found experimentally that the magnetic dead layer thickness in LSMO33 thin films interfaced with SRO is reduced [118, 119, 120, 121]. In LSMO33/SRO heterostructures, Ru 4d couples with Mn 3d via interfacial oxygen atoms, resulting in AF coupling between two ferromagnets [122]. The overlap between transition metal d and O 2p orbitals directly influences the strength and sign of the indirect magnetic exchange interaction; therefore, parameters such as orbital occupancy play a key role. Lv *et al.* [123] have performed density functional theory (DFT) calculations showing that LSMO33 in contact with SRO undergoes an orbital restructuring which, in conjunction with charge transfer, stabilizes a robust ferromagnetismat LSMO33 below its critical thickness. However, currently, no experimental evidence for such orbital reconstruction is presented.

To understand the influence of SRO on the orbital reconstruction and charge transfer and linking it to the LSMO33 magnetic properties, we investigate here LSMO33/SRO bilayers deposited on STO in comparison with LSMO33 thin film grown on STO substrate by means of polarized soft x-ray absorption.

5.2 Synthesis and structural characterization

Epitaxial heterostructures of LSMO33/SRO were deposited on TiO_2 terminated STO (001) by PLD using stoichiometric targets of LSMO33 and SRO as explained in Section 4.1. The thickness and quality control of films have been monitored *in-situ* during the growth using RHEED. LSMO33 films of 2uc, 4uc, 8uc, 15uc (uc = unit cell) were deposited on 20uc SRO and are labeled from now on as 2/20, 4/20, 8/20, 15/20, respectively. For comparison, 4uc thick LSMO33 layer was deposited on non-ferromagnetic 3uc SRO (4/3). In addition, single layer of LSMO33 films of varying thickness were deposited directly on STO. The single layers LSMO33 film are labeled as 4/0, 8/0, 11/0, 25/0, where the first numbers correspond to the LSMO33 thickness in uc. One uc of LSMO33 and SRO corresponds to approximately 0.39nm [31]. Structural characterization of the heterostructures was done by XRD and XRR measurements.

Fig. 5.1(a) shows XRD $\omega - 2\theta$ scan along (001) reflection of STO for 2/20 and 15/20. The strong and sharp substrate peak is observed for both samples with LSMO33 and SRO film peaks appearing at higher and lower 2θ values, respectively, as expected from the strain state: tensile for LSMO33 layer and compressive for SRO. The thin films have broader peak compared to the substrate due to the reduced thickness.

To confirm the growth of fully strained film we obtained the reciprocal space map around (103), which are shown in Fig. 5.1(b). LSMO33 and SRO peaks are located at higher and lower Q_z compared to the substrate peak, respectively, in agreement with

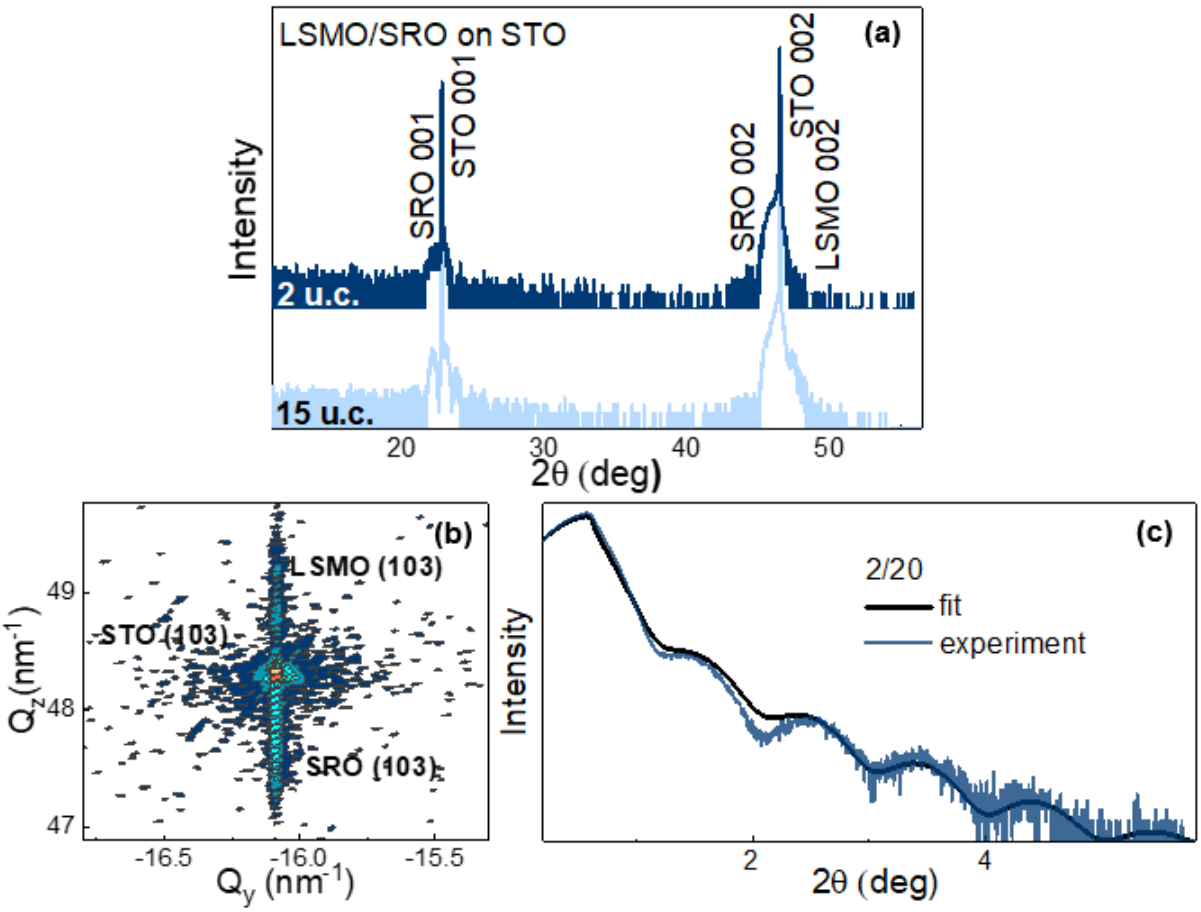

Figure 5.1: a) X-ray diffraction (XRD) $\omega - 2\theta$ scans for 2/20 and 15/20 b) XRD reciprocal space map along STO (103) of 15/20 c) XRR data and simulated curve for 2/20. Figure is taken from [66].

Fig. 5.1(a). All peaks fall at the same Q_y value indicating perfect in-plane matching and confirms that both layers are fully strained.

As an indication of the high-quality of the interface, in Fig. 5.1(c) black curve presents Kiessig fringe pattern on the 2/20 sample. The thickness determination of each layer based on fitting of reflectivity curves (Fig. 5.1(c), blue curve) is in agreement with the expected values and a roughness of 0.1-0.2nm was obtained for each layer.

5.3 XMCD study of magnetic properties

Further, when we discuss XA data, the Mn $L_{2,3}$-edge absorption spectra were obtained in TEY mode with the XA spectra defined as the sum of the spectra measured with different polarizations. The XMCD and XLD were normalized such that the corresponding maximum XA was at 1. Spectra were measured in grazing incidence geometry with a 30°

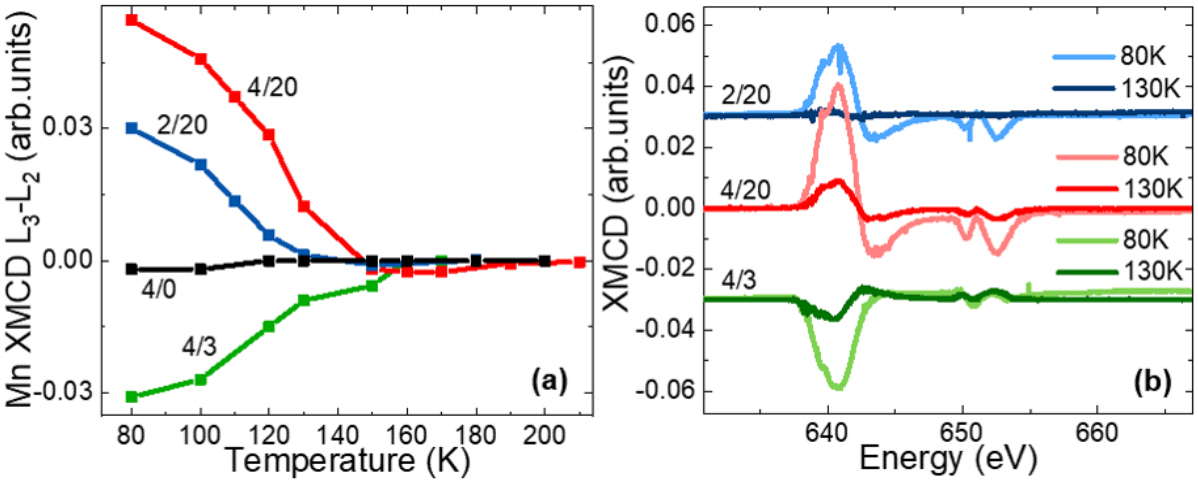

Figure 5.2: a) Difference between Mn XMCD intensity at L_3 and L_2 edges plotted as a function of temperature b) Mn $L_{2,3}$ XMCD comparison at two temperatures: 80 and 130K. Data in a) and b) were obtained in grazing incidence geometry at 50mT applied after saturation for ultrathin LSMO33 (2 and 4uc thick) for three different interface layers (0, 3, and 20uc thick). The XMCD spectra are displaced vertically for better visualization. Figure is taken from [66].

angle between the sample plane and incoming x-rays. The XMCD spectra was calculated as the difference between XAS measured with circularly polarized right and left x-rays. The XMCD were recorded with applied field of 6T or with 50mT after saturation at 6T. The magnetic field was applied parallel to the x-ray beam. 50mT field was chosen in order to measure in a field higher than the superconducting coil remanence which is around 10mT. All temperature-dependent XMCD data were measured after zero-field cooling.

To capture the T_C of the ultra-thin LSMO33 layers, XMCD spectra were measured at Mn $L_{2,3}$ edge, for both bilayers and single layers, at different temperatures, with an applied field of 50mT. The XMCD intensity difference, defined as the difference between its maxima/minima at L_3 and L_2 edge (L_3-L_2), is plotted in Fig. 5.2 as a function of temperature. As expected, 4/0 shows no measurable magnetic remanence down to 80K, while all other bilayers show magnetic remanence. Even the 2/20, which has LSMO33 thickness much below the single film critical thickness. The temperature at which XMCD response is vanished in Fig. 5.2(a) were found as 130K for 2/20, and 150K for 4/20 and 4/3. In Fig. 5.2(b) comparison between XMCD spectra measured at 80K and 130K confirms observation from Fig. 5.2(a) that the 2/20 has no significant remanence at 130K while 4uc LSMO33 on SRO is still magnetic and absolute value of the remanent moment is the same for 4/3 and 4/20. Therefore, T_C values that were found for the bilayers are indeed

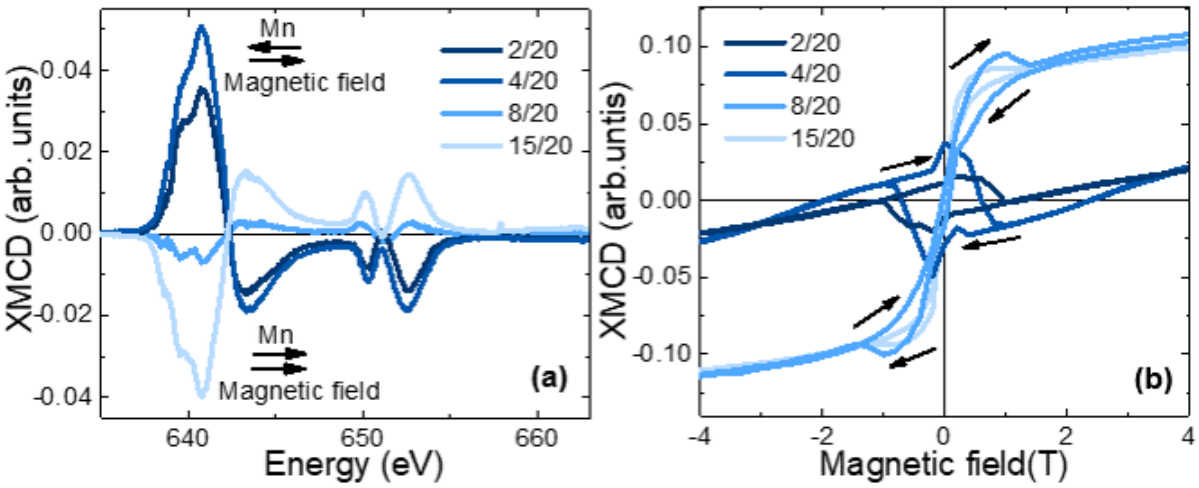

Figure 5.3: a) Comparison of Mn $L_{2,3}$ XMCD data measured at 25K in grazing in 50mT after 6T between LSMO33/20SRO bilayers with different LSMO33 thickness followed by b) magnetic hysteresis at the Mn L_3 edge measured in grazing incidence geometry. Arrows indicate direction of measurements. Figure is taken from [66].

lower than T_C in LSMO33 bulk, but they are clearly higher than T_C of thin LSMO33 single film of similar thicknesses, as previously observed [103]. Thus, we can conclude that LSMO33 magnetism recovers in ultra-thin limit when interfaced with SRO layer. This recovery happens even for films on 3uc SRO, where SRO is not ferromagnetic.

Interestingly, Mn XMCD signal in Fig. 5.2(a) and (b) is opposite for 4/3 compared to 2/20 and 4/20. In our geometry, this indicates that the Mn moment projection along the x-rays is oriented opposite to the field direction for 2/20 and 4/20, whereas 4/3 is along the field. This sign flip is a direct observation of the antiferromagnetic coupling between LSMO33 and SRO according to Goodenough-Kanamori rule. Theoretical calculation showed that this condition is energetically more favourable compared to any other [122, 123]. At 4/3 the Mn moment is parallel to the field since 3uc SRO is expected to be non-magnetic [44].

Next, we look at the magnetic properties of the bilayers for varying LSMO33 thickness while fixing SRO layer to 20uc thick. The XMCD spectra measured at 25K, 50mT is presented in Fig. 5.3(a) and the Mn hysteresis curves, measured by XMCD, are presented in Fig. 5.3(b). Das *et al.* [124] have also reported the hysteresis of LSMO33/SRO bilayers probed by XMCD, for thicker LSMO33 layers, showing similar shape as presented here. The data shown in Fig. 5.3 can be understood looking them as two sub-datasets: the thin LSMO33 layers (2/20 and 4/20) and the thicker LSMO33 layers (8/20 and 15/20). For the thin layers the sign of the XMCD at 50mT (Fig. 5.3(a)) evidences that the Mn moment is opposite to the applied field, as already observed in Fig. 5.2. From the

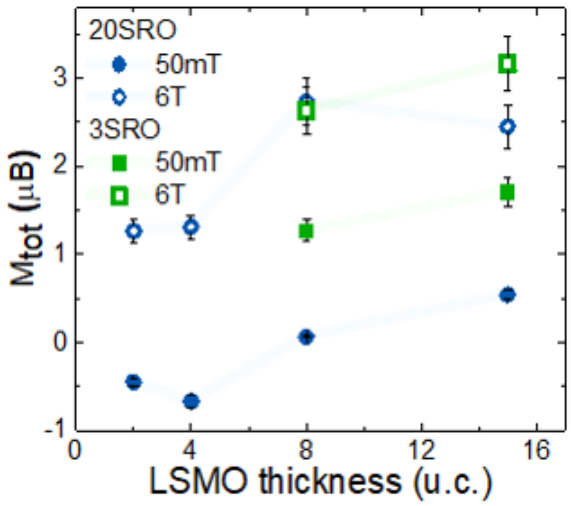

Figure 5.4: Total magnetic moment M_{tot} per Mn atom calculated as a sum of magnetic spin and orbital moment extracted from corresponding XMCD data at 25K in 6T and 50mT. Figure is taken from [66].

hysteresis (Fig. 5.3(b)) it can be seen that above 1T (2/20) and 2.5T (4/20) the magnetic field is strong enough to rotate the Mn moments with a projection parallel to the applied field, overcoming the antiferromagnetic coupling of Mn-Ru. For the thicker LSMO33 layers (8/20 and 15/20), the Mn moment projection is parallel to the x-ray beam and to the applied magnetic field for fields above 50mT, as evidenced both by Fig. 5.3(a) and (b). In addition, it can be seen from Fig. 5.3(b) that the thicker LSMO33 layers are not completely saturated, possibly because of the antiferromagnetic coupling of the interface layers with SRO.

The Mn total magnetic moment was calculated as the sum of spin and orbital contribution using Eq. (3.14) and (3.15). The number of Mn holes was taken as 5.5 from [125]. At the end, the spin moment value was corrected by a factor of 1.5 due to admixture of Mn L_2 and L_3 edges as it was discussed in Chapter 3. The results are shown in Fig. 5.4. The Mn saturated moment for 15/20 in Fig. 5.4 has been found to be $2.4\mu_B$, which is less than the expected value of $3.5\mu_B$. However, the saturated Mn moment found for 15/3 is $3.1\mu_B$, which is larger than for 15/20. The moments in low field are also larger for the layer interfaced with 3SRO than with 20SRO, as can be seen in Fig. 5.4. The explanation for this difference is that the interfacial layer of LSMO33 is always driven antiparallel to the applied field by coupling with 20SRO in our films regardless of LSMO33 thickness [124]. Top layers of LSMO33 on 20SRO for thicker LSMO33 layers tend to align with the field, resulting in the parallel moment projection observed in Fig. 5.3(b). Since 3uc of SRO is non-magnetic the AFM coupling at the interface does not take place and the

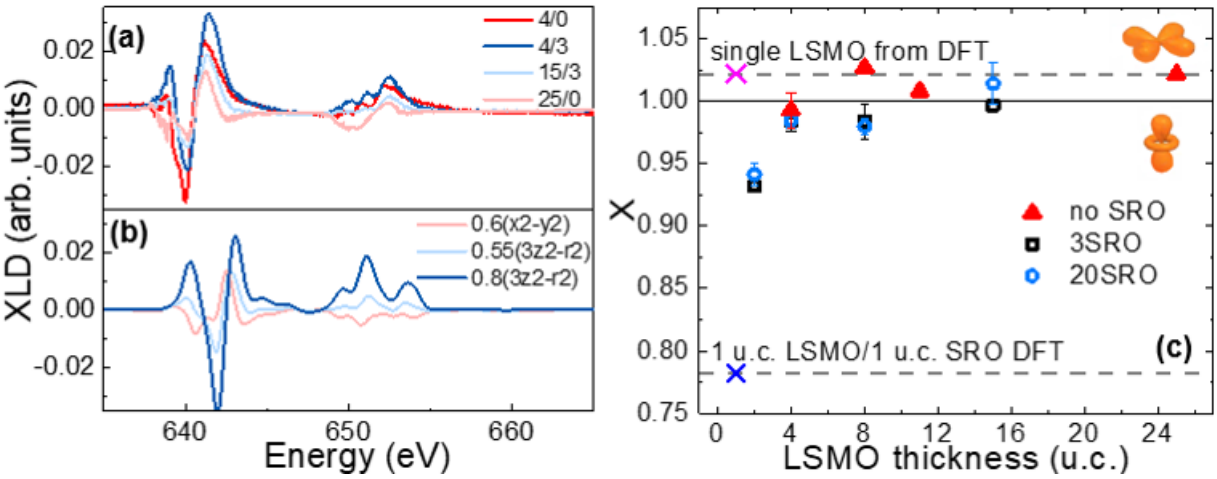

Figure 5.5: a) XLD data collected at Mn $L_{2,3}$ edges in grazing at room temperature b) corresponding linear combination of two simulations labeled as weight of the $3z^2 - r^2$ orbital c) calculated hole ratio X as a function of LSMO33 thickness calculated from experimental XLD data and from density functional theory (DFT) calculation from [123]. Figure is taken from [66].

moments of LSMO33 on 3SRO are larger.

5.4 Orbital occupation probed by XLD

Lv et al. have performed DFT calculations showing an orbital redistribution in Mn at LSMO33/SRO in comparison to single LSMO33 on STO [123]. In order to validate these calculations, we have investigated the orbital occupation using XLD at Mn $L_{2,3}$-edges (Fig. 5.5(a)) comparing two different bilayers as a function of LSMO33 thickness. In LSMO33 Mn^{4+} does not provide any XLD signal, since the e_g orbital is empty and t_{2g} is half-full. Therefore, the XLD signal represents the anisotropy of eg orbital in Mn^{3+} . The spectra in Fig. 5.5(a) are not well reproduced by the simulations for single orbital occupation presented in Fig. 3.7(a,b) using parameters from Tab. 3.1. This is due to the fact that both e_g orbitals are partially occupied. Therefore, we simulated the spectra by making a linear combination of the simulations, which is shown in Fig. 5.5(b). The differences among the XLD spectra measured for the various bilayers are subtle. In the following discussion, we focus on the differences at the L_2 edge since the XLD spectra is less complex. A single electron at the $x^2 - y^2$ would give a negative XLD at the L_2-edge, while $3z^2 - r^2$ occupation contributes to a positive XLD at the L_2-edge. We started by the thickest single layer measured, 25/0. For this film the XLD shows down-up feature, which is in agreement with simulation shown in Fig. 5.5(b) having the 0.6 weight from

$x^2 - y^2$ orbital occupied. For three other films presented (4/3, 15/3, and 4/0), the L_2 XLD is positive, which agrees better with the simulations where $3z^2 - r^2$ is occupied in majority.

For a quantitative interpretation of the XLD spectra, we have calculated the ratio X between holes at the two e_g orbitals $h(3z^2 - r^2)/h(x^2 - y^2)$ from Eq. (3.8). The values obtained for X are plotted in Fig. 5.5(c) as a function of LSMO33 thickness. X larger (smaller) than one indicates that in-plane (out-of-plane) orbitals have higher occupation. The simulation from Fig. 5.5(b) agrees with Fig. 5.5(c): the experimental data, which show $3z^2 - r^2(x^2 - y^2)$ orbital more occupied, indeed also show X<1(>1).

From Fig. 5.5(b) we see that there is a change of orbital occupation with thickness: 4 and 2uc thick LSMO33 films have out-of-plane orbital ordering while thicker films have in-plane orbital ordering. Since LSMO33 is tensile strained on STO substrate, from a pure strain point of view it is expected that the orbital occupancy should be dominantly from $x^2 - y^2$ orbitals. Indeed, the X value found for 25/0 matches with this prediction, and it is in very good agreement with theoretical DFT calculation for single LSMO33 film on STO. For thinner LSMO33 layers (<8uc) deposited on SRO we find a change of orbital contribution with a larger $3z^2 - r^2$ occupation for LSMO33, also in agreement with the prediction of an orbital rearrangement at the LSMO33/SRO interface [123]. However, the calculated values give approximately $15 - 20\%$ larger orbital asymmetry for 1uc LSMO33 on SRO, than what we measure for 2uc of LSMO33 on SRO.

In contrast to thick LSMO33//STO films (LSMO33>4uc), the XLD shape of 4/0 and the calculated X shows out of plane occupation, very similar to 4/3 (Fig. 5.5(a,b)). This agrees with previous observations on ultra-thin single LSMO33 that demonstrates orbital occupancy opposite to the one expected due to purely strain [113, 114, 117].

5.5 Determining Mn valence by XAS

Finally, we have also looked at the Mn valence for bilayers compared to single layers by comparing the XA spectra at Mn -edges. Fig. 5.6 shows XA spectra for 11/0, 4/0 and 4/20. The XA spectra from powder $SrMnO_3$ is also shown as a reference for Mn^{+4}. From Fig. 5.6 it can be seen that 11/0, 4/20 and 4/3 all have the maximum XA peaks at a similar energy. The energy position of XA peaks is lower than in Mn^{4+} of the reference sample, which is expected due to the mixed-valence of LSMO33 [124]. On the other hand, 4/0 has a clear energy shift, of about 0.4eV, towards lower energy evidencing a lower Mn valence state in 4/0 compared to the other films.

Here we point out that in the TEY detection, the signal decays exponentially with the distance from the surface due to the electron escape probability. Then, consequently, the

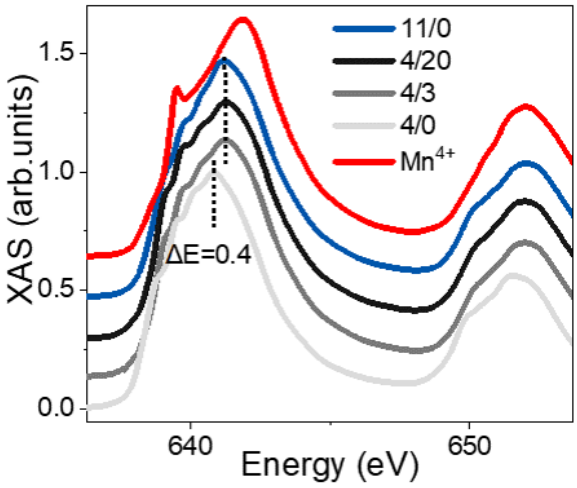

Figure 5.6: Comparison of XA spectra at Mn $L_{2,3}$ edges measured at 300K between 4uc LSMO33 interfaced with different SRO layers (0, 3, and 20uc thick) and reference data ($SrMnO_3$ and 11/0). The spectra are displaced vertically for better visualization. Figure is taken from [66].

relative contribution of the buried layers to the total signal decreases as the film thickness increases. Therefore, it is reasonable to assume that the energy shift between 11/0 and 4/0 is due to a higher Mn^{3+} concentration at the LSMO33//STO interface. This valence change with thickness is in agreement with previous results [116].

Since 4uc thick LSMO33 layer interfaced with SRO layer (20uc and 3uc) does not exhibit an energy shift compared to 11/0, we conclude that the nominal Mn mixed valence in LSMO33 is preserved through the entire thickness in the LSMO33/SRO bilayer. Such a valence stability could be evoked by increased charge transfer at the LSMO33/SRO interface. It is expected that due to extended nature of Ru 4d orbital, O 2p hybridizes more with Ru 4d than with Ti 3d [126]. At the same time, SRO is in the negative charge transfer regime meaning that Ru d4 is more likely to accept electron from O 2p rather than transferring its own electrons [43].

5.6 Discussion and Conclusion

Our XMCD measurements confirm that LSMO33 layer is magnetically dead for thickness of 4uc when grown on STO. However, once ultra-thin LSMO33 layer is interfaced with 20uc SRO layer (4/20 and even 2/20) the magnetic order is restored up to 150K indicating that the dead layer is reduced dramatically. It is important to notice that even when the SRO layer is not ferromagnetic the LSMO33 ferromagnetism is still preserved up to 130K, as in 4/3. In addition, our results suggest a change in LSMO33 moment orienta-

tion throughout the layer thickness with the moments close to LSMO33/SRO interface antiparallel to the applied field and the top layers parallel to the applied field. Our films are completely strained, as shown in Fig. 5.1 and indeed the orbital anisotropy measured for 11/0 agrees with LSMO33 in tensile strain (Fig. 5.5). The interface with SRO leads to out-of-plane orbital occupation, in qualitative agreement with DFT predictions [123]. However, 4uc LSMO33 on STO also shows out-of-plane orbital occupation, in agreement with previously reported studies [113, 114, 117]. In summary 4/0, 4/3 and 4/20 show very similar orbital occupation despite their contrastingly different magnetic properties. We discuss in sequence how this apparently contradicting result can be reconciled.

The out-of-plane orbital occupation in ultrathin LSMO33 on STO, has been previously observed and associated with C-type AFM ordering, where the crystal field splitting of the e_g levels lowers the $(3z^2 - r^2)$ orbitals [113]. In addition, the larger Mn^{3+} concentration observed at the interface would result in disrupted FM ordering in plane and loss of metallicity. SRO on STO grows on compressive strain and the energetic levels are such that Ru t_{2g} xz and yz orbitals are lower in energy [44]. Since in-plane orbital overlap between Mn 3d and Ru 4d is weak, only out-of-plane orbitals can contribute to Mn-Ru coupling. In LSMO33/SRO this orbital overlap allows for a 3D electronic structure, hindering quantum confinement effects [118]. The hybridized Mn 3d $3z^2 - r^2$ orbital drops below the $x^2 - y^2$, changing the sign of LSMO33 XLD, as observed here. Furthermore, LSMO33/SRO interface hinders the Mn valence reduction observed at the LSMO33//STO interface, and the nominal LSMO33 valence is preserved throughout the film thickness. In summary, the hybridization with the Ru orbitals coming from the orbital reconstruction, together with preservation of the Mn valence, help in reducing LSMO33 magnetic dead layer. In addition, the remaining Mn $x^2 - y^2$ occupation still allows for a strong Mn double exchange in the plane.

We have revealed the large impact of proximity and dimensionality, resulting in that the magnetic dead layer in LSMO33/SRO bilayers is drastically diminished. This restoration of magnetism in the ultra-thin LSMO33 layer could be associated with strong hybridization between LSMO33/SRO, hindering the quantum confinement effect. Even though the Mn orbital occupation in ultra-thin layers probed by XLD is the same, this orbital rearrangement has different origins and consequences. In LSMO/SRO bilayers it allows for a strong hybridization at the LSMO33/SRO interface leading to an effective Mn-Ru coupling. Additionally, in LSMO33/SRO bilayers, in contrast to LSMO33 single layers, the Mn valence is maintained throughout the thickness allowing for the preservation of the DE coupling in the plane.

Chapter 6

Interface control of the magnetic order in nickelate-manganite heterostructure

The NNO magnetic moment manipulation in nickelate-manganite heterostructure is a continuation of a joint project with M. Caputo and M. Radovic that has been published in [19], where we found unexpected ferromagnetism on NNO in NNO/LSMO33 bilayer [1]. In this chapter, we explore influence of strain, LSMO doping and NNO thickness in NNO/LSMO bilayers. This influence is examined by XAS, XMCD and RXMR techniques, and insights into magnetic coupling between Mn and Ni ions are revealed.

6.1 Introduction

Classically, when it comes to the interface between non-FM and FM compounds (or paramagnetic), people are interested in induced magnetism in non-FM layer and mech-

[1]My contribution to the paper in [19] was XMCD experiments on 5uc NNO/15uc LSMO33// NGO. Further, samples used in this chapter were fabricated by me, Dr. Milan Radovic, Dr. Marco Caputo, Dr. Eduardo Guedes and Dr. Teguh C. Asmara from the Spectroscopy of Novel Materials Group at PSI. TEM characterization of the samples was performed by Dr. Elisabeth Müller from the Electron Microscopy facility at PSI. XRD experiment was conducted by me and Dr. Laura Maurel from the Mesoscopic Systems Group at PSI. Electrical transport and AC susceptibility were done by Dr. Maria Luisa Medarde from the Physical Properties of Materials Group at PSI. XA and XMCD data were obtained at the X-treme beamline by Dr. Cinthia Piamonteze, Dr. Marco Capuro, Dr. Eduardo Guedes and me. Resonant reflectivity experiments were conducted by me and Dr. Cinthia Piamonteze at SIM beamline with support from Dr. Urs Staub, Dr. Nazaret Ortiz Hernández and Dr. Elizabeth Skoropata at PSI. Fitting of reflectivity data in DYNA program was performed by me with support from Dr. Jean-Marc Tonnerre from Institut Néel.

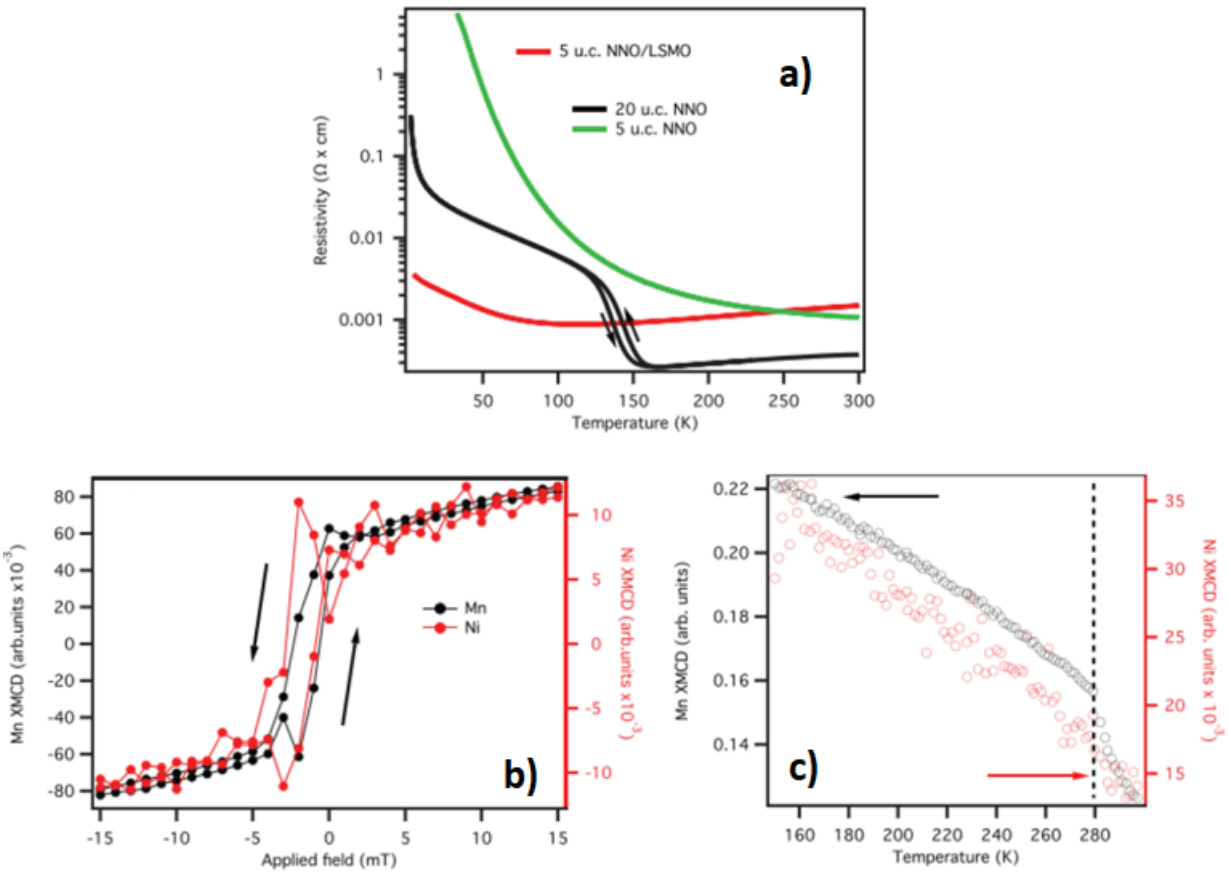

Figure 6.1: a) Temperature-dependent resistivity data on NNO systems. Comparison between the bulk-like 20 uc NNO//NGO, 5uc NNO//NGO and 5uc NNO/LSMO33//NGO b) magnetization loops measured by XMCD on the 5uc NNO/LSMO33//NGO sample on the Mn and Ni edges at 25K c) temperature dependence of Mn magnetization and Ni (red lines) in the 5uc NNO/LSMO33//NGO sample under 6.5 T magnetic field. Figure is taken from [19].

anisms driving this magnetic phase transition. For manganite-nickelate system emerged ferromagnetism is mostly seen in the context of charge transfer scenario and magnetic exchange interaction between Mn^{4+} -Ni^{2+} ions as in case of $LaNiO_3/LaMnO_3$ [**?**], $La_{0.7}Ca_{0.3}MnO_3/LaNiO_3$ [127] and $(La,Sr)MnO_3/LaNiO_3$ [128]. Besides, due to the correlation between magnetism and transport, by manipulating one, often one affects the other.

Previously, we found a ferromagnetic layer in usually AF NNO in 5uc NNO/15uc LSMO33 heterostructure deposited on $(110)_{or}$-oriented NGO as evidenced by XMCD in Fig. 6.1(b,c). From the transport study, rather metallic behaviour was observed in such a bilayer in comparison to a single layer NNO (Fig. 6.1(a)). It was also seen as a much smoother MIT transition in ARPES (Angle-Resolved Photoemission Spectroscopy) data

in comparison to a single NNO layer. Surprisingly, charge transfer effects were shown to play an insignificant role in driving NNO magnetism, unlike in many other manganite-nickelate studies, where Mn^{4+} -Ni^{2+} exchange and interfacial charge transfer were claimed to govern emerged ferromagnetism in the nickelate layer. Instead, we proposed demagnetizing field of LSMO33 to be the most important ingredient for Ni moments to align.

At the start of my thesis, we analyzed the temperature dependence of NNO magnetism for temperature values lower than shown in Fig. 6.1(c) and an unusual behaviour was observed, as discussed later in this section. At low temperatures (from 2K up to 100K) we noticed the moment decreases with decreasing temperature. We suggest that such a low-temperature behaviour might indicate recovering of AF coupling in ferromagnetic NNO further from the interface in addition to the FM interface. To verify this hypothesis, this sample was investigated by RXMR, which is described in Section 6.3. Moreover, we wanted to quantify the NNO magnetic layer thickness. To reproduce the observed effect and provide further clarification on how magnetism is realized in the NNO layer and how NNO magnetism can be configured continuation of this project was urged.

Increased thickness of the NNO layer could increase the chances of recovered AF ordering and would assist in determining the thickness of the magnetic layer in NNO by combining the surface sensitivity of TEY detection compared in different NNO thicknesses. Hence, as the first stage in Section 6.2, we vary NNO layer thicknesses (n=5,10uc) while keeping the LSMO33 layer unchanged. Further, we explore the effect of different strains by growing the bilayers on LAO in addition to different NNO thicknesses.

Further in Section 6.3, in addition to the variable NNO layer (n=5,10uc) LSMO33 doping was changed to become a ferromagnetic insulator (LSMO12) to identify the importance of conductivity in the proximity induced magnetism of NNO in non-FM/FM system. Furthermore, such a change would affect potential charge transfer through the interface via changed Mn^{4+} content. Finally, we analyze RXMR data on different samples with 5uc NNO to draw a comprehensive conclusion on Ni and Mn magnetic moment behaviour in the respective heterostructure.

6.2 NNO magnetic moment manipulation via strain

6.2.1 Structural characterization and electrical transport

In Chapter 3 we discussed dissimilarities between bulk materials and thin films. Both NNO and LSMO33 characteristics are strongly affected by both dimensionality and substrate choice, therefore newly discovered NNO ferromagnetism in NNO/LSMO33 heterostructure should be possible to configure by changing these parameters.

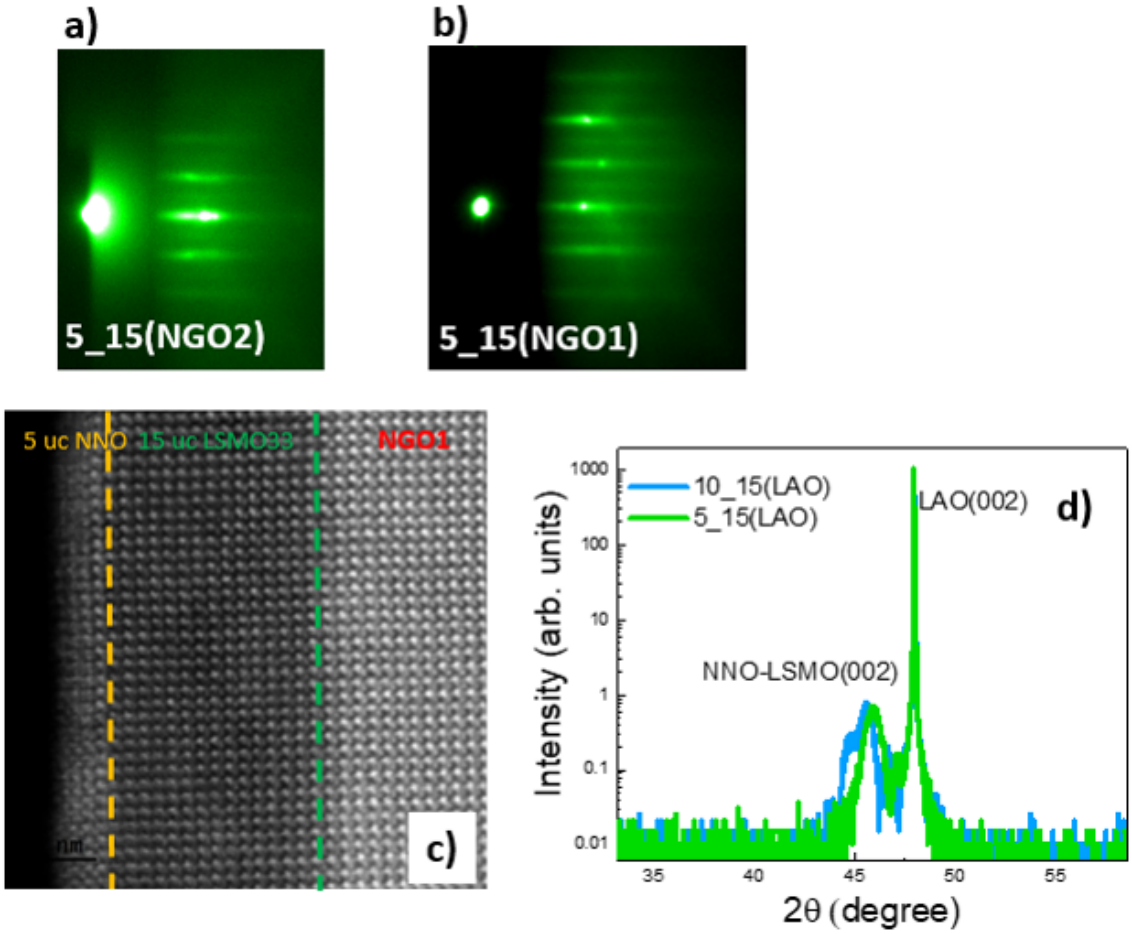

Figure 6.2: *In-situ* RHEED pattern of a) 5_15(NGO2) b) 5_15(NGO1), c) dark-field TEM image for 5_10(NGO1) and d) XRD $\theta - 2\theta$ scan for 5_10 and 10_15(LAO).

Initially, 5uc NNO/15uc LSMO33 deposited on NGO(110) bilayer was grown shortly before I started my thesis by M. Caputo. This sample was used in the publication [19] and will be labeled as 5_15(NGO1). Further, the growth of this system was repeated (5_15(NGO2)) adding an extra sample with 10uc NNO on top of 15uc LSMO33 (10_15(NGO2)). Another set of samples was grown on (100)-oriented LAO using two thicknesses 5 and 10uc of NNO keeping 15uc LSMO33 fixed (5_15(LAO) and 10_15(LAO)). All samples were prepared using the parameters given in Section 4.1.

The thickness and quality of the films were controlled by RHEED, TEM, XRD and XRR. In Fig. 6.2(a) and (b) elongated Bragg spots of 5_15(NGO1) and 5_15(NGO2) indicate a good surface quality. The slightly elongated spots point to a remaining roughness, which as seen by XRR is of the order of 0.2-0.5nm. TEM measurement of these samples in Fig. 6.2(c) confirms high crystallinity, sharp interfaces and the number of layers matching our expectations.

XRD was additionally used to check film quality and strain. The lattice constants

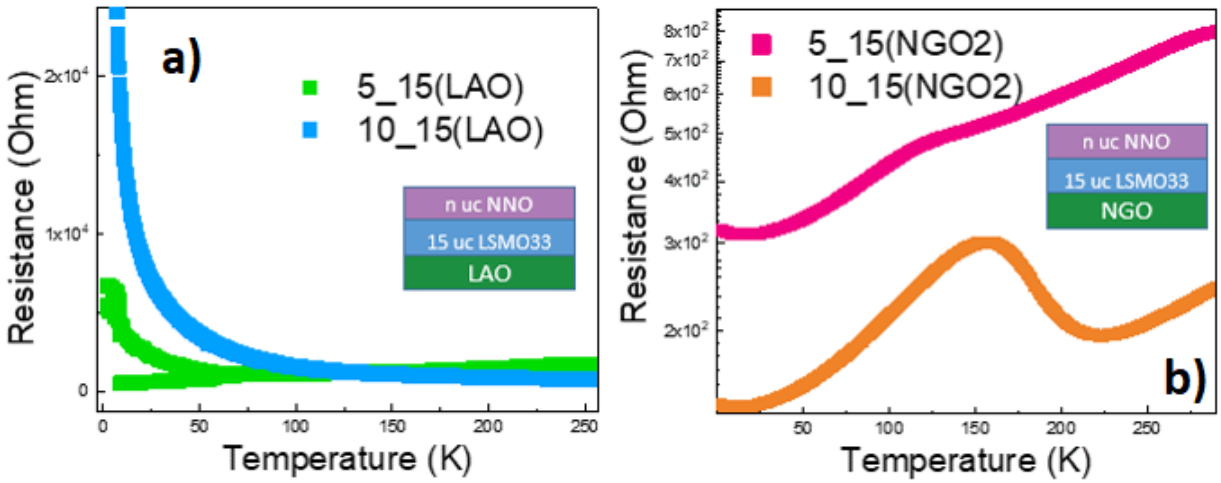

Figure 6.3: The temperature-dependent resistance measurement via cooling and warming for a) 5_15 and 10_15(LAO), b) 5_15(pink) and 10_15(NGO2).

of the substrate induce compressive strain on both NNO and LSMO when grown on LAO, while on NGO NNO has a tensile strain and LSMO is compressed (see Tab. 2.1). Fig. 6.2(d) shows out-of-plane diffraction along (002) direction for 5_15(LAO) and 10_15(LAO). In Fig. 6.2(d) we see LAO (001) substrate peak at 48° and the film at 46° for 5_15(LAO) and 45.6° for 10_15(LAO). The film peak is broad and seems to combine both contributions from NNO and LSMO due to similar lattice parameters. Subtracting out-of-plane lattice parameters for the substrate and the film from the XRD by Bragg law we get a_{LAO} ≈3.76Å and a_{LSMO} ≈3.87Å close to Tab. 2.1 confirming that LSMO film is fully strained as expected.

Fig. 6.3 presents electrical transport measured as a function of temperature while cooling and warming from 300K to 4K. The aim was to check if the films present MIT. In previous publications, thin NNO films deposited on LAO and on NGO upon decreasing thickness exhibit narrowing of the hysteresis with still visible MIT for 10uc and completely insulating behaviour throughout the whole temperature range for 5uc [19, 129].

In Fig. 6.3(a) sharp MIT was not observed for the samples on LAO. 5_15(LAO) exhibits upturn with hysteresis at low temperature and superimposed cooling and warming curves above 70K. Surprisingly, at the high-temperature 10_15(LAO) looks less resistant than 5_15(LAO). Both cooling and warming curves of 10_15(LAO) superpose at all temperatures. From the NNO layer alone we would expect opposite observations for 5 and 10uc NNO: no hysteresis on 5uc and narrow opening on 10uc.

A different picture is observed for the transport measurements of films deposited on NGO. Two samples with 5uc NNO on top (5_15(NGO1) and 5_15(NGO2)) seem to have similar behaviour (Fig. 6.1(a) and Fig. 6.3(b)) with no hysteresis opening and metallic-like

behaviour even at low temperature. Although no hysteresis was observed, 10_15(NGO2) exhibits a jump in resistance at around 150K. This jump might be addressed to the occurrence of MIT around 150K. A much less pronounced feature is observed in 5_15(NGO2) at around 120K.

Notice that even though we observed insulating-like behaviour on samples on LAO and more metallic-like on NGO, there is always an uncertainty in transport measurements of the bilayers in what we are probing: NNO or LSMO33. Therefore ARPES investigation would help to verify the more insulating state of samples on LAO.

6.2.2 Magnetic properties probed by XMCD

XMCD measurements provide information on magnetism at the bilayers with separated contributions from Ni and Mn. In this section XMCD spectra were measured in saturation at 6.5T and in remanence after saturation at 6.5T; in grazing geometry (30° angle between the sample plane and incoming x-rays) and in normal (90°); all after zero-field cooling. These measurement geometries probe the moment in-plane and out of plane, respectively. The XMCD spectra were normalized such that the corresponding maximum XA spectra was at 1. To visualize the evolution of magnetism in different sample sets with temperature we plot the difference between XMCD at L_2 and L_3 edges, which corresponds to the XMCD amplitude and therefore is proportional to the magnetic moment.

In order to probe the magnetic easy axis of LSMO33 and NNO, XMCD measurements were carried out in grazing and normal geometry. From previous publications, we expect the easy axis of single layer LSMO33 to be in-plane on NGO and out-of-plane on LAO [31]. For data measured in saturation XMCD in grazing and normal incidence is hardly distinguishable (data are not shown here). Therefore we have a closer look at data in remanence. For bilayers deposited on NGO we get an easy axis for LSMO in-plane as expected and NNO following LSMO33 (data are not shown here). For samples on LAO data are provided in Fig. 6.4. Mn XMCD intensity is stronger in normal incidence for single layer LSMO33(LAO) in Fig. 6.4(a) and for bilayers in Fig. 6.4(b). It means that the direction of the magnetic easy axis remains unchanged by adding an NNO layer on top and stays out-of-plane. Fig. 6.4(c) shows Ni edge XMCD in remanence and we see that the easy axis of NNO follows LSMO33 as well. From now on the geometry of XMCD measurements was kept following the magnetic easy axis of the film deposited on NGO or LAO respectively.

Fig. 6.5(a) compares Mn XMCD measured as a function of NNO thickness in normal incidence for films on LAO. Surprisingly, bilayers have a higher Mn remanent moment than a single layer despite the same LSMO thickness. In order to understand if this is

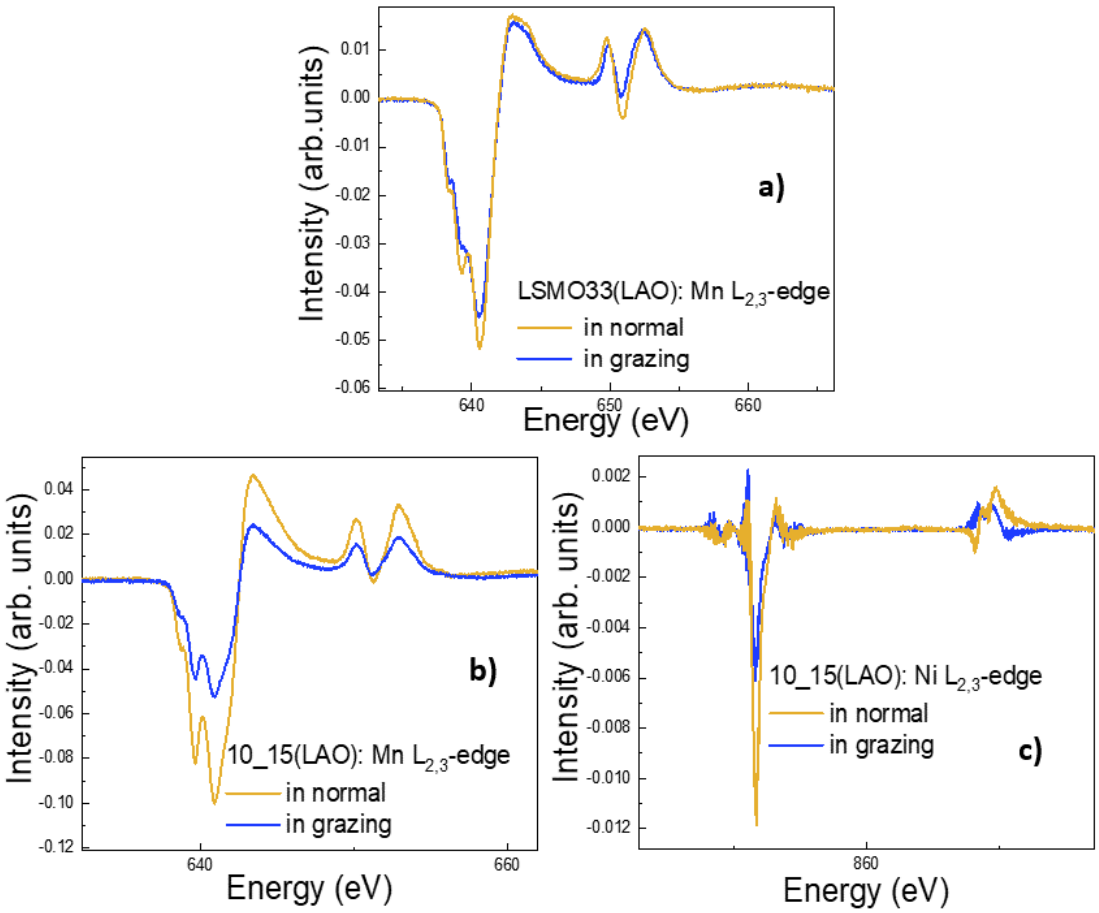

Figure 6.4: XMCD spectra measured in normal and grazing incidence at a) Mn $L_{2,3}$-edge LSMO33(LAO) b) Mn $L_{2,3}$-edge 10_15(LAO) c) Ni $L_{2,3}$-edge 10_15(LAO). All the spectra were taken at T=25K in remanence.

just a surface effect or not we performed XEOL (X-ray Excited Optical Luminescence) measurements of Mn XMCD. This technique allows measuring transmission-like spectra probing the whole thickness of the film [130]. We see a dramatic change in Mn XMCD between bilayers and single layer by a factor of four. Since XEOL data shows the same difference as XMCD it means that change in magnetism as a function of the top layer occurs through the whole thickness of the LSMO33 film. It is a very intriguing finding. Additionally, the difference appearing between 5_15(LAO) and 10_15(LAO) is displayed for both detecting techniques (Fig. 6.5(a,b)). Such an observation suggests the reconstruction of magnetism in LSMO33 as a function of NNO thickness and might be ascribed to a different coupling scheme between Mn and Ni ions. Thus, we continue with a more thorough XMCD analysis.

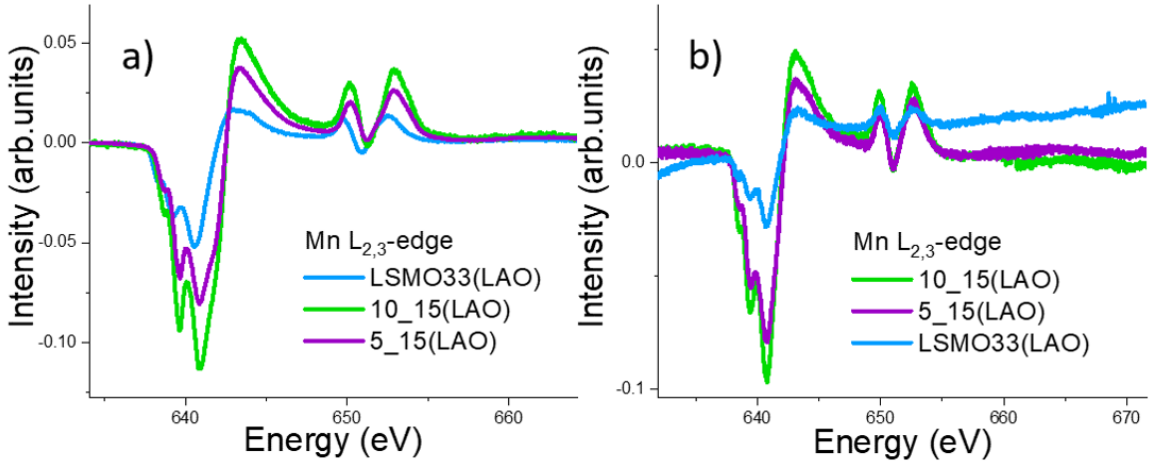

Figure 6.5: Mn $L_{2,3}$ XMCD as a function of NNO thickness taken in remanence in samples deposited on LAO substrate recorded in a) TEY mode at T=2K and b) XEOL mode at T=40K.

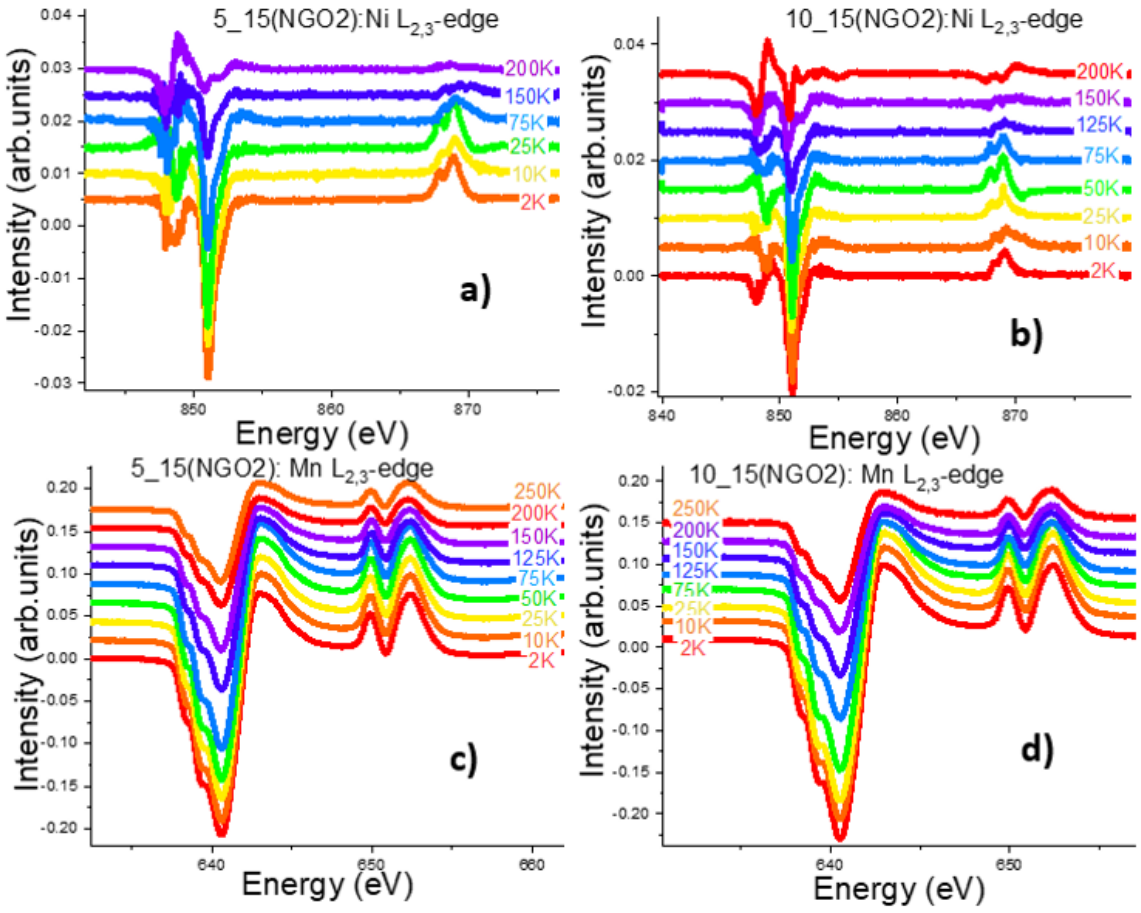

Figure 6.7: XMCD spectra as a function of temperature taken in grazing geometry in remanence a) Ni $L_{2,3}$-edge 5_15(NGO2) b) Ni $L_{2,3}$-edge 10_15(NGO2) c) Mn $L_{2,3}$-edge 5_15(NGO2) d) Mn $L_{2,3}$-edge 10_15(NGO2). The spectra are displaced vertically for better visualization.

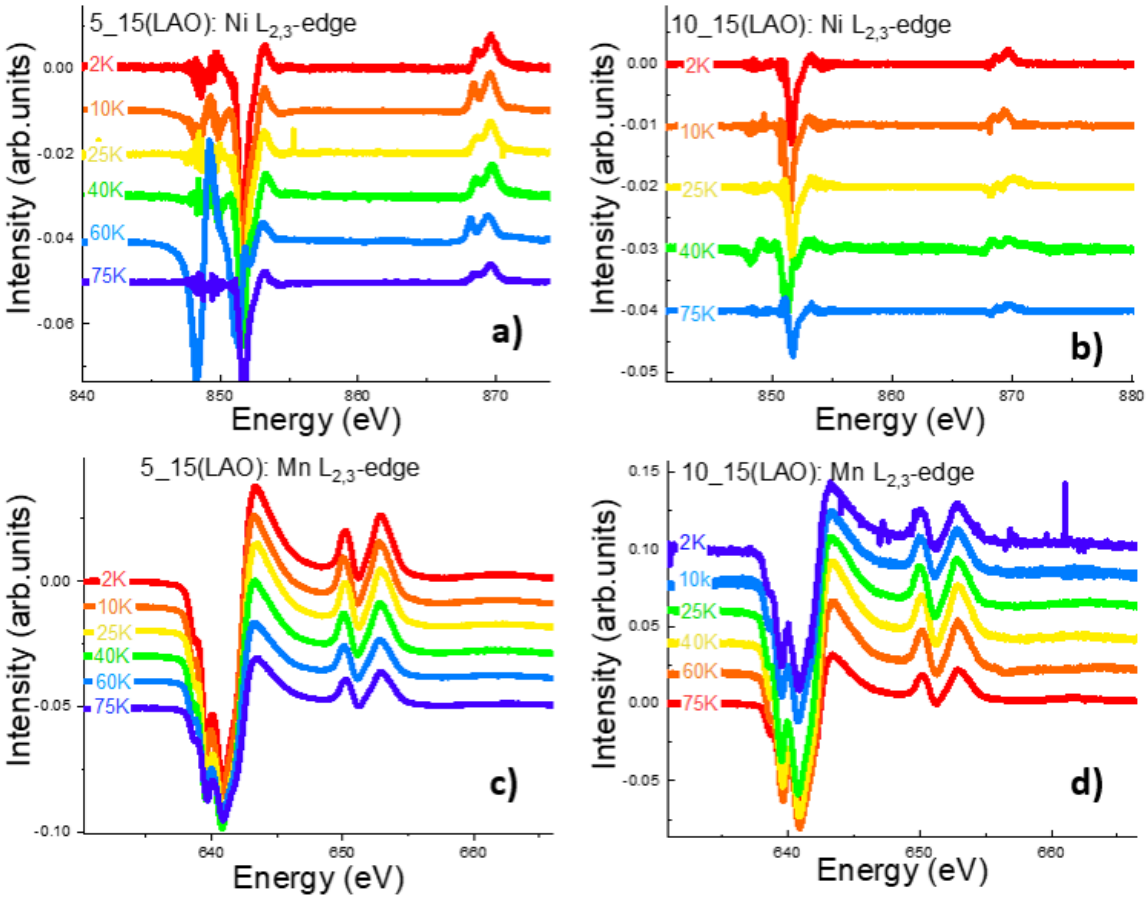

Figure 6.6: XMCD spectra as a function of temperature taken in normal geometry in remanence at a) Ni L_2-edge 5_15(LAO) b) Ni L_2-edge 10_15(LAO) c) Mn L_2-edge 5_15(LAO) d) Mn L_2-edge 10_15(LAO). The spectra are displaced vertically for better visualization.

In Fig. 6.6 and 6.7 we show the remanent XMCD signal at Mn and Ni over a long range of temperatures on LAO and NGO varying NNO thickness. Although the data quality across the Mn edge is excellent, across the Ni edge it suffers from a generally lower signal and La M_4-edge contribution. However, after baseline treatment, the quality of data across the Ni edge is very good with both edges clearly visible. The negative XMCD sign at both Ni and Mn L_3-edges indicates that Ni and Mn are coupled ferromagnetically.

To add to the discussion on magnetism on LAO we introduce here temperature-dependent magnetization as a function of NNO thickness. Fig. 6.8 illustrates L_2-L_3 difference XMCD plotted as a function of temperature for Mn and Ni edge in remanence (a,b) and in saturation (inset). We see that despite coincided saturated data (see inset in Fig. 6.8(a)) Mn in 10_15(LAO) has a larger remanent magnetic moment than 5_15(LAO) over the whole temperature range. The Ni reflects the opposite behaviour to Mn: the higher the Mn moment in a bilayer, the lower the Ni moment. It can be simply explained

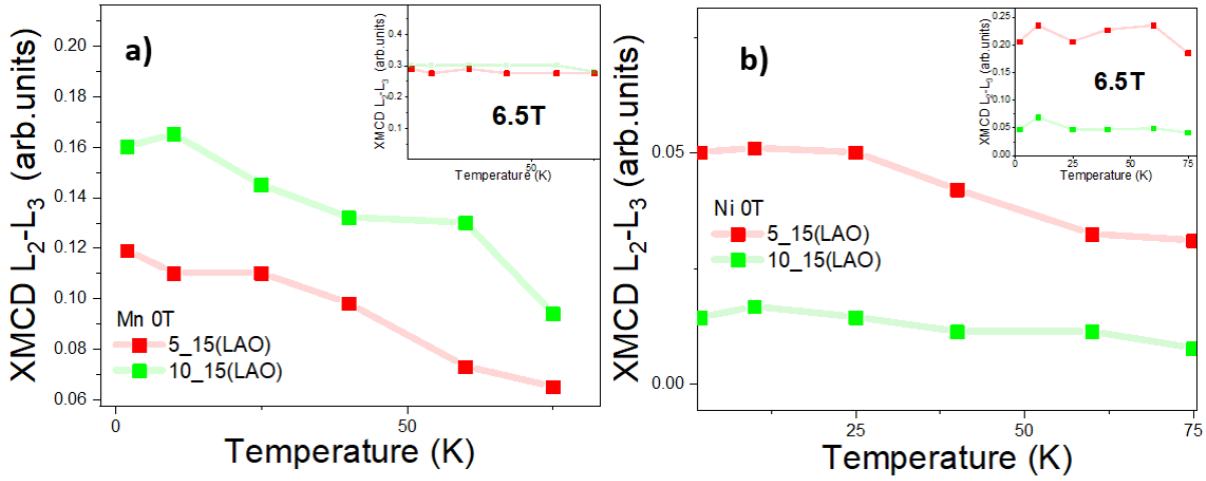

Figure 6.8: The L_2-L_3 difference versus temperature in remanence measured in normal on samples deposited on LAO measured a) at Mn edge (inset: in saturation at 6.5T) b) at Ni edge (inset: in saturation at 6.5T).

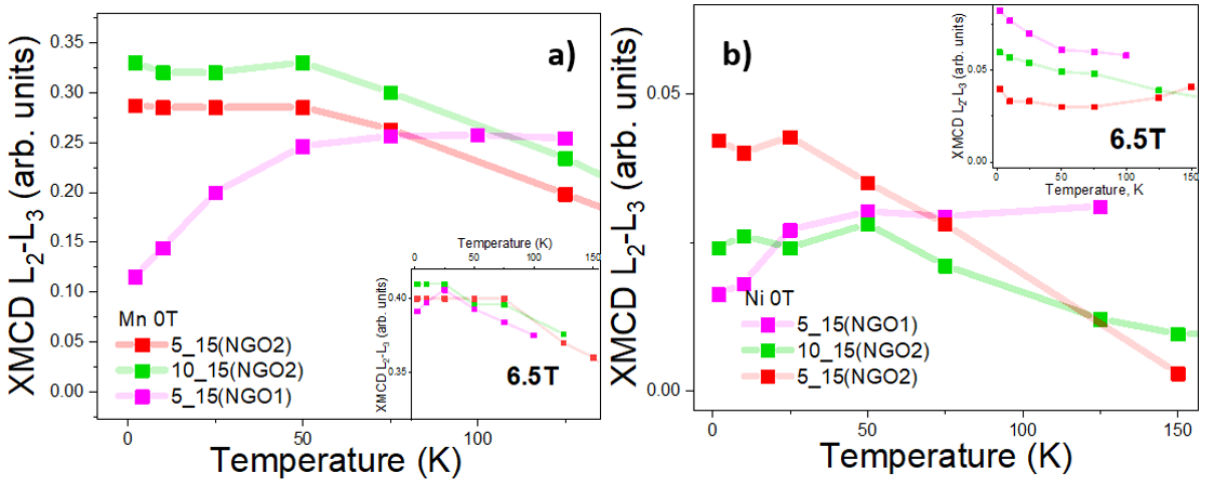

Figure 6.9: The L_2-L_3 difference versus temperature in remenence measured in grazing on samples deposited on NGO measured a) at Mn edge (inset: in saturation at 6.5T) b) at Ni edge (inset: in saturation at 6.5T).

by probing depth of NNO in TEY mode, where the XMCD signal drops exponentially. If we assume the NNO ferromagnetic layer is concentrated at the interface with LSMO33, its contribution to the TEY signal would decrease the thicker NNO layer.

Samples on NGO in Fig. 6.9(a, inset) show that the Mn magnetization as a function of temperature in saturation is the same for all films. As it was noted in the introduction of this section Mn and Ni have unusual low-temperature behaviour in 5_15(NGO1) (that can be observed in Fig. 6.9(a,b) in pink). We expected to reproduce this behaviour in a new 5_15(NGO2). However, the new sample 5_15(NGO2) (Fig. 6.9(a,b) in red) does

Table 6.1: Sum of the orbital and spin magnetic moment for each sample extracted by sum rules from 6.5T applied field XMCD taken at 25K.

	Mn (μ_B)	Ni (μ_B)
LSMO33(LAO)	2.5±0.3	•
5_15(LAO)	2.9±0.3	0.6±0.06
10_15(LAO)	2.7±0.3	0.3±0.03
5_15(NGO1)	3.5±0.4	0.2±0.02
5_15(NGO2)	3.8±0.4	0.07±0.007
10_15(NGO2)	3.14±0.3	0.08±0.008

not show the same L_2-L_3 increase as 5_15(NGO1), despite all similarities in electrical transport and structural characteristics. The difference between the two samples from the different rounds of preparation remains unclear. One scenario could explain this difference by moment frustration at the interface in one case and its absence in the other case. Another scenario may suggest a very fine difference in structural parameters that adjust local magnetic moments differently in these two films. To resolve this mystery we return to this question in Section 6.3 comparing RXRR and RXMR on these samples. In addition to different low-temperature behaviour, we observe different T_C of Ni for these samples. Magnetization of 5_15(NGO2) drops to zero already at 150K, while it is still non-zero for 5_15(NGO1) and 10_15(NGO2). Saturated data at Ni edge follows the opposite trend as remanent data. Especially for 5_15(NGO2) which has the strongest magnetization in remanence and the lowest in saturation.

To interpret remanent and saturated data as a function of NNO thickness we compare the element-specific magnetization curves (Fig. 6.10) at the Mn and Ni edge for both sets of samples. The similarity of the hysteresis loop shape measured for Mn and Ni demonstrates a strong ferromagnetic coupling between the Mn and the Ni for all samples. As it can be seen, the saturated moment is always bigger for 5uc NNO regardless of a substrate at both edges. Fig. 6.10(a,b) show hysteresis on samples deposited on NGO fully saturated at 2T. No coercivity was detected due to the precision of the measurement. Saturation for a sample with 5uc NNO is twice as high than for film with 10uc NNO for both: Mn and Ni. On the other hand, in Fig. 6.10(c,d) a significant hysteresis is observed for all samples on LAO. While Mn hysteresis for 5_15(LAO) is fully saturated at 2T, Ni in 5_15(LAO) and both edges in 10_15(LAO) exhibit ferromagnetic hysteresis with a diagonal paramagnetic-like contribution. The film with 5uc NNO has three times larger saturation than the film with 10uc NNO at both edges.

Until now we evaluated only the qualitative behaviour of the magnetization as a func-

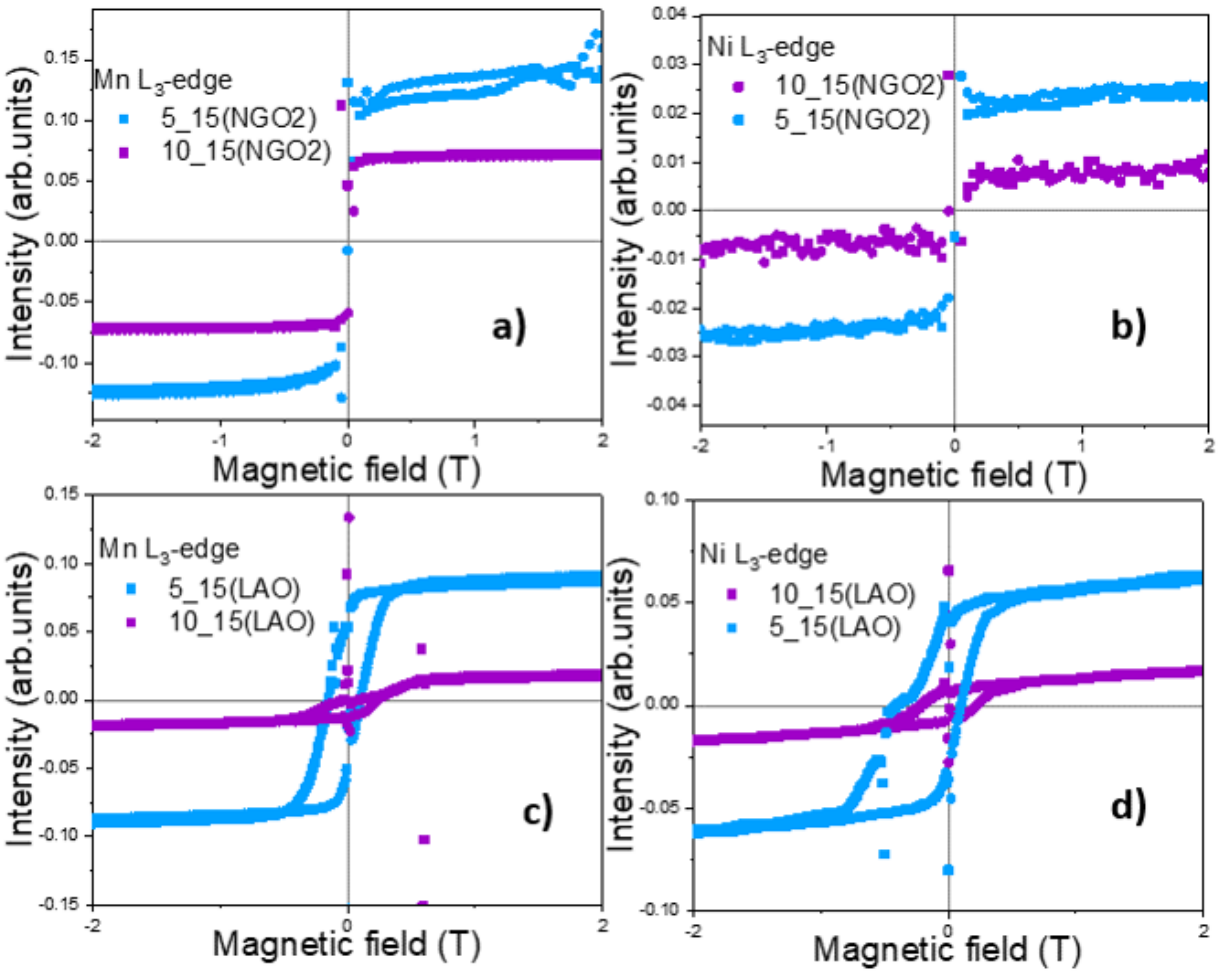

Figure 6.10: Magnetization curves measured in grazing incidence on samples deposited on NGO a) at Mn edge b) at Ni edge and measured in normal incidences on samples deposited on LAO c) at Mn edge d) at Ni edge. All the spectra were taken at T=25K.

tion of temperature, thickness and magnetic field. Sum rules help us to quantify these changes. XMCD sum rules from Eq. (3.14) and (3.15) have been applied to both the Ni and Mn spectra. Saturated Mn and Ni total magnetic moments extracted by sum rules are given in Tab. 6.1 with the error bar of 10%. For the analysis number of holes was taken as 5.8 for Mn and 2.2 for Ni. These values lie approximately between Mn^{3+} and Mn^{4+}; between Ni^{2+} and Ni^{3+}. L_3 and L_3+L_2 integrals were calculated in energy range 850-860eV and 850-890eV respectively. Mn moment is in good agreement with a reported value of $3.2\mu_B$ for LSMO33 within the error bar. We can clearly see a reinforcement of the Mn magnetic moment in the bilayers on LAO in comparison to a single layer. Ni magnetic moment was found to be twice smaller in 5_15(NGO2) than in 5_15(NGO1). For LAO samples Ni magnetic moment differs by a factor of two between 5_15(LAO) and

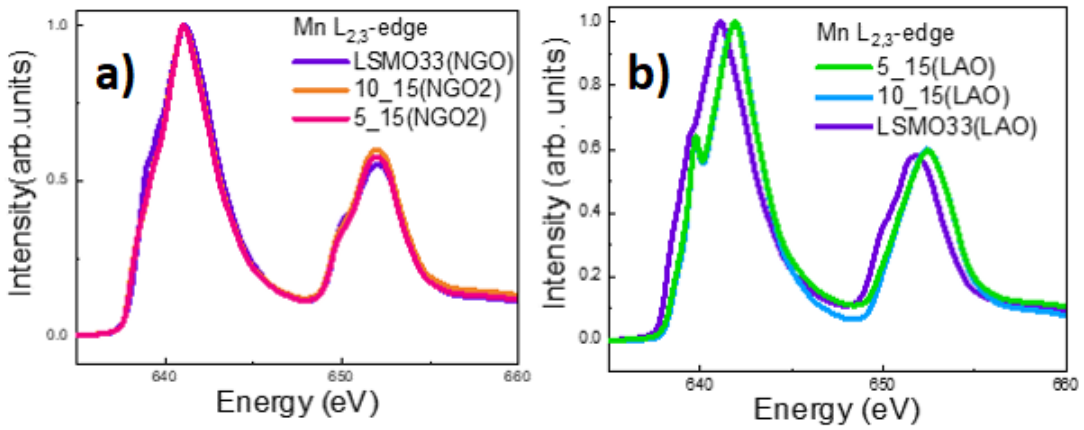

Figure 6.11: XA spectra at Mn $L_{2,3}$-edge a) bilayers deposited on NGO substrate are compared to a single layer LSMO33 b) bilayers deposited on LAO substrate are compared to a single layer LSMO33.

10_15(LAO). The order of magnitude of Ni magnetic moment on average is in agreement with what was reported before on Ni in manganite-nickelate systems [**?**, 131].

6.2.3 Electronic structure and charge transfer probed by XAS

To prove or disprove the charge transfer scenario at the interface between LSMO33 and NNO XA spectra were taken at Mn and Ni edges. It illustrates valence change for Ni and Mn that also serves as an indication of charge transfer.

Room-temperature XA obtained as the sum of XA intensity measured with two polarization from bilayers is compared to a single layer LSMO33 at Mn edge in Fig. 6.11. Samples deposited on NGO in Fig. 6.11(a) demonstrate very similar spectral shape without big change between single layer and bilayers ascribing very little charge transfer in such systems. Nevertheless, samples on LAO in Fig. 6.11(b) demonstrate remarkable energy shift for bilayers compared to the single layers. From the previous works [131, **?**], we know that this shift to higher energy means more Mn^{4+} content and is an indication of interfacial charge transfer.

In the next step, we introduce XA spectra across the Ni edge taken at room temperature. Bilayers, NiO powder, and 30uc NNO film (bulk-like) are compared in Fig. 6.12. Fig. 6.12 shows Ni XA spectra from bilayers compared to reference samples with Ni^{2+} (powder) and NNO (film). The La M_4 peak (at 849 eV) partially overlaps with Ni L_3 (centered at 852.3eV). Therefore, the La M_4 peak was fitted by Lorentzian (as schematically shown in Fig. 6.12(a)) and removed from Ni XA spectra to enable correct analysis, especially between bilayers deposited on a different substrate with different La contribution. Fig. 6.12(b,d) show L_3 edge, while (c,e) show L_2 comparison.

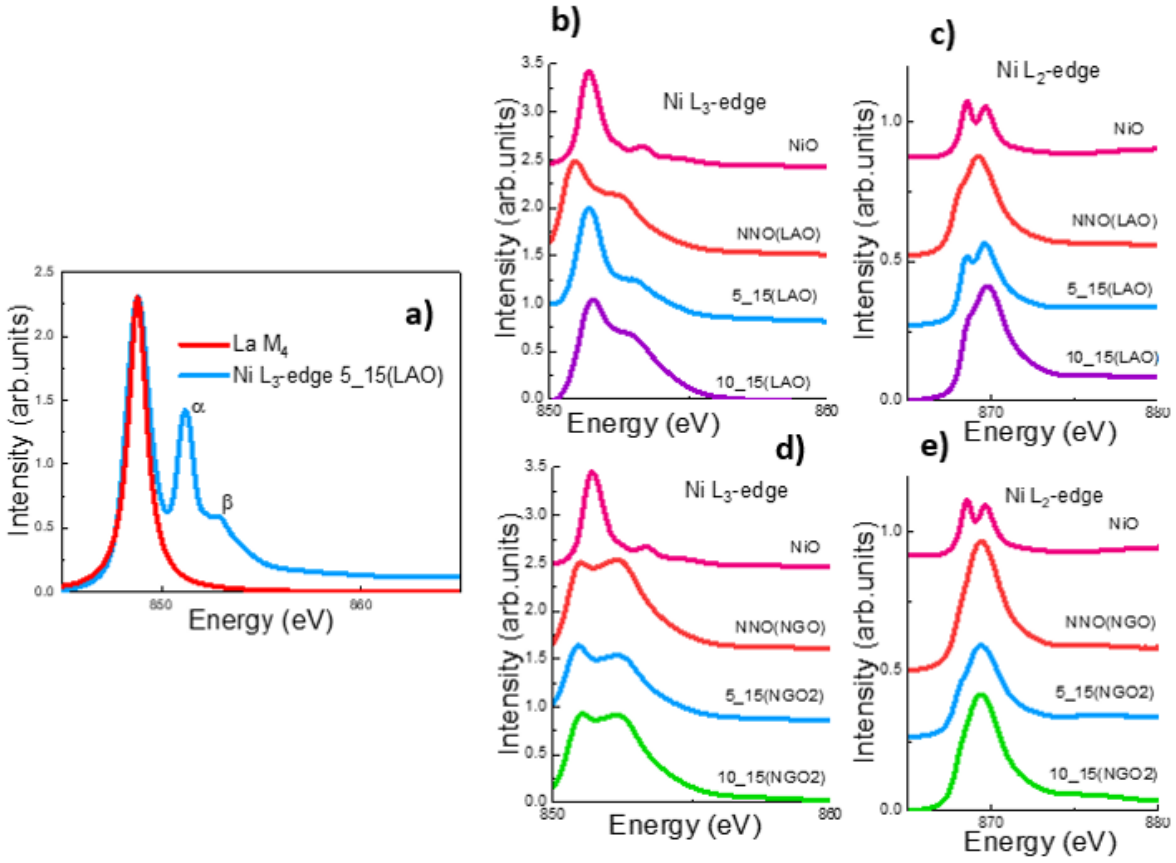

Figure 6.12: The set of XAS spectra at Ni $L_{2,3}$-edge a) example of La M_5 peak subtraction and two Ni L_3 shoulders labeled as α and β; comparison between NiO powder, NNO bulk-like film, and bilayers at room deposited on LAO and NGO at b,c) L_3-edge and d,e) L_2-edge respectively. The curves are displaced vertically for better visualization.

Shoulder of Ni L_3 peak at 851.4eV of NiO corresponds to Ni^{2+} and Ni L_3 peak at higher energy 852.4eV of NNO corresponds to Ni^{3+} as can be seen in Fig. 6.12(b,d). In Fig. 6.12(b) L_3 in 5_15(LAO) and 10_15(LAO) exhibits same position as NiO at room-temperature. 5_15(LAO) resembles more closely NiO shape than NNO at room temperature. Same trend is observed at L_2 edge (Fig. 6.12(c)). L_2 resolved double-peak featuring NiO was found in both 5 and 10uc, although for 10uc the L_2 peak is clearly more Ni^{+3}-like than for 5uc. It is an indication of Ni^{3+} component that increases as the thickness of the NNO layer increases. It can be interpreted as the localization of some of Ni^{2+} at the interface.

In contrast to samples on LAO Fig. 6.12(c) demonstrate NNO bulk-like shape across L_3 for all samples on NGO at room temperature with a very small contribution of Ni^{2+} on 5uc that is even lowered in 10uc NNO. In Fig. 6.12(e) L_2 edge agrees with observation at L_3 edge.

6.2.4 Discussion

We ascertained a significant difference in the amount of charge transfer at the nickelate-manganite interface as a function of strain. From transport measurements, samples under compressive strain seems more insulating than under tensile strain. It agrees with previous finding on single NNO film under different strain by L. Wang *et al.* [132]. Additionally, it was shown that relatively bigger Ni^{2+} component promotes insulating state in nickelates [133]. LAO substrate and thus lattice distortion due to strain result in establishing Mn^{4+} -Ni^{2+} charge transfer as was evidenced by XA spectra at Ni and Mn edges.

This difference in charge transfer leads to an enhancement of magnetic properties for LAO samples. Ni in 5uc NNO deposited on LAO possesses a magnetic moment of $0.6\mu_B$ that is three times higher than the highest magnetic moment observed in samples on NGO. Interestingly, it happens despite LSMO33 being less magnetic in samples on NGO than on LAO with magnetic moment $3.5\mu_B$ on NGO against $3\mu_B$. The difference of $0.5\mu_B$ might be addressed to different effects. Having assumed complete spin alignment of Mn in high-spin state values of the magnetic moment were calculated for Mn^{4+} and Mn^{3+} as $3\mu_B$ and $4\mu_B$ respectively. Therefore, a relatively higher contribution of Mn^{4+} in samples on LAO would lead to a reduction of overall magnetic moment on LSMO33. Moreover, it can be also an effect of a larger strain then on LAO. As shown in previous work [110] LSMO33 single film on LAO has lower T_C than on NGO.

Ni magnetization curves claim saturation to be lower for 10uc NNO. We see a clear reduction of the Ni magnetic moment as a function of NNO thickness, therefore we assume magnetism to be concentrated at the first layers at the interface with LSMO33. If we take into account the exponential decay of the TEY signal from Eq. (4.3), we obtain a nearly 50% drop of the signal for 10uc NNO coinciding with a difference in Ni magnetic moment between 5uc and 10uc NNO for both substrates. Therefore the moment is concentrated at the interface.

5_15(NGO1) shows an unusual magnetic behaviour at low temperature. This deep in Mn and Ni magnetic moment on 5_15(NGO1) can be assigned to establishing the AF phase in NNO or more precisely canted ferromagnetic phase in both NNO and LSMO33 when deposited on NGO below T_N of NNO which is expected to be at 75K [134]. This behaviour is not quite reproduced in 5_15(NGO2). The magnetism in these two films are further investigated by RXMR in the next chapter.

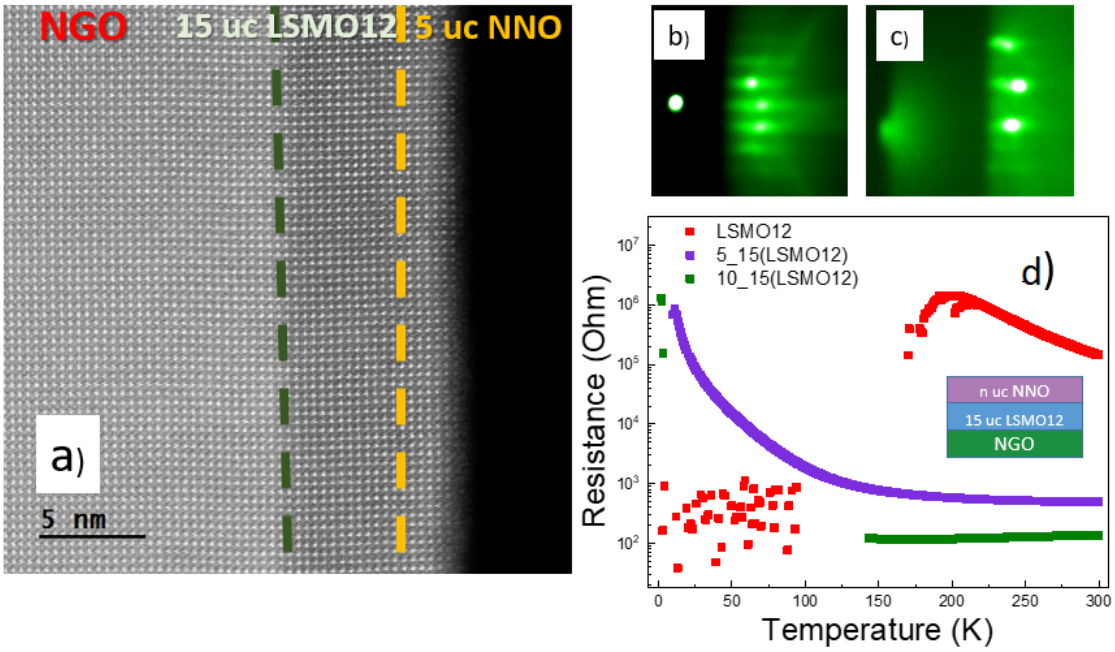

Figure 6.13: Pre-charachterization of a) 5_15(LSMO12) sample by TEM dark-field imaging; RHEED pattern for b) LSMO12 and b) 5_15(LSMO12) samples; c) the temperature-dependent resistance measurement via cooling and warming for LSMO12 (red), 5_1(LSMO12) (violet) and 10_15(LSMO12) (green).

6.3 NNO magnetic moment manipulation via LSMO doping

In this section, we focus on the investigation of samples deposited on NGO. In addition to samples with LSMO33, we include samples with LSMO12 trying to link emerged magnetism in NNO with the conductivity of the layer underneath. In order to do so high-quality epitaxial thin films of NNO/LSMO12 have been grown on $(110)_{or}$-oriented NGO substrate. LSMO12 thickness is fixed to 15uc., NNO was 5 and 10uc similar to samples with LSMO33. In addition, films were capped with 6nm of carbon to avoid charging problems during the measurements. Films will be denoted as LSMO12 for 15uc LSMO12 single layer, 5_15(LSMO12) and 10_15(LSMO12) for 5uc and 10uc NNO deposited on LSMO12. Note that the samples on LSMO33 are the same as from the previous section and they are named 5_15(NGO1), 5_15(NGO2) and 10_15(NGO2).

The thickness and quality of the films were controlled by RHEED and TEM. In Fig. 6.13(a) TEM image shows high crystallinity and nearly ideally sharp interfaces between each layer. The difference between LSMO12 and NNO atoms cannot be seen from a dark-field image, because the lower content of Sr made them indistinguishable in compar-

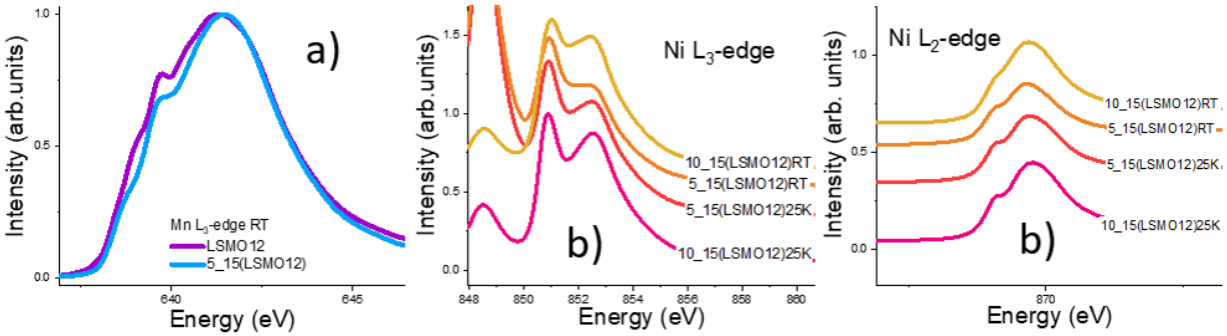

Figure 6.14: XA spectra a) at Mn L_3-edge for 5_15(LSMO12) compared to a single layer LSMO12 taken at room-temperature b) at Ni L_3-edge (left) and at Ni L_2-edge (right) comparing 5_15(LSMO12) and 10_15(LSMO12) at room temperature and 25K. The curves at Ni $L_{2,3}$ edge are displaced vertically for better visualization.

ison to the sample with LSMO33. However, additional EDX measurements helped us to differentiate these two layers (not shown here). RHEED pattern on LSMO12 alone and in bilayer show symmetric dots that confirm the smooth interface of our films (Fig. 6.13(b)).

Transport measurements indicate a highly insulating state of LSMO12 (Fig. 6.13(c)). Measurements were not possible below 200K. In addition, 5_15(LSMO12) (Fig. 6.13(c)) demonstrates insulating behaviour similar to a thin NNO single layer through the whole temperature range with no sign of MIT. 10_15(LSMO12) could be measured only down to 170K (Fig. 6.13(c)).

6.3.1 Electronic structure and charge transfer probed by XAS

First, we are going to discuss the electronic configuration of bilayers with LSMO12 and compare with what we observed for bilayers with LSMO33. XA spectra presented here are calculated as sum of XA intensity measured with different polarizations and normalized by the maximum of the signal. Data on LSMO12 samples are presented in Fig. 6.14(a) comparing XA spectra across Mn edge at room temperature between single LSMO12 and 5_15(LSMO12). As can be seen, Fig. 6.14(a) demonstrates an energy shift of 0.1eV between Mn XA spectra of the single LSMO12 and the bilayer. This indicates that, similarly to LSMO33, there is slightly more Mn^{4+} in the bilayer compared to the single layer. Notice that comparing Mn XA spectra between LSMO12 and LSMO33 the energy shift is 0.2eV because of the difference in doping and therefore different Mn^{3+}/Mn^{4+} ratio.

Fig. 6.14 (b) and (c) compares XA spectra across Ni spectra for L_3 and L_2 edges respectively. We will focus on the discussion of L_2 edge due to previously mentioned problems with La M_4 contribution. Ni XA spectra in Fig. 6.14(c) provide a comparison between

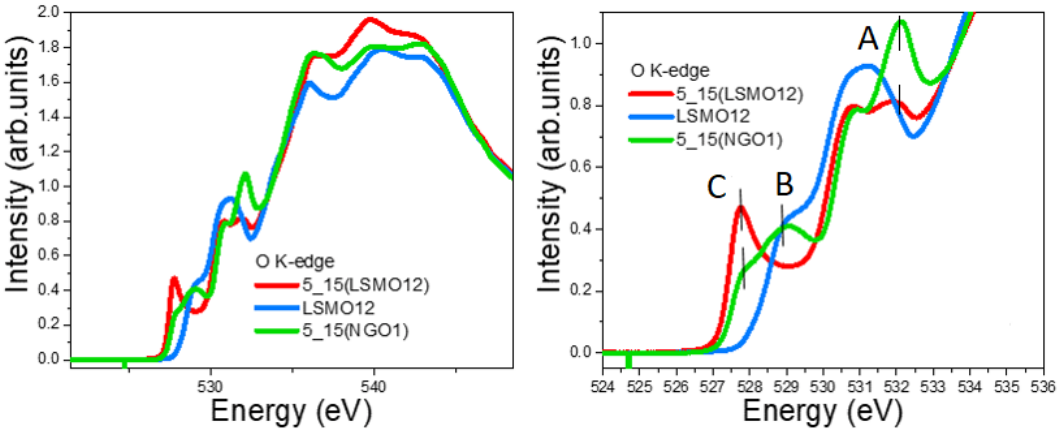

Figure 6.15: Comparison of room-temperature XA spectra at O K-edge between single LSMO12 film and bilayers 5_15(NGO1), 5_15(LSMO12) and 10_15(LSMO12)(left) for the whole range of 520-555eV and (right) for pre-peak energy range.

5_15(LSMO12) and 10_15(LSMO12) at room and low temperature. In Fig. 6.14(c) we see that the behaviour of the samples with LSMO12 is very similar to the samples with LSMO33. The shape of the L_2 edge resembles very well NNO single film and the energy position of both shoulders of L_2 edge remains at the same energy as for single NNO films also at low temperature. In addition, we observed sharpening of the L_2 as we expect from NNO entering an insulating state [135]. This sharpening is very clear in the L_3 edge as well.

Properties of TMOs are governed by their interaction with 2p levels of oxygen. Here, we try to get insight into the hybridization of 3d Ni and Mn with O 2p states by looking at the O K-edge of samples with different LSMO doping: 5_15(LSMO12), 5_15(NGO1) and a single LSMO12 film. In Fig. 6.15(a) the whole spectral range is given. It includes the contribution from 5f Nd, La 5d, Sr 4d, Ni, and Mn 4sp that are positioned at higher energy (above 536eV) [39, 136]. The spectra have been normalized in the high-energy region at 550eV. However, we are more interested in the lower energy region below 536eV. This energy region is dominated by the hybridization between O 2p and TM 3d. The larger the intensity of the pre-peak, the larger the number of holes in O 2p due to electron transfer to the TM 3d. In other words, higher pre-peak intensity is a direct measure of the hybridization. Therefore in Fig. 6.15(b) we focus on this area. A peak A at 532.5eV can be assigned to Ni^{2+} contribution i.e. indication of charge transfer between Ni and Mn [137]. Peak A has a higher intensity in 5_15(NGO1), decreases in 5_15(LSMO12) and disappears in single film LSMO12. It might be explained by change in Mn^{4+} /Mn^{3+} ratio between LSMO12 and LSMO33.

Previous publications assign peak B at 528.9eV to Mn 3d e_g [138, 136]. Further

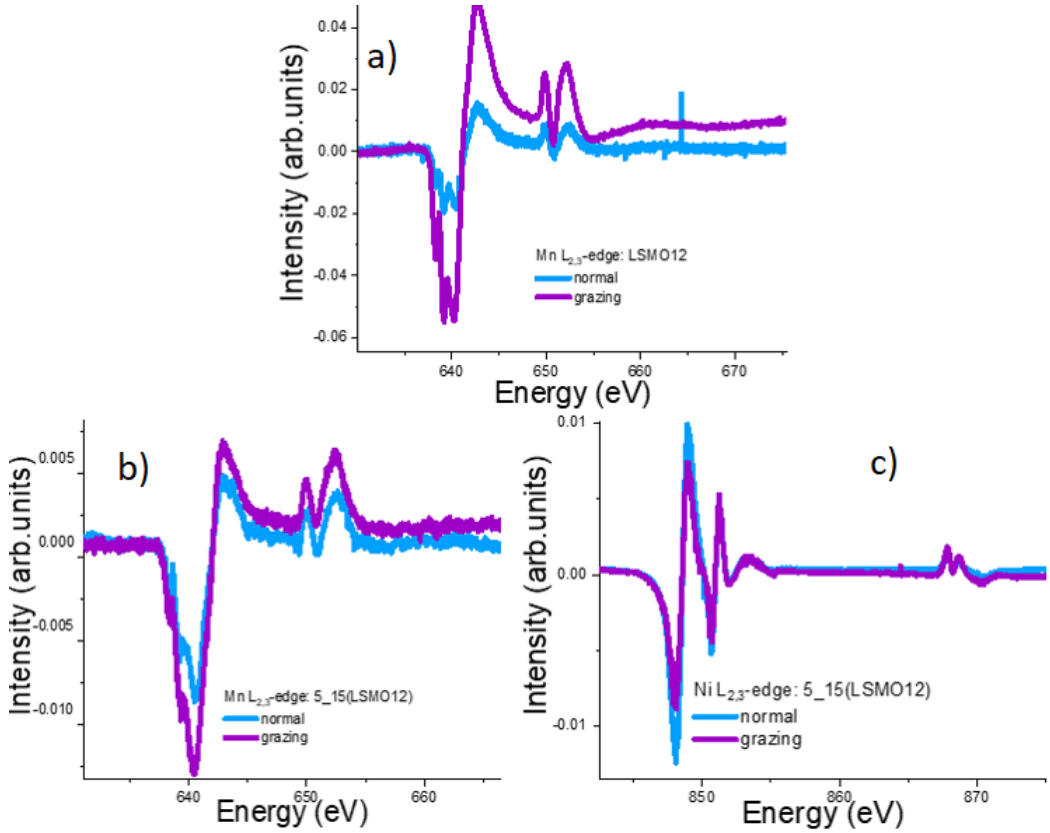

Figure 6.16: XMCD spectra measured in normal and grazing a) in 0.05T applied at Mn $L_{2,3}$-edge for LSMO12 single film; in remanence for 5_15(LSMO12) at b) Mn $L_{2,3}$-edge and c) Ni $L_{2,3}$-edge. All the spectra were taken at T=25K after saturation at 6.5T.

contribution at 531eV might attribute to Mn t_{2g}, however, it could intermix with Ni^{3+} states. Surprisingly, we find no visible evidence of the peak B in 5_15(LSMO12). Although it might be simply hidden by strong pre-peak at 527.7eV. This peak denoted as C is attributed to nickel ions with a formal oxidation state of Ni^{3+} hybridizing with O 2p orbitals [139]. Pre-peak C in 5_15(LSMO12) resembles the spectral shape of the pre-peak typical for NNO bulk. On the other hand, the lower intensity of peak C in 5_15(NGO1) was previously seen in LSMO33/$LaNiO_3$ heterostructure with some presence of interfacial charge transfer [138].

6.3.2 Magnetic properties probed by XMCD

Here, we conduct a detailed XMCD study to gain more information on Ni-Mn magnetic coupling, when both (NNO and LSMO) layers are insulating.

First, we checked what is the magnetic easy axis for NNO/LSMO12 heterostructure. As is shown in Fig. 6.16(a,b) both single layer and 5_15(LSMO12) have a larger intensity of Mn XMCD measured in grazing geometry. LSMO12 single film was measured in a

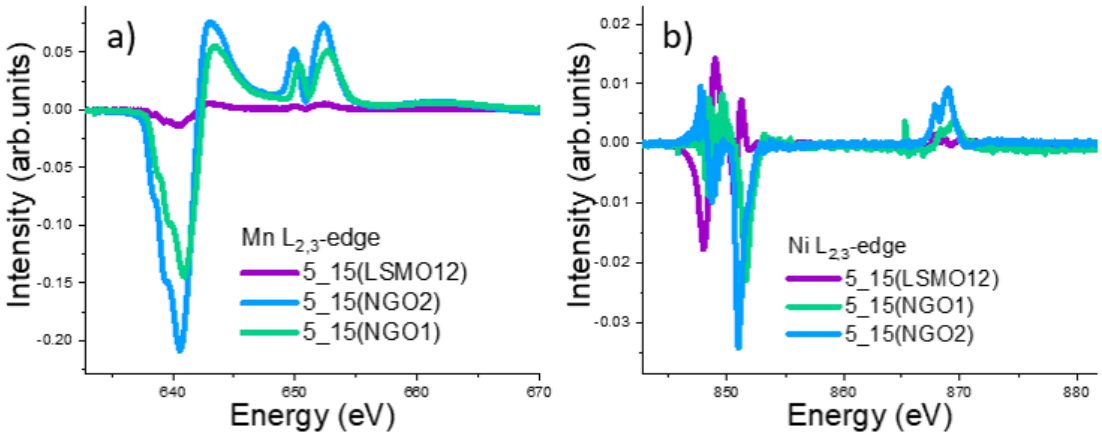

Figure 6.17: Comparison of remanent XMCD spectra between 5_15(LSMO12), 5_15(NGO1) and 5_15(NGO2)at a) Mn $L_{2,3}$-edge and b) Ni $L_{2,3}$-edge. All spectra are taken in grazing geometry at T=25K after saturation in 6.5T.

50mT field to improve the quality of the measurements. The Ni magnetic moment in NNO on top of LSMO12 has been found barely measurable with L_3 edge suffering from noise caused by La M_5 (Fig. 6.16(c)). As expected single layer and in bilayers LSMO12 on NGO has the same direction of the magnetic easy axis as in LSMO33. Thus, all XMCD data presented from now on was measured in grazing geometry.

Fig. 6.17 demonstrates a XMCD comparison between samples with 5uc NNO with different LSMO doping from different rounds of preparation measured in remanence after zero-field cooling at 25K. In addition to the ferromagnetic signal (Mn L_3 is negative), we can see a large decrease in remanent XMCD intensity at the Mn edge for 5_15(LSMO12) (Fig. 6.17(a)). At Ni edge the XMCD intensity on 5uc with LSMO12 is already extremely weak, therefore we did not measure it on 10uc NNO (Fig. 6.17(b)). It could be interpreted as Ni moments being completely disordered or Ni being in the AF phase that cannot be detected by XMCD.

The study on magnetism can be further extended by adding hysteresis loops measured in the same conditions as XMCD data. Fig. 6.18(a,b) shows magnetization curves. Fig. 6.18(a) presents a rectangular hysteresis loop of 5_15(LSMO12) on Mn L_3 edge typical for ferromagnets. The saturation at Mn edge is as high as for 5_15(NGO1) and 5_15(NGO2) by comparing Fig. 6.18(a), Fig. 6.1(b) and Fig. 6.10(a). It can be also clearly seen from saturated XMCD data shown in Fig. 6.18(a,inset) comparing all samples. The Ni 5_15(LSMO12) hysteresis displays s-like shape in Fig. 6.18(b) with very high saturation fields. There is still measurable remanence indicating a small ferromagnetic component but it is much smaller than in other cases. The loop does not look FM, so probably the

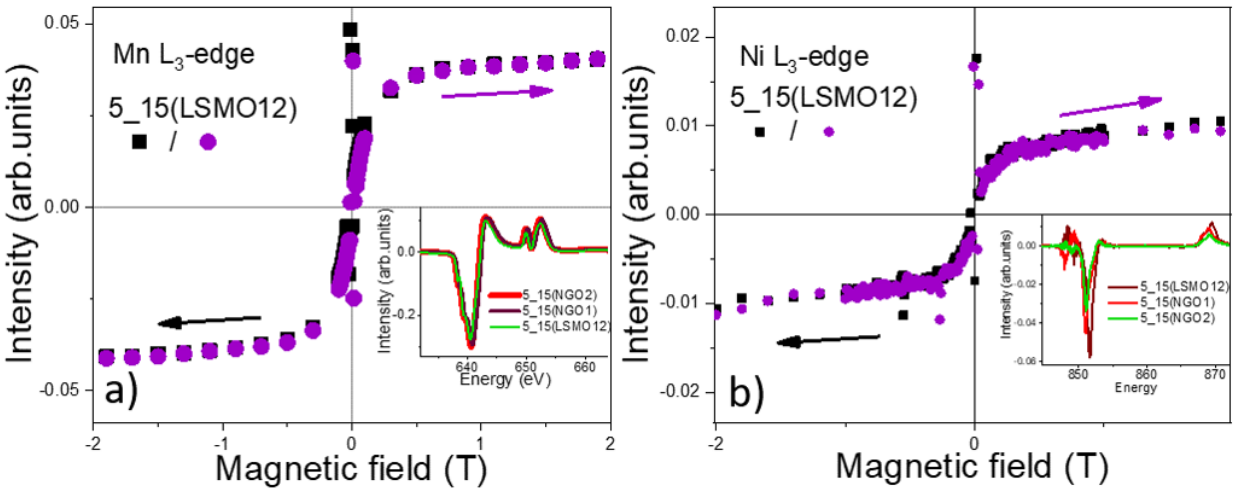

Figure 6.18: Magnetization curves measured on 5_15(LSMO12) a) at Mn edge b) at Ni edge. All spectra are taken in grazing geometry after zero-field cooling at T=25K. Inset: corresponding XMCD spectra recorded at 6.5T compared to similar spectra measured on 5_15(NGO1) and 5_15(NGO2).

largest component is PM or superparamagnetic. Saturated Ni XMCD meaured at 6.5T XMCD for 5uc NNO as a function of LSMO doping is also plotted in Fig. 6.18(b,inset) highlighting the difference in Ni magnetism between the samples: the saturated XMCD from sample 5_15(LSMO12) is twice smaller than sample 5_15(NGO1) and 5_15(NGO2).

XMCD sum rules analysis is particularly challenging for very insulating samples due to background instability. Therefore, it was only possible for 5_15(LSMO12) at Mn edge. Here, we use data in 6.5T at 25K after zero-field cooling. The number of holes was used as 5.5 reflecting lower Mn^{4+} content in LSMO12. The total magnetic moment was found to be $3\mu_B \pm 0.3$ against $3.5\mu_B$ for 5_15(NGO1). Sum rule analysis was not applied for Ni, because the moment was found to be very small and the quality of the data does not allow a reliable quantification due to background instability.

Now we have a closer look at Mn XMCD in samples with LSMO12 and different thicknesses of the NNO layer as a function of temperature. In Fig. 6.19(a) Mn XMCD L_3-edge intensity is plotted to provide information on the evolution of Mn magnetic moment. All data were measured in a 50mT field after zero-field cooling to be able to compare single layer data with the bilayers. The Mn moment of LSMO12 decreases with increasing temperature as expected for ferromagnetic compounds and vanishes at 120K. This temperature is lower than T_C of the bulk LSMO12 (200K) probably due to film thickness. Mn magnetism linearly drops over the whole temperature range. A different picture is seen for the bilayers. Both 5uc and 10uc show increasing Mn moment with increasing temperature. Mn moment in 10_15(LSMO12) reaches its maximum value at 60K for and

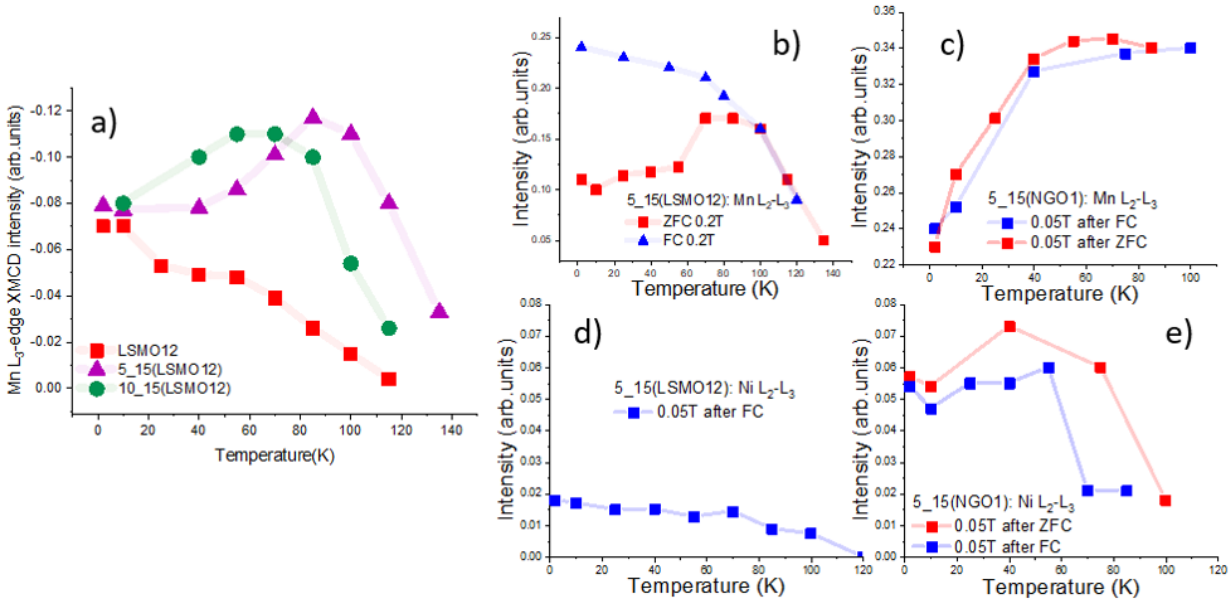

Figure 6.19: a) Comparison of Mn L_3 intensity as a function of temperature and NNO layer thickness under LSMO12. All spectra are taken in grazing geometry after zero-field cooling, with 0.05T applied after saturation in 6.5T. The L_2-L_3 difference versus temperature measured after zero-field cooling (red) and cooling in 0.2T field (blue) on 5_15(LSMO12) and 5_15(NGO1) at b,c) Mn edge and d,e) Ni edge respectively.

5_15(LSMO12) reaches the maximum at 85K. Higher in temperature Mn moment goes down to zero at 140K for 5_15(LSMO12) and at 120K for 10_15(LSMO12). Considering smaller overall Mn moment in LSMO12 compared to the bilayers and increased T_C of 5_15(LSMO12) we see that magnetic properties were improved in the bilayer. Additionally, abnormal dependence of Mn moment as a function of temperature in the bilayers occurs as a clear sign of complex magnetic texture at the interface with NNO. NNO capping layer could help to enhance magnetism in LSMO12 bilayers compared to a single layer below T_N of NNO and MIT. However, once NNO crosses T_N and becomes insulating and AF, Mn moment decreases with temperature. Surprisingly, this moment decrease happens at lower temperature in 10uc than in 5 uc NNO, even though T_N is supposed to be higher in thicker NNO film.

Furthermore, we have a look at the comparison of magnetization between 5_15(LSMO12) and 5_15(NGO1) measured in different field-cooling settings. 5_15(NGO1) was chosen for further investigation due to the presence of low temperature deep in magnetic moment. Previously, in Fig. 6.19(a) we demonstrated zero-field cooled magnetization curves. In Fig. 6.19(b,c) Mn L_2-L_3 XMCD is plotted as a function of temperature measured in two different settings: zero-field cooled (ZFC) and 0.2T field cooled (FC). 6.5T FC (not shown

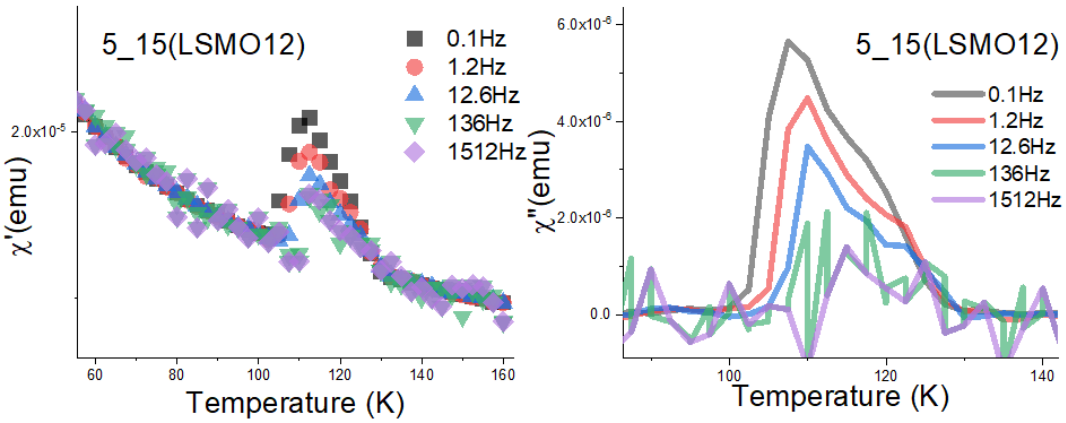

Figure 6.20: AC susceptibility measurements for 5_15(LSMO12) showing (left) χ' and (right) χ'' as a function of temperature and applied frequency.

here) was also measured and we found no difference in magnetic behaviour with 0.2T FC. 5_15(NGO1) has a similar behaviour no matter what is the magnetic field used for cooling (Fig. 6.19(b)). The decrease in magnetization at low temperature observed for Mn and Ni does not change if the sample is FC or ZFC, while for 5_15(LSMO12) the behaviour is very different as seen in Fig. 6.19(c). This shows that the magnetization decrease at low temperature for Mn 5_15(LSMO12) could be due to frustration of Mn magnetic moments at the interface in a so-called spin-glass state by analogy to other manganite systems [140]. In order to test this hypothesis we have measured AC susceptibility for 5_15(LSMO12). Measurements were carried out in 500 Oe applied field using five frequencies. From Fig. 6.20(left) in a plot for χ'' we see the peak at 112K. In Fig. 6.20(right) for the χ'' value, we see a shift in the peak position that indicates spin-glass states in LSMO12 [140].

By FC the 5_15(LSMO12) film in magnetic field the XMCD signal at Ni edge becomes measurable. Fig. 6.20 shows the measurement of the Ni L_2-L_3 while warming up after FC. Fig. 6.20 indicates a big change in magnetic moment between bilayer with LSMO12 (Fig. 6.20(c)) and with LSMO33 layer (Fig. 6.20(d)). The Ni magnetic signal is three times smaller in 5_15(LSMO12) in comparison to 5_15(NGO1). It is a very important finding that might help to understand induced NNO magnetism because we clearly see Ni ferromagnetism decay in NNO depending on the metallicity of the LSMO layer.

In summary we observed very different magnetic behaviour on samples with LSMO doping variation. In order to understand better the differences seen by XMCD we also measured RXMR on 5_15(LSMO12), 5_15(NGO1) and 5_15(NGO2). These results are presented in the next section.

Table 6.2: Bulk densities for each layer and its conversion to mol*cm^{-3}.

elements/compounds	atomic mass (g*mol^{-1})	density (g*cm^{-3})	density (mol*cm^{-3})
C	12	2.3	0.189
H_2O	6	1	0.16
LSMO	45.3	6.5	0.143
NNO	50.2	7.6	0.15
NGO	52.4	7.57	0.144

6.3.3 RXMR study on magnetism

In this section we discuss reflectivity data and its fitting sample by sample starting with 5_15(LSMO12), then 5_15(NGO1) and we finish with 5_15(NGO2) sample. Every paragraph is organized as following: off-resonance data and its fit followed by on-resonance data at Mn and Ni L_3 edge. Off-resonant spectra were measured at room-temperature or at 10K without applied field. On-resonance data were measured at 10K after field-cooling at 0.2T in 0.2T saturation and their fitting. On-resonance reflectivity curves are complemented by an asymmetry ratio calculated as I^--I^+/I^-+I^+. As explained in Section 3.4, non-zero asymmetry at a low angle is an indication of magnetic moments aligned in the sample plane, while the high-angle signal is linked to out-of-plane contribution. In addition, if oscillations change their sign over the measured range, it is usually an indication of antiparallel spin alignment in the sample. DYNA [83] uses densities calculated as mol*cm^{-3}, therefore our conventional density in g*cm^{-3} for each compound needs to be converted to (density in g*cm^{-3})/(atomic mass averaged per atom in g*mol^{-1}). Bulk densities for each layer and their conversion are presented in Tab. 6.2. For better fit results a low-density layer of C or/and H_2O were added to represent the accumulation of dirt and ice on the top surface (that is more likely to occur at low temperature).

Table 6.3: Parameters of the off-resonance fit for 5_15(LSMO12) from Fig. 6.21.

layer	density [g/cm^3]	thickness [Å]	roughness [Å]
C	0.7	164.5	28.2
NNO	6.7	21.8	2.7
LSMO12	6.8	59	5.1
NGO	4.24	2984	3.1
NGO	7.6	-	-

We begin with 5_15(LSMO12) sample and its off-resonance reflectivity curve shown in Fig. 6.21 with the respective fitting parameters in Tab. 6.3. Before we discuss structural parameters, it should be pointed out that deviation of density by 30-40% from the bulk value is considered normal for thin films. We find a NNO density lower than bulk values

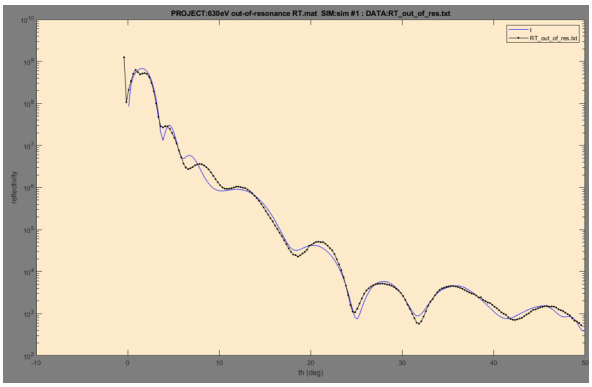

Figure 6.21: Experimental reflectivity curve (black) obtained at 630eV (off-resonant energy) at room-temperature on 5_15(LSMO12) and corresponding fit (blue).

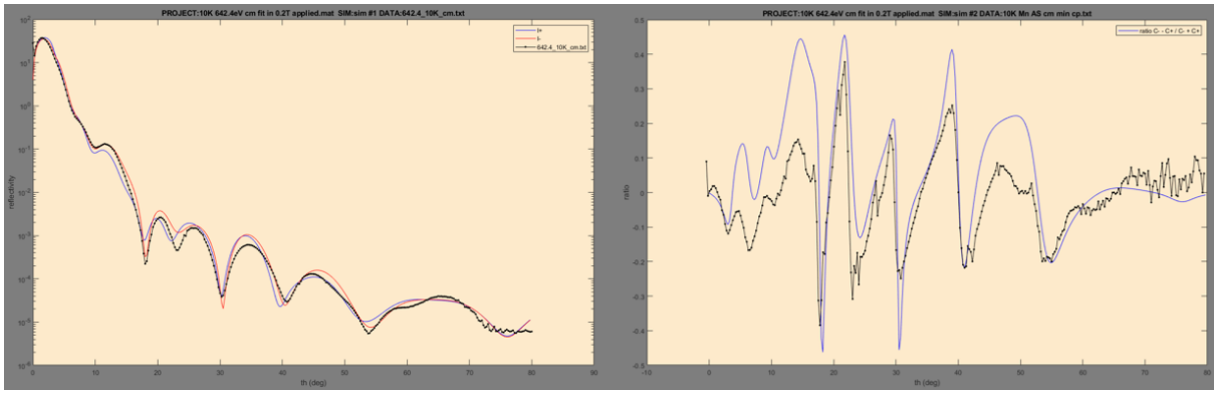

Figure 6.22: (left) Experimental resonant reflectivity curve (black) measured with c+ at Mn L_3 edge at T=10K on 5_15(LSMO12) and corresponding fit (blue), (right) experimental asymmetry ratio (black) and corresponding fit (blue).

by 12%. LSMO12 has a density that is very close to its bulk value. To improve the fit the density of the top part of the NGO substrate was decreased by 40% in comparison to the buried layers. Extracted roughness of each layer is between 2-5Åindicating a smooth interface.

The structural information obtained in the first step can be further used to fit the magnetic contribution of resonant data at low temperature. As a second step data sets measured at Ni and Mn L_3 edges at 10K were fitted. Fig. 6.22(left) and Fig. 6.23(left) shows the experimental reflectivity curve measured with c+ polarization and its fit, while asymmetry and its fit are shown in Fig. 6.22(right) and Fig. 6.23(right). Tab. 6.4 summarizes values of magnetic moments and angles for each layer. As it was defined before in Fig. 3.4, when ϕ and γ are at 90°, it means the moments are in the film plane. If the value of the magnetic moment is negative, it is equivalent to the rotation of the moment by 180° i.e. antiparallel alignment.

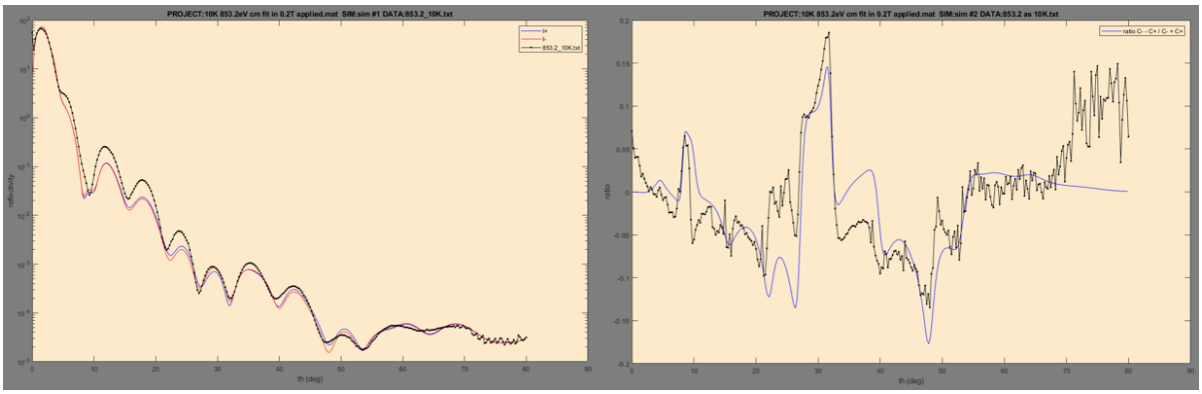

Figure 6.23: (left) Experimental resonant reflectivity curve (black) measured with c+ at Ni L_3 edge at T=10K on 5_15(LSMO12) and corresponding fit (blue), (right) experimental asymmetry ratio (black) and corresponding fit (blue).

Table 6.4: Parameters of Mn and Ni L_3 edge fit for 5_15(LSMO12) from Fig. 6.22 and 6.23.

layer	thickness [Å]	magnetic moment[μ_B]	ϕ[°]	γ[°]
NNO	3.4	0		
NNO	3.2	0		
NNO	5	0		
NNO	4	0		
NNO	4	0.2	90	90
LSMO12	6.2	2	90	70
LSMO12	3.4	2.5	90	80
LSMO12	7.3	3	90	90
LSMO12	14.9	3	90	90
LSMO12	28.8	3	90	90

There was only one magnetic atomic layer found in NNO at the interface with LSMO12 with a value of $0.2\mu_B$. Mn shows a reduction of the magnetic moment the closer it is to the interface with averaged magnetic moment value of $2.7\mu_B$ and a small tilt from the in-plane direction. Mn magnetic moment decrease is in agreement with the frustrated moments found by XMCD. Even though in FC we expect all Mn spins to be aligned, a small tilt can remain.

Next, we consider 5_15(NGO1) sample and its off-resonance reflectivity curve shown in Fig. 6.24 with the respective fitting parameters in Tab. 6.5. The best-fitting curve was achieved by dividing the LSMO33 layer into two parts: the top part being slightly denser than the bulk (by 4%) and the inner part being 8% less dense than the bulk. Moreover, NNO density was reduced by 33% from its bulk value. All densities are in very good agreement with their bulk values i.e. within the allowed deviation range. The

Table 6.5: Parameters of the off-resonance fit for 5_15(NGO1) from Fig. 6.24.

layer	density [g/cm^3]	thickness [Å]	roughness [Å]
NNO	5.22	15.3	4.0
LSMO33	6	37.7	3
LSMO33	6.8	22.2	0
NGO	7	20.9	1.7
NGO	7.6	-	-

density of the NGO top part was again decreased (by 8%) to improve fitting quality. This changes in density give a qualitative better agreement, but they are not correlated to other physics parameter. Extracted roughness 2-4Å of each layer between demonstrates smooth interfaces.

Ni and Mn L_3 edges at 10K were fitted in the next step. The results are shown in Fig. 6.25 and Fig. 6.26 with corresponding asymmetry and their fit. Tab. 6.6 summarizes values of magnetic moments and angles for each layer. The magnetic configuration seems to be more complex in this bilayer. An averaged magnetic moment of $2.4\mu_B$ Mn demonstrates some interfacial rotation and reduction of the magnetic moment. Interesting results were found for Ni. It seems to have antiferromagnetic ordering with an interfacial layer coupled antiparallel to Mn: negative oscillations in asymmetry at around 25° clearly show that. If we sum up magnetic moments from each layer and scale it by probing depth, we obtain a value that is close to the value obtained from XMCD (nearly $0.1\mu_B$). The antiparallel Ni layer at the interface probably causes the tilt of interfacial Mn spins by 10°.

Table 6.6: Parameters of Mn and Ni L_3 edge fit for 5_15(NGO1) from Fig. 6.25 and 6.26.

layer	thickness [Å]	magnetic moment[μ_B]	ϕ[°]	γ[°]
NNO	2	0.02	90	90
NNO	2	0.5	90	90
NNO	3.4	-0.4	90	90
NNO	3.2	0.7	90	90
NNO	2	-0.8	90	90
LSMO33	3	2.2	90	100
LSMO33	6.3	2	90	96
LSMO33	6.4	2.7	90	90
LSMO33	7.5	2.5	90	90
LSMO33	11.9	2.1	90	90
LSMO33	25.8	2.6	90	90

The last sample to be discussed is 5_15(NGO2). Its off-resonance reflectivity curve is shown in Fig. 6.27 with the respective fitting parameters in Tab. 6.7. All densities are in

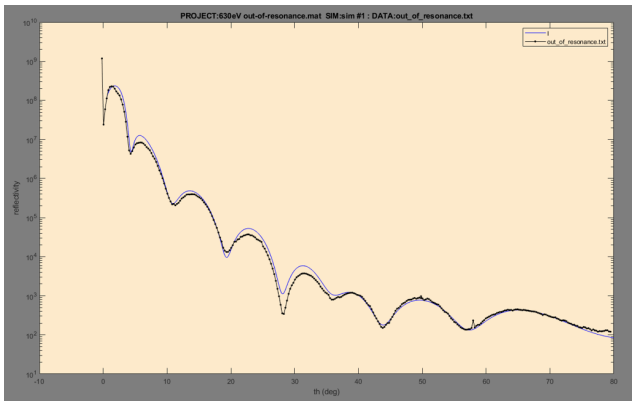

Figure 6.24: Experimental reflectivity curve (black) obtained at 630eV (off-resonant energy) at room-temperature on 5_15(NGO1) and corresponding fit (blue).

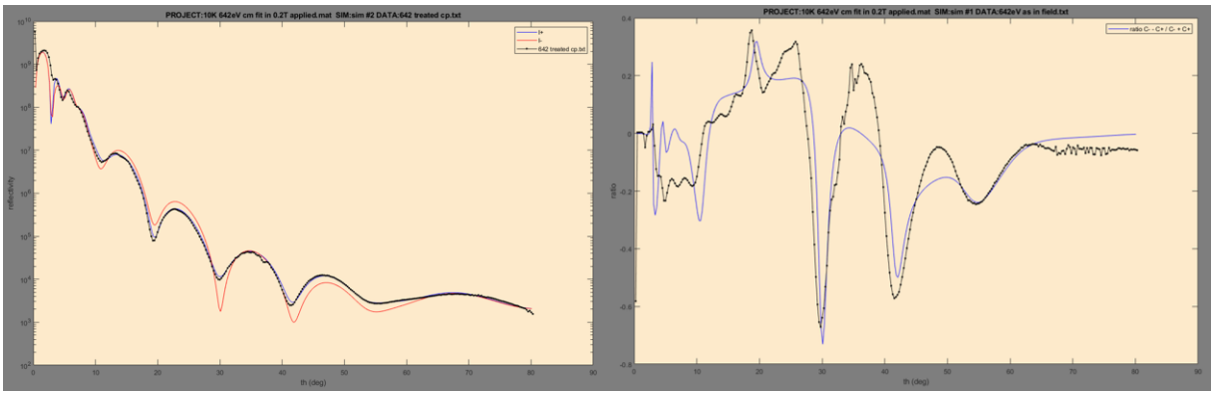

Figure 6.25: (left) Experimental resonant reflectivity curve (black) measured with c+ at Mn L_3 edge at T=10K on 5_15(NGO1) and corresponding fit (blue), (right) experimental asymmetry ratio (black) and corresponding fit (blue).

very good agreement with bulk values: LSMO33 density is lower than bulk by 10%, NNO density by 2%, and NGO top part by 17%. Extracted roughness of each layer varies in a range between 2-5Å. Off-resonance data were measured at low temperature, therefore in the fitting an additional layer of ice on the surface needed to be included.

Ni and Mn L_3 edges at 10K fit in the next step are shown in Fig. 6.28 and Fig. 6.29 with corresponding asymmetry and their fit. Tab. 6.8 summarizes values of magnetic moments and angles for each layer. The magnetic configuration of Mn seems to be similar to 5_15(NGO1). Despite the reduction at the interface, the rest of LSMO33 shows a stable value of a magnetic moment that is very close to the value we found from XMCD. However, Ni seems to behave differently. The negative oscillation at around 30° gives a hint that there is going to be some antiferromagnetic contribution. It is confirmed by fitting: Tab. 6.8 shows only one ferromagnetic layer at the interface with LSMO33, while the other two layers are aligned antiparallel to one another. If we again sum up the total

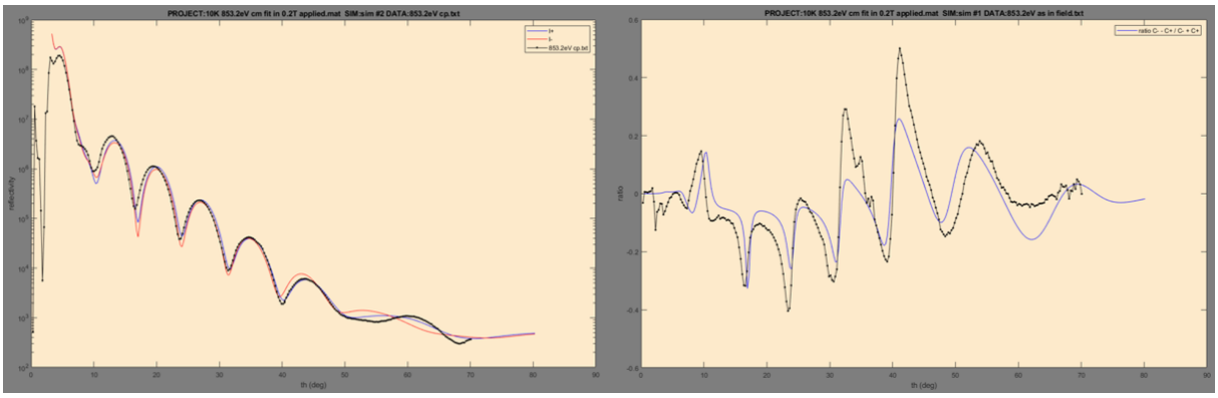

Figure 6.26: (left) Experimental resonant reflectivity curve (black) measured with c+ at Ni L_3 edge at T=10K on 5_15(NGO1) and corresponding fit (blue) (right) experimental asymmetry ratio (black) and corresponding fit (blue).

magnetic moment on Ni scaled by probing depth, we obtain $0.1\mu_B$ as expected from XMCD.

Table 6.7: Parameters of the off-resonance fit for 5_15(NGO2) from Fig. 6.27.

layer	density [g/cm^3]	thickness [Å]	roughness [Å]
H_2O	0.04	29.02	1
C	0.4	17.5	20
NNO	7.5	22.5	2.6
LSMO33	5.9	41.6	5
NGO	6.3	8333	4.1
NGO	7.6	-	-

Table 6.8: Parameters of Mn and Ni L_3 edge fit for 5_15(NGO2) from Fig. 6.28 and 6.29.

layer	thickness [Å]	magnetic moment[μ_B]	ϕ[°]	γ[°]
NNO	8.7	-0.06	90	90
NNO	6.5	0	90	90
NNO	5	-0.1	90	90
NNO	4	0.3	90	90
LSMO33	3.1	2.3	90	90
LSMO33	9	3.2	90	90
LSMO33	8.3	3.2	90	90
LSMO33	22	3.2	90	90

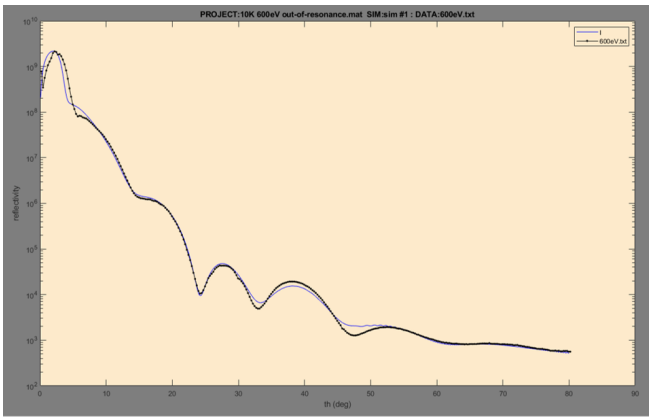

Figure 6.27: Experimental reflectivity curve (black) obtained at 630eV (off-resonant energy) at 10K on 5_15(NGO2) and corresponding fit (blue).

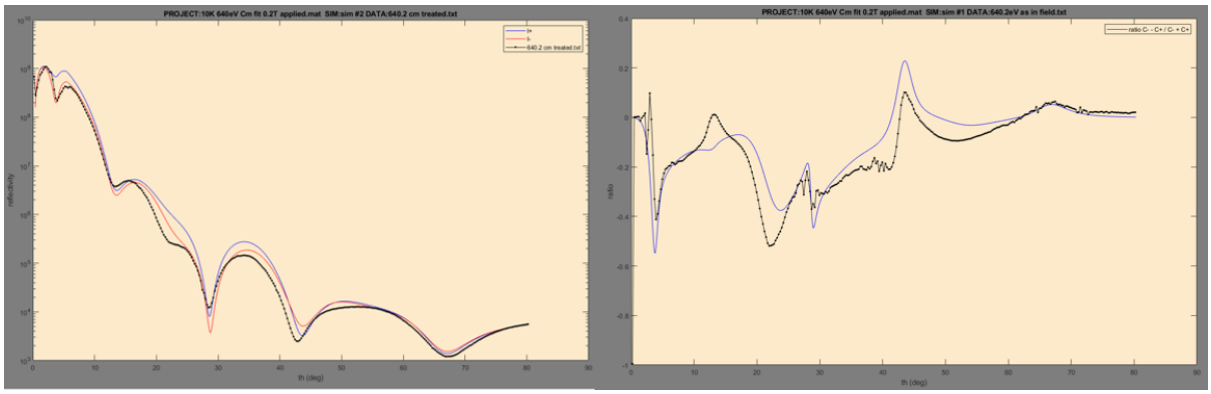

Figure 6.28: (left) Experimental resonant reflectivity curve (black) measured with c- at Mn L_3 edge at T=10K on 5_15(NGO2) and corresponding fit (blue), (right) experimental asymmetry ratio (black) and corresponding fit (blue).

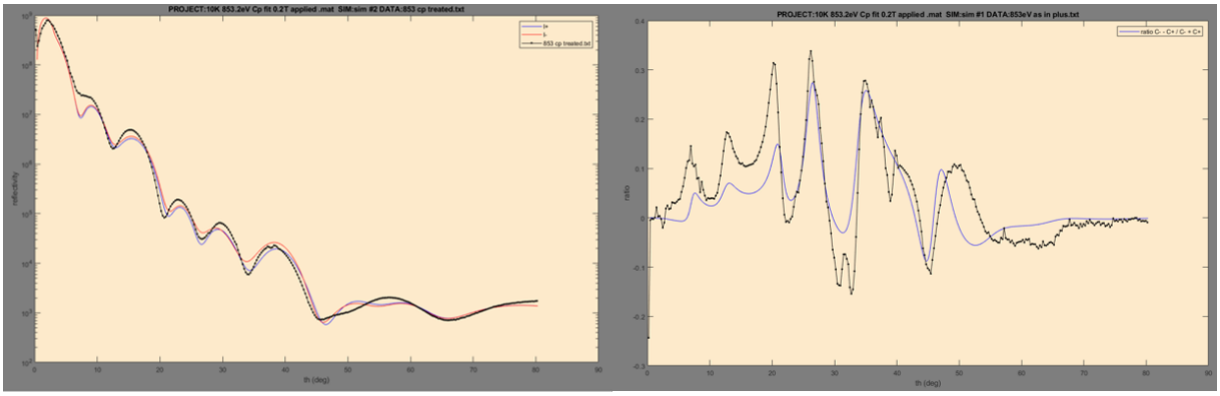

Figure 6.29: (left) Experimental resonant reflectivity curve (black) measured with c- at Ni L_3 edge at T=10K on 5_15(NGO2) and corresponding fit (blue), (right) experimental asymmetry ratio (black) and corresponding fit (blue).

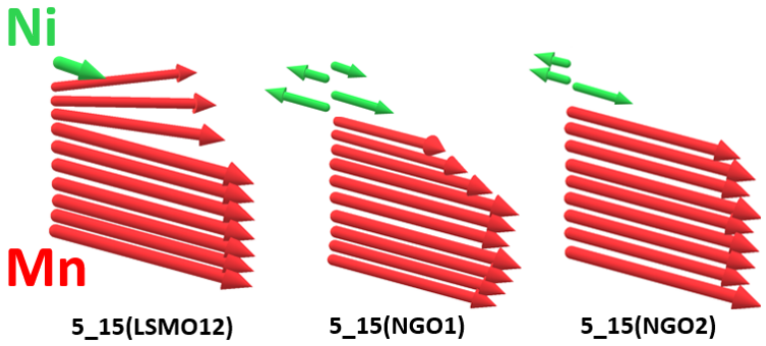

Figure 6.30: Schematic drawing of Ni and Mn magnetic moments using parameters from Tab. 6.4, 6.6 and 6.8.

6.3.4 Discussion

We have explored the effect of doping in LSMO/NNO heterostructure revealing major alternation in terms of magnetic and electronic reconstruction. As pointed out in [29, 38, 37] the magnetic moment per Mn atom in LSMO12 is expected to be 30% smaller than in LSMO33 single film. If NNO ferromagnetism is solely driven by LSMO magnetism, one would expect the reduction of magnetism on both Mn and Ni in the bilayers. We have shown vanishing magnetism in NNO in proximity to LSMO12 by neglectable XMCD signal in remanence and non-ferromagnetic hysteresis shape. Such a small remanent signal allows assuming NNO on top of LSMO12 is likely to be paramagnetic or antiferromagnetic in contrast to NNO on top of LSMO33 which is clearly ferromagnetic. Simultaneously, we have demonstrated LSMO12 to have slightly lower saturated magnetic moment than LSMO33 in the bilayers. Mn in LSMO12 possesses a saturated magnetic moment $3\mu_B$ in comparison to $3.5\mu_B$ value found for LSMO33. It allows to emphasize that LSMO magnetism is not the only driving force of emerged magnetism in NNO.

In Section 6.3, we discovered abnormal temperature behaviour for bilayers with LSMO12 when measured in ZFC settings. Since this effect disappeared when FC we suggest spin-glass-like behaviour of the Mn magnetic spins in LSMO12. Further, this suggestion was confirmed by AC susceptibility measurements. Since it was not observed in a single LSMO12 film, we could suggest interfacial interaction with NNO layer to govern Mn spin behaviour.

A systematic XA study was intended to probe the charge-transfer model of emerged magnetism in NNO. In the absence of charge transfer, we were able to detect a small difference in Mn XA spectra between a single film and the bilayer. It can be attributed to the valence gradient in LSMO12. Due to lower Mn^{4+} content than in LSMO33, LSMO12 naturally exhibits even lower charge transfer that is supported by O K-edge data.

Finally, we reconstructed the magnetic depth profile of samples with 5uc NNO deposited on NGO. From the structural point of view, we found abrupt interfaces and fine differences in terms of thicknesses. 5_15(NGO1) has 1uc less NNO than expected and 5_15(NGO2) has 5uc less LSMO than expected. This fine difference may result in slightly different magnetic behaviour due to the high sensitivity of our heterostructures. Furthermore, despite measured FM response by XMCD, RXMR results show that the coupling is not entirely FM. Different coupling schemes can be realized in the NNO/LSMO system as illustrated in the reconstructed magnetic profile for each sample shown in Fig. 6.30.

We have found Ni in 5_15(LSMO12) to couple ferromagnetically to Mn with $0.2\mu_B$ net magnetic moment on Ni found only at the interfacial 1uc layer. The rest of the NNO seems to be non-magnetic. However, there is a chance of NNO being truly AF. If the top layers of NNO are AF, it would give no XMCD signal in the absorption experiment or resonant reflectivity. Mn spins are aligned FM with 10° spin canting in the first 3uc at the interface. A small net moment on Ni and Mn spin canting might be a consequence of saturation in a 0.2T field: on NNO this field is enough to induce a small magnetic moment and, yet, it is not enough to fully saturate interfacial spin-glass Mn states.

From XMCD we expected AF component in NNO/LSMO33. We were able to detect AF spin alignment on NNO in both samples with LSMO33: 5_15(NGO1) and 5_15(NGO2). Only some of the Ni layers are coupled parallel to Mn. Most surprisingly, 5_15(NGO1) and 5_15(NGO2) reveal different coupling with the LSMO33 layer. In 5_15(NGO1) Ni is coupled AF to the Mn in the first layer and AF to the next Ni layer. It creates a collinear AF structure on NNO with a constant reduction of Ni moment from the bottom to the top. Due to that, we were able to measure uncompensated net ferromagnetic moment by XMCD. On the other hand, in 5_15(NGO2) Ni is coupled ferromagnetically to Mn in the first layer. Ni magnetic moment is concentrated in the interfacial 1uc layer with other NNO layers aligned antiparallel relative to LSMO33 and interfacial NNO layer.

Now let us discuss the LSMO33 behaviour in these samples. Both LSMO33 layers in 5_15(NGO1) and 5_15(NGO2) are aligned ferromagnetically. We found a higher saturated magnetic moment on 5_15(NGO2) ($3.1\mu_B$) in comparison to 5_15(NGO1) with an average of $2.4\mu_B$. It is in agreement with the XMCD, where at 10K we found a higher saturated magnetic moment on 5_15(NGO2). Moreover, we found 10° tilt in the interfacial layer of LSMO33 in 5_15(NGO1). It might occur due to competing FM and AF coupling taking place between Mn and Ni spins.

Great instability arises from competition between AF and FM orders at the NNO/LSMO interface. The study by Hepting *et al.* [134] revealed the possibility of collinear and non-collinear AF ordering in thin NNO films as a function of NNO thickness. From this work,

one can expect 5uc NNO to align as a collinear antiferromagnet. We also know that AF coupling between Ni planes in NNO is quite strong. On the other hand, there is the proximity of the ferromagnetic LSMO layer. By adding LSMO we create possibilities for different magnetic exchanges at the interface. Having both Mn^{3+} and Mn^{4+} enable ferromagnetic superexchange between Mn^{3+} and Ni^{3+}; and Mn^{4+} and Ni^{2+}. Contrastingly, Ni^{3+} and Mn^{4+} promote AF superexchange [141, 142]. Therefore, different types of exchange can act together to create complex magnetic structures in NNO/LSMO bilayers similar to $LaSrMn_{1-x}Ni_xO_3$, where different types of magnetic ordering: from AF to FM were realized as a function of Ni doping [142].

6.4 Conclusion

In Section 6.2 we have widely investigated magnetism and charge transfer of Ni in NNO/LSMO bilayer versus NNO thickness and strain. Our experimental results obtained by XMCD and XAS demonstrated the presence of Ni net ferromagnetic moment for 5uc and 10uc NNO in both strain states. The detected difference in magnetic properties between two NNO thicknesses could justify the FM phase of Ni to be located at the interface with LSMO33 without extending over the whole NNO layer. We found a remarkable enhancement of interfacial charge transfer between Ni and Mn in samples on LAO that can attribute to a larger Ni moment. Moreover, the samples on LAO show an out-of-plane easy axis and a large coercivity of 0.1T. Although we were able to measure Ni ferromagnetism in the samples on NGO, we claim AF interactions to be stabilized between Mn and Ni spins. It is supported by RXMR reconstruction of the magnetic depth-resolved profile presented in Section 6.3.

In Section 6.3, we have conducted a thorough study of the NNO/LSMO interface by different techniques as a function of LSMO doping. We found a spin-glass-like state on LSMO12 in the bilayers and weak ferromagnetic coupling at the interface between Mn and Ni.

We were able to manipulate Ni magnetic state and NNO electronic and magnetic properties by the structural disorder to accommodate the strain state and LSMO doping level. Our investigation demonstrates that coupling between NNO and LSMO can be tailored by small structural changes or external conditions such as temperature or magnetic field.

Summary

The aim of this thesis is to investigate magnetic properties of low dimensional complex system composed of TMOs. We have elucidated phenomena of induced magnetism in non-ferromagnetic TMOs by introducing them into the heterostructures. We present two systems, where we were able to tune magnetism by the proximity effects.

The first study is performed on $La_{0.7}Sr_{0.3}MnO_3/SrRuO_3$ system deposited on $SrTiO_3$ substrate that generates tensile strain on LSMO33. The study provides XMCD investigation of magnetism at Mn $L_{2,3}$ in the ultra-thin LSMO33 layer as a function of LSMO33 and SRO thickness; temperature and magnetic field. In contrast to LSMO33 single film that is already non-magnetic at 4uc, the magnetism of LSMO33 interfaced with the SRO layer is found to be restored. It occurs regardless of SRO thickness i.e. if the SRO layer is ferromagnetic metal or a non-magnetic insulator. Although if the SRO layer is magnetic, Mn spins at the interface can switch from AF to FM ordering due to interlayer coupling with SRO. It creates a spiral-like Mn spin arrangement that returns to a completely aligned with the field in the top layers if the LSMO33 layer is thick enough. Moreover, when SRO is magnetic, LSMO33 magnetism is preserved down to 2uc. If the SRO layer is below its critical thickness, LSMO33 orders ferromagnetically along the applied field direction.

To reason the origin of interface-related phenomena emerging ferromagnetism in ultra-thin manganites, we have conducted XLD experiments at Mn $L_{2,3}$ to single out the effect of orbital anisotropy. Such an effect has been predicted by DFT to have a major impact on magnetism stability in LSMO33/SRO structure [123]. XLD experiment and its simulation in CTM4XAS evidenced orbital reconstruction on LSMO33 in proximity to SRO layer from in-plane preferential occupation as expected purely from strain to out-of-plane similarly to DFT predictions. SRO modifies electronic levels of LSMO33 and lowers the energy of the out-of-plane orbital. Comparing orbital occupation of LSMO33 in ultra-thin limit with or without SRO layer, similar behaviour was found due to a strong dimensionality effect. As previously shown, out-of-plane orbital occupation on LSMO33 leads to C-type AF ordering in ultra-thin limit [113]. It does not occur in presence of the SRO layer, because it changes not only an orbital occupation but also affects charge transfer.

Valence change observed experimentally by Mn $L_{2,3}$ XA spectra in the ultra-thin single LSMO33 film in contrast to the bilayers allows us to assume that the SRO layer helps to maintain optimal Mn^{3+} /Mn^{4+} ratio in LSMO33 for the most effective ferromagnetic DE. We suggest that both effects originate from the more extended nature of Ru 4d orbitals in comparison to Ti 3d causing better hybridization with Mn 3d [126]. Results of the present work were published in [66].

The second study introduces AF/FM system composed of 5uc $NdNiO_3$ and 15uc $La_{0.7}Sr_{0.3}MnO_3$ deposited on $NdGaO_3$ substrate. In such a system, Ni is shown to have a net ferromagnetic moment measured by XMCD. This NNO magnetism was attributed to LSMO33 magnetism rather than charge transfer as seen from ARPES and XAS. Unexpectedly high conductivity was exhibited by electrical transport in this system in contrast to the low-temperature strong insulting phase expected. These results have been published in [19].

Single NNO film tends to have more Ni^{2+} on $LaAlO_3$ than on NGO [133] as also shown by our Ni $L_{2,3}$ XA spectra. This valence difference was associated with a more insulating phase in NNO films. Valence change towards Ni^{2+} and difference in resistance are resembled also in bilayers deposited on NGO and LAO. These effects have been attributed to structural distortion in different strain states by preferential orbital occupation and orbital occupancy; change of Ni-O-Ni angle and bond length in a single NNO [132, 133]. Consequently, in the bilayer, Mn-O-Ni distance and angle are also affected. If NGO substrate that generates tensile strain on NNO is replaced by LAO generating compressive strain, it results in reinforcement of FM phase in NNO. The investigation by XMCD exhibits twice larger Ni magnetic moment for compressed 5uc NNO on LSMO33 in comparison to tensile 5uc NNO on LSMO33. We suggest that this magnetism enhancement is caused by stronger charge transfer between Ni and Mn due to higher Ni^{2+} content when NNO is compressed. In turn, it helps to establish Mn^{4+} -Ni^{2+} ferromagnetic superexchange. We can deduce Ni FM ordering is a short-range effect by setting the thickness of the NNO layer to 10uc on top of 15uc LSMO33. The observed reduction of the XMCD signal could indicate that the FM alignment of the Ni spins does not extend over the whole NNO layer.

Further charge transfer suppression was evoked by the NNO interface with low-doped $La_{0.88}Sr_{0.12}MnO_3$ on NGO substrate. Insulator-insulator interface exhibits depression of interfacial magnetism on NNO unlike insulator-metal interface. No detected ferromagnetic signal at Ni $L_{2,3}$ may provide the evidence of recovered AF ordering on NNO. We have found exotic behaviour on LSMO12 in proximity to the NNO layer. Our Mn $L_{2,3}$ XMCD results suggest competing FM and AF coupling between Ni and Mn that probably causes spin-glass-like Mn behaviour in the interfacial layer. Resonant x-ray reflectivity

measurements and their fit enable accurate comparison between two coupling schemes: between NNO and LSMO33 or LSMO12 layers. Data and our simulation reveal a weak ferromagnetic coupling between Mn and Ni solely in 1uc in NNO/LSMO12. Such a coupling might be a consequence of a small applied field. On the other hand, antiparallel spin alignment between Ni and Mn was clearly seen at the NNO/LSMO33 interface. Our results suggest that the lack of interfacial charge transfer results in establishing antiferromagnetic superexchange between $Ni^{2+/3+}$ and $Mn^{3+/4+}$ for this system. This work is currently being prepared for publication.

Summarizing, in this thesis we addressed the origin of emerging ferromagnetism in non-ferromagnetic layer. By heterostructure engineering we were able to design different magnetic configurations. Our investigation highlights once more the importance of understanding interfacial physics ruling the magnetization appearance, its direction and strength.

Acknowledgements

I do not have enough words to express how grateful I am for these four years at PSI. I was lucky to experience this unique scientific environment, with its research excellence and very warm and friendly touch. I was very happy to be coming to work every single day (until COVID came) and enjoyed our countless group activities. Even in the time of the home office, our connection through Zoom kept me motivated and uplifted.

First of all, I would like to thank Dr. Cinthia Piamonteze for her supervision and for her time and patience invested in my PhD. She has shaped not only my research project but also me as a scientist. She taught me a lot about science, how to organize my work and most importantly how to look at things from different angles. Thank you Cinthia for your positive attitude and gentle coaching.

I am thankful to Prof. Dr. Frithjof Nolting for the guidance that I received from him along my PhD and for his readiness to help. I always enjoyed our meetings and looked forward to them. I would like to thank Prof. Dr. Martino Poggio for his part in my supervision.

I would like to express my gratitude to Dr. Urs Staub, Dr. Nazaret Ortiz Hernández and Dr. Elizabeth Skoropata for their fantastic support before, during and after our RESOXS experiments. It was not always going perfectly well, but every experiment taught me something very important.

I would also like to thank all MM group members and ex-members for the enjoyable time (both offline and online) spent together. Thank you for all the meetings, collaborations, beamtimes, coffee discussions, BBQ, fondue-in-the-forest and sports activities. It was a great privilege to work with you.

A special thanks to the SIS beamline team and its ex-members. They taught me so much about PLD and without the excellent samples we did together, my PhD wouldn't have happened. During meetings with Dr. Milan Radovic, one always learns a lot not only about physics but about the world. With support from Dr. Marco Caputo, I survived my first night shifts at X-treme beamline. I want also to thank Dr. Eduardo Guedes, who always had time to discuss or to grow one more tiny little sample quickly.

I would like to thank Dr. Jean-Marc Tonnerre who agreed to collaborate with me and

contributed a lot to my success of the reflectivity data fitting.

Finally, I would like to thank my family and especially my boyfriend Gaby for their generous support and for always believing in me.

List of Abbreviations

AF Antiferromagnetic

BF Bright field

DE Double exchange

DF Dark field

EDX Energy dispersive x-rays

FC Field cooled

FM Ferromagnetic

GKR Goodenough-Kanamori rule

LAO $LaAlO_3$

LSMO $La_{1-x}Sr_xMnO_3$

LSMO12 $La_{0.88}Sr_0.12MnO_3$

LSMO33 $La_{0.67}Sr_0.33MnO_3$

MIT Metal to insulator transition

NGO $NdGaO_3$

NNO $NdNiO_3$

PLD Pulsed laser deposition

PM Paramagnetic

RHEED Reflection high-energy electron diffraction

RSM Reciprocal Space Mapping

RXMR Resonant x-ray reflectivity

RXRR Resonant x-ray reflectivity

SE Superexchange

SRO $SrRuO_3$

STO $SrTiO_3$

TEM Transmission electron microscopy

TEY Total electron yield

TFY Total fluorescence yield

TMO Transition metal oxides

XAS X-ray absorption spectroscopy

XLD X-ray linear dichroism

XMCD X-ray magnetic circular dichroism

XRD X-ray diffraction

ZFC Zero-field cooled

List of Samples

The summary of the films composition with their respective names used in this thesis.

abbreviation	full name
n/m	n=2, 4, 8, 15uc LSMO33/m=0, 3, 20uc SRO//STO
5_15(NGO1)	5uc NNO/15uc LSMO33//NGO
LSMO33(NGO)	15uc LSMO33//NGO
5_15(NGO2)	5uc NNO/15uc LSMO33//NGO
10_15(NGO2)	10uc NNO/15uc LSMO33//NGO
5_15(LAO)	5uc NNO/15uc LSMO33//LAO
10_15(LAO)	10uc NNO/15uc LSMO33//LAO
LSMO33(LAO)	15uc LSMO33//LAO
5_15(LSMO12)	5uc NNO/15uc LSMO12//NGO
10_15(LSMO12)	10uc NNO/15uc LSMO12//NGO
LSMO12	15uc LSMO12//NGO

Curriculum Vitae

Full Name	Anna Zakharova
Date of Birth	April 22, 1994
Place of Birth	Yekaterinburg, Russia
Address	Zuercherstrasse 3, 5400 Baden, Switzerland

EDUCATION

- 2018-2022 **Doctoral Studies** at University of Basel (carried out at the Paul Scherrer Institute, Villigen). Supervised by Dr. Cinthia Piamonteze and Prof. Dr. Frithjof Nolting.
- 2016-2018 **Master of Science** in Physics, Saint-Petersburg State University, St. Pe- tersburg (Russia).
- 2012-2016 **Bachelor of Science** in Physics, Saint-Petersburg State University, St. Pe- tersburg (Russia).

CONFERENCE AND PRESENTATIONS

- Science and Progress — St. Petersburg, Russia (2016, poster presentation)
- PNPI Winter School in Condensed Matter Research — St. Petersburg, Russia (2017, poster presentation)
- SIN-NANO Summer School — Moscow, Russia (2017, poster, oral presentation)
- ILL ESRF Summer Undergraduate Program — Grenoble, France (2017, oral presentation)
- PSI Condensed Matter Retreat — Zurich, Switzerland (2018, poster presentation)

- Joint Annual Meeting of Swiss Physical Society and Austrian Physical Society — Zurich, Switzerland
- (2019, poster presentation)
- European School on Magnetism — Brno, Czech Republic (2019, poster presentation)
- Oxide Electronics School — Cargese, France (2019, poster presentation)
- The Joint European Magnetic Symposia — Online (2020, presentation)
- MANEP Mini-workshop on Oxides Heterostrustures – Online (2021, talk)

PUBLICATIONS

- J. Lumetzberger, V. Ney, **A. Zakharova**, D. Primetzhofer, K. Lenz, and A. Ney. Control of site occupancy by variation of the Zn and Al content in NiZnAl ferrite epitaxial films with low magnetic damping. *Phyical Review B*, 105(134412), 2022.
- **A. Zakharova**, M. Caputo, E. B. Guedes, M. Radovic, F. Nolting, and C. Piamonteze. Interplay between magnetism and interface-induced effects in ultrathin manganites. *Phyical Review Materials*, 5:124404, 2021.
- M. Caputo, Z. Ristic, R. Dhaka, T. Das, Z. Wang, C. Matt, N. Plumb, E. Guedes, J. Jandke, M. Naamneh, **A. Zakharova**, M. Medarde, M. Shi, L. Patthey, J. Mesot, C. Piamonteze, and M. Radovic. Proximity-induced novel ferromagnetism accompanied with resolute metallicity in $NdNiO_3$ heterostructure. *Advanced Science*, 8 (10), 2021.
- G. De Luca, J. Spring, U. Bashir, M. Campanini, R. Totani, C. Dominguez, **A. Zakharova**, M. Döbeli, T. Greber, M. D. Rossell, C. Piamonteze, and M. Gibert. Ferromagnetic insulating epitaxially strained La_2NiMnO_6 thin films grown by sputter deposition. *APL Materials*, 9, 081111, 2021.
- N. Ortiz Hernández, Z. Salman, T. Prokscha, A. Suter, J. R. L. Mardegan, S. Moser, **A. Zakharova**, C. Piamonteze, and U. Staub. Magnetic order of tetragonal CuO ultrathin films. *Phyical Review B*, 103 (224429), 2021.
- A.A. Mistonov, A.P. Chumakov, R.P. Ermakov, L.D. Iskhakova, **A.V. Zakharova**, A.V. Chumakova. K.O. Kvashnina. Electronic structure studies of bismuth compounds using high energy resolution X-ray spectroscopy and ab initio calculations. *Journal of Alloys Compounds*, 753 (646-654), 2018.

Bibliography

[1] S.Fusil, V.Garcia, A.Barthélémy, and M.Bibes. Magnetoelectric devices for spintronics. *Annual Review of Materials Research*, 44(1):91–116, 2014.

[2] G. A. Prinz. Magnetoelectronics. *Science*, 282(5394):1660–1663, 1998.

[3] J. Fabian I.Žutić and S.S.Das. Spintronics: Fundamentals and applications. *Reviews of Modern Physics*, 76:323–410, 2004.

[4] J.D. Hoffman, S. M. Wu, B.J. Kirby, and A. Bhattacharya. Tunable non-collinear antiferromagnetic resistive memory through oxide superlattice design. *Physical review applied*, 9:044041, 2018.

[5] A. Bhattacharya and S.J. May. Magnetic oxide heterostructures. *Annual Review of Materials Research*, 44(1):65–90, 2014.

[6] S.E. Barnes S. Ishihara W. Koshibae G. Khaliullin S. Maekawa, T. Tohyama. *Physics of Transition Metal Oxides*. Springer, 2004.

[7] D.I.Khomskii. *Transition Metal Compounds*. Cambridge University Press, 2014.

[8] A. Fujimori I. Masatoshi and Y. Tokura. Metal-insulator transitions. *Reviews of Modern Physics*, 70:1039–1263, 1998.

[9] H.-U. Habermeier. Thin films of perovskite-type complex oxides. *Materials Today*, 10(10):34–43, 2007.

[10] J.M.D. Coey, M. Viret, and S. von Molnár. Mixed-valence manganites. *Advances in Physics*, 58(6):571–697, 2009.

[11] J. Stöhr and H.C. Siegmann. *Magnetism: From Fundamentals to Nanoscale Dynamics*. Springer, 2006.

[12] F. Hellman, A. Hoffmann, Y. Tserkovnyak, G. S. D. Beach, E. E. Fullerton, C. Leighton, A. H. MacDonald, D. C. Ralph, D. A. Arena, H. A. Dürr, P. Fischer, J. Grollier, J. P. Heremans, T. Jungwirth, A. V. Kimel, B. Koopmans, I. N.

Krivorotov, S. J. May, A. K. Petford-Long, J. M. Rondinelli, Nitin Samarth, Ivan K. Schuller, Andrei N. Slavin, Mark D. Stiles, O. Tchernyshyov, A. Thiaville, and B. L. Zink. Interface-induced phenomena in magnetism. *Reviews of Modern Physics*, 89:025006, 2017.

[13] P. Zubko, S. Gariglio, M. Gabay, P. Ghosez, and J.-M. Triscone. Interface physics in complex oxide heterostructures. *Annual Review of Condensed Matter Physics*, 2(1):141–165, 2011.

[14] Y. Tokura and N. Nagaosa. Orbital physics in transition-metal oxides. *Science*, 288(5465):462–468, 2000.

[15] X. Zhai, L. Cheng, Y. Liu, C. Schlepütz, S. Dong, L. Hui, Z. Xiaoqiang, S. Chu, L. Zheng, J. Zhang, A. Bhattacharya J. N. Eckstein A. Zhao, H. Hong, and C. Zeng. Correlating interfacial octahedral rotations with magnetism in $(LaMnO_{3+\delta})_n/(SrTiO_3)_n$ superlattices. *Nature communications*, 5:4283, 2014.

[16] P. Yu, J.-S. Lee, S. Okamoto, M. D. Rossell, M. Huijben, C.-H. Yang, Q. He, J. X. Zhang, S. Y. Yang, M. J. Lee, Q. M. Ramasse, R. Erni, Y.-H. Chu, D. A. Arena, C.-C. Kao, L. W. Martin, and R. Ramesh. Interface ferromagnetism and orbital reconstruction in $BiFeO_3-La_{0.7}Sr_{0.3}MnO_3$ heterostructures. *Physical Review Letters*, 105:027201, 2010.

[17] A. V. Boris, Y. Matiks, E. Benckiser, A. Frano, P. Popovich, V. Hinkov, P. Wochner, M. Castro-Colin, E. Detemple, and V. K. Malik et al. Dimensionality control of electronic phase transitions in nickel-oxide superlattices. *Science*, 332(6032):937–940, 2011.

[18] A. Frano, E. Schierle, M. W. Haverkort, Y. Lu, M. Wu, S. Blanco-Canosa, U. Nwankwo, A. V. Boris, P. Wochner, G. Cristiani, and Habermeier. Orbital control of noncollinear magnetic order in nickel oxide heterostructures. *Physical Review Letters*, 111:106804, 2013.

[19] M. Caputo, Z. Ristic, R. Dhaka, T. Das, Z. Wang, C. Matt, N. Plumb, E. Guedes, J. Jandke, M. Naamneh, A. Zakharova, M. Medarde, M. Shi, L. Patthey, J. Mesot, C. Piamonteze, and M. Radovic. Proximity-induced novel ferromagnetism accompanied with resolute metallicity in $NdNiO_3$ heterostructure. *Advanced Science*, 8, 10 2021.

[20] A. M. F. Pereira. *Ordering Phenomena in Transition-Metal-Oxide Heterostructures.* PhD thesis, Technischen Universtit¨at Berlin, 2014.

[21] A. J. Freeman and R. E. Watson. Theory of direct exchange in ferromagnetism. *Physical Review*, 124:1439–1454, 1961.

[22] C. Zener. Interaction between the d-shells in the transition metals. ii. ferromagnetic compounds of manganese with perovskite structure. *Physical Review*, 82:403–405, 1951.

[23] H.A Kramers. L'interaction entre les atomes magnétogènes dans un cristal paramagnétique. *Physica*, 1(1):182–192, 1934.

[24] J. B. Goodenough. Theory of the role of covalence in the perovskite-type manganites $[\mathrm{La, M(II)}]\mathrm{MnO_3}$. *Physical Review*, 100:564–573, 1955.

[25] J. B. Goodenough and A. L. Loeb. Theory of ionic ordering, crystal distortion, and magnetic exchange due to covalent forces in spinels. *Physical Review*, 98:391–408, 1955.

[26] J. Kanamori. Theory of the Magnetic Properties of Ferrous and Cobaltous Oxides, I. *Progress of Theoretical Physics*, 17(2):177–196, 1957.

[27] P. W. Anderson. Antiferromagnetism. theory of superexchange interaction. *Physical Review*, 79:350–356, 1950.

[28] P. Bruno. *Physical Origins and Theoretical Models of Magnetic Anisotropy*. 1993.

[29] J. Hemberger, A. Krimmel, T. Kurz, H.-A. Krug von Nidda, V. Yu. Ivanov, A. A. Mukhin, A. M. Balbashov, and A. Loidl. Structural, magnetic, and electrical properties of single-crystalline $\mathrm{La_{1-x}Sr_xMnO_3}$ ($0.4 < x < 0.85$). *Physical Review B*, 66:094410, 2002.

[30] A. Urushibara, Y. Moritomo, T. Arima, A. Asamitsu, G. Kido, and Y. Tokura. Insulator-metal transition and giant magnetoresistance in $\mathrm{La_{1-x}Sr_xMnO_3}$. *Physical Review B*, 51:14103–14109, 1995.

[31] A. Vailionis, H. Boschker, W. Siemons, E. P. Houwman, D. H. A. Blank, G. Rijnders, and G. Koster. Misfit strain accommodation in epitaxial $\mathrm{ABO_3}$ perovskites: Lattice rotations and lattice modulations. *Physical Review B*, 83:064101, 2011.

[32] Z. Bukowski R. Dybzinski P. W. Klamut J. E. Siewenie O. Chmaissem J. Shaffer C. W. Kimball J. D. Jorgensen B. Dabrowski, X. Xiong and S. Short. Structure–properties phase diagram for $\mathrm{La_{1-x}Sr_xMnO_3}$ ($0.1 \leq x \leq 0.2$). *Physical Review B*, 60:7006, 1999.

[33] H. Kawano, R. Kajimoto, M. Kubota, and H. Yoshizawa. Ferromagnetism-induced reentrant structural transition and phase diagram of the lightly doped insulator $La_{1-x}Sr_xMnO_3(x \leq 0.17)$. *Physical Review B*, 53, 1996.

[34] Y. Endoh, K. Hirota, S. Ishihara, S. Okamoto, Y. Murakami, A. Nishizawa, T. Fukuda, H. Kimura, H. Nojiri, K. Kaneko, and S. Maekawa. Transition between two ferromagnetic states driven by orbital ordering in $La_{0.88}Sr_{0.12}MnO_3$. *Physical Review Letters*, 82:4328–4331, 1999.

[35] S. Uhlenbruck, R. Teipen, R. Klingeler, B. Büchner, O. Friedt, M. Hücker, H. Kierspel, T. Niemöller, L. Pinsard, A. Revcolevschi, and R. Gross. Interplay between charge order, magnetism, and structure in $La_{0.875}Sr_{0.125}MnO_3$. *Physical Review Letters*, 82:185–188, 1999.

[36] S. Grenier, K. J. Thomas, J. P. Hill, U. Staub, Y. Bodenthin, M. García-Fernández, V. Scagnoli, V. Kiryukhin, S-W. Cheong, B. G. Kim, and J.-M. Tonnerre. Direct observation of oxygen superstructures in manganites. *Physical Review Letters*, 99:206403, 2007.

[37] Y. Feng, K.-J. Jin, L. Gu, X. He, C. Ge, Q.-h. Zhang, M. He, Q.-l. Guo, Q. Wan, M. he, H.-b. Lu, and G. Yang. Insulating phase at low temperature in ultrathin la0.8sr0.2mno3 films. *Scientific Reports*, 6:22382, 2016.

[38] Y. Kim, S. Ryu, and H. Jeen. Strain-effected physical properties of ferromagnetic insulating $La_{0.88}Sr_{0.12}MnO_3$ thin films. *RSC Advances*, 9:2645–2649, 2019.

[39] J. Liu, M. Kargarian, M. Kareev, B. Gray, P. J. Ryan, A. Cruz, N. Tahir, Y.-D. Chuang, J. Guo, J. M. Rondinelli, J. W. Freeland, G. A. Fiete, and J. Chakhalian. Heterointerface engineered electronic and magnetic phases of $NdNiO_3$ thin films. *Nature Communications*, 4(1), 2013.

[40] M. Ziese, I. Vrejoiu, and D. Hesse. Structural symmetry and magnetocrystalline anisotropy of $SrRuO_3$ films on $SrTiO_3$. *Physical Review B*, 81:184418, 2010.

[41] D. J. Singh. Electronic and magnetic properties of the 4d itinerant ferromagnet $SrRuO_3$. *Journal of Applied Physics*, 79:2645–2649, 1996.

[42] N. Hiraoka, M. Itou, A. Deb, Y. Sakurai, Y. Kakutani, A. Koizumi, N. Sakai, S. Uzuhara, S. Miyaki, H. Koizumi, K. Makoshi, N. Kikugawa, and Y. Maeno. Ru−O orbital hybridization and orbital occupation in $SrRuO_3$: A magnetic compton-profile study. *Physical Review B*, 70:054420, 2004.

[43] E. B. Guedes, M. Abbate, K. Ishigami, A. Fujimori, K. Yoshimatsu, H. Kumigashira, M. Oshima, F. C. Vicentin, P. T. Fonseca, and R. J. O. Mossanek. Core level and valence band spectroscopy of $SrRuO_3$: Electron correlation and covalence effects. *Physical Review B*, 86:235127, 2012.

[44] K. Ishigami, K. Yoshimatsu, D. Toyota, M. Takizawa, T. Yoshida, G. Shibata, T. Harano, Y. Takahashi, T. Kadono, V. K. Verma, V. R. Singh, Y. Takeda, T. Okane, Y. Saitoh, H. Yamagami, T. Koide, M. Oshima, H. Kumigashira, and A. Fujimori. Thickness-dependent magnetic properties and strain-induced orbital magnetic moment in $SrRuO_3$ thin films. *Phys. Rev. B*, 92:064402, 2015.

[45] S. Kang, Y. Tseng, B. H. Kim, S. Yun, B. Sohn, B. Kim, D. McNally, E. Paris, C. H. Kim, C. Kim, T. W. Noh, S. Ishihara, T. Schmitt, and J.-G. Park. Orbital-selective confinement effect of Ru $4d$ orbitals in $SrRuO_3$ ultrathin film. *Physical Review B*, 99:045113, 2019.

[46] H. Jeong, S. G. Jeong, A. Y. Mohamed, M. Lee, W.-S. Noh, Y. Kim, J.-S. Bae, W. S. Choi, and D.-Y. Cho. Thickness-dependent orbital hybridization in ultrathin $SrRuO_3$ epitaxial films. *Applied Physics Letters*, 115(9):092906, 2019.

[47] Y. J. Chang, . H. Kim, S.-H. Phark, Y. S. Kim, J. Yu, and T. W. Noh. Fundamental thickness limit of itinerant ferromagnetic $SrRuO_3$ thin films. *Physical Review Letters*, 103:057201, 2009.

[48] A. J. Grutter, F. J. Wong, E. Arenholz, A. Vailionis, and Y. Suzuki. Evidence of high-spin ru and universal magnetic anisotropy in $SrRuO_3$ thin films. *Physical Review B*, 85:134429, 2012.

[49] S. Catalano, M. Gibert, J. Fowlie, J. Íñiguez, J.-M. Triscone, and J. Kreisel. Rare-earth nickelates $RNiO_3$: thin films and heterostructures. *Reports on Progress in Physics*, 81(4):046501, 2018.

[50] J. Chaloupka and G. Khaliullin. Orbital order and possible superconductivity in $LaNiO_3/LaMO_3$ superlattices. *Physical Review Letters*, 100:016404, 2008.

[51] U. Staub, G. I. Meijer, F. Fauth, R. Allenspach, J. G. Bednorz, J. Karpinski, S. M. Kazakov, L. Paolasini, and F. d'Acapito. Direct observation of charge order in an epitaxial $NdNiO_3$ film. *Physical Review Letters*, 88:126402, 2002.

[52] I. I. Mazin, D. I. Khomskii, R. Lengsdorf, J. A. Alonso, W. G. Marshall, R. M. Ibberson, A. Podlesnyak, M. J. Martínez-Lope, and M. M. Abd-Elmeguid. Charge

ordering as alternative to jahn-teller distortion. *Physical Review Letters*, 98:176406, 2007.

[53] J. L. García-Muñoz, M. A. G. Aranda, J. A. Alonso, and M. J. Martínez-Lope. Structure and charge order in the antiferromagnetic band-insulating phase of $NdNiO_3$. *Physical Review B*, 79:134432, 2009.

[54] V. Scagnoli, U. Staub, A. M. Mulders, M. Janousch, G. I. Meijer, G. Hammerl, J. M. Tonnerre, and N. Stojic. Role of magnetic and orbital ordering at the metal-insulator transition in $ndnio_3$. *Physical Review B*, 73:100409, 2006.

[55] H. Park, A. J. Millis, and C. A. Marianetti. Site-selective mott transition in rare-earth-element nickelates. *Physical Review Letters*, 109:156402, 2012.

[56] M. L. Medarde. Structural, magnetic and electronic properties of perovskites $RNiO_3$ (R = rare earth). *Journal of Physics: Condensed Matter*, 9(8):1679–1707, 1997.

[57] S. Middey, J. Chakhalian, P. Mahadevan, J.W. Freeland, A.J. Millis, and D.D. Sarma. Physics of ultrathin films and heterostructures of rare-earth nickelates. *Annual Review of Materials Research*, 46(1):305–334, 2016.

[58] R. S. Dhaka, Tanmoy Das, N. C. Plumb, Z. Ristic, W. Kong, C. E. Matt, N. Xu, Kapildeb Dolui, E. Razzoli, M. Medarde, L. Patthey, M. Shi, M. Radović, and Joël Mesot. Tuning the metal-insulator transition in $NdNiO_3$ heterostructures via fermi surface instability and spin fluctuations. *Physical Review B*, 92:035127, 2015.

[59] Haverkort M. W. Brück S. Goering E. Macke S. Frañó A. Yang X. Andersen O. K. Cristiani G. Habermeier H. U. Boris A. V. Zegkinoglou I. Wochner P. Kim H. J. Hinkov V. Keimer B Benckiser, E. Orbital reflectometry of oxide heterostructures. *Nature materials*, 10:189–193, 2011.

[60] M. Wu, E. Benckiser, M. W. Haverkort, A. Frano, Y. Lu, U. Nwankwo, S. Brück, P. Audehm, E. Goering, S. Macke, V. Hinkov, P. Wochner, G. Christiani, S. Heinze, G. Logvenov, H.-U. Habermeier, and B. Keimer. Strain and composition dependence of orbital polarization in nickel oxide superlattices. *Physical Review B*, 88:125124, 2013.

[61] M. Haverkort. *Spin and orbital degrees of freedom in transition metal oxides and oxide thin films studied by soft x-ray absorption spectroscopy*. PhD thesis, Universität zu Köln, 2005.

[62] B. T. Thole, G. van der Laan, and G. A. Sawatzky. Strong magnetic dichroism predicted in the $M_{4,5}$ x-ray absorption spectra of magnetic rare-earth materials. *Physical Review Letters*, 55:2086–2088, 1985.

[63] G. van der Laan, B. T. Thole, G. A. Sawatzky, J. B. Goedkoop, J. C. Fuggle, J.-M. Esteva, R. Karnatak, J. P. Remeika, and H. A. Dabkowska. Experimental proof of magnetic x-ray dichroism. *Physical Review B*, 34:6529–6531, 1986.

[64] F. De Groot. Core level spectroscopy of solids. 2008.

[65] F. De Groot. Multiplet effects in x-ray spectroscopy. *Coordination chemistry reviews*, 249:31–63, 2005.

[66] A. Zakharova, M. Caputo, E. B. Guedes, M. Radovic, F. Nolting, and C. Piamonteze. Interplay between magnetism and interface-induced effects in ultrathin manganites. *Physical Review Materials*, 5:124404, 2021.

[67] E. Stavitski and F. M.F. de Groot. The CTM4XAS program for EELS and XAS spectral shape analysis of transition metal L edges. *Micron*, 41(7):687–694, 2010.

[68] G. van der Laan and A. I. Figueroa. X-ray magnetic circular dichroism—a versatile tool to study magnetism. *Coordination Chemistry Reviews*, 277-278:95–129, 2014. Following Chemical Structures using Synchrotron Radiation.

[69] G. Schütz, W. Wagner, W. Wilhelm, P. Kienle, R. Zeller, R. Frahm, and G. Materlik. Absorption of circularly polarized x-rays in iron. *Physical Review Letters*, 58:737–740, 1987.

[70] J. Stöhr. X-ray magnetic circular dichroism spectroscopy of transition metal thin films. *Journal of Electron Spectroscopy and Related Phenomena*, 75:253–272, 1995. Future Perspectives for Electron Spectroscopy with Synchrotron Radiation.

[71] P. Carra, B. T. Thole, M. Altarelli, and X. Wang. X-ray circular dichroism and local magnetic fields. *Physical Review Letters*, 70:694–697, 1993.

[72] B. T. Thole, P. Carra, F. Sette, and G. van der Laan. X-ray circular dichroism as a probe of orbital magnetization. *Physical Review Letters*, 68:1943–1946, Mar 1992.

[73] C. T. Chen, Y. U. Idzerda, H.-J. Lin, N. V. Smith, G. Meigs, E. Chaban, G. H. Ho, E. Pellegrin, and F. Sette. Experimental confirmation of the x-ray magnetic circular dichroism sum rules for iron and cobalt. *Physical Review Letters*, 75:152–155, 1995.

[74] J. P. Crocombette, B.T. Thole, and F. Jollet. The importance of the magnetic dipole term in magneto-circular x-ray absorption dichroism for 3d transition metal compounds. *Journal of Physics: Condensed Matter*, 8(22):4095–4105, 1996.

[75] C. Piamonteze, P. Miedema, and F. M. F. de Groot. Accuracy of the spin sum rule in XMCD for the transition-metal L edges from manganese to copper. *Physical Review B*, 80:184410, 2009.

[76] S. Macke and E. Goering. Magnetic reflectometry of heterostructures. *Journal of Physics: Condensed Matter*, 26(36):363201, 2014.

[77] M. Born, E. Wolf, A. B. Bhatia, P. C. Clemmow, D. Gabor, A. R. Stokes, A. M. Taylor, P. A. Wayman, and W. L. Wilcock. *Principles of Optics: Electromagnetic Theory of Propagation, Interference and Diffraction of Light*. Cambridge University Press, 1999.

[78] E. Hecht. *Optics*. Addison-Wesley, 2002.

[79] L. G. Parratt. Surface studies of solids by total reflection of x-rays. *Physical Review*, 95:359–369, 1954.

[80] J. P. Hannon, G. T. Trammell, M. Blume, and D. Gibbs. X-ray resonance exchange scattering. *Physical Review Letters*, 61:1245–1248, 1988.

[81] C. T. Chantler. Detailed tabulation of atomic form factors, photoelectric absorption and scattering cross section, and mass attenuation coefficients in the vicinity of absorption edges in the soft x-ray ($Z = 30$–$36, Z = 60$–$89, E = 0.1$keV–10keV), addressing convergence issues of earlier work. *Journal of Physical and Chemical Reference Data*, 29(4):597–1056, 2000.

[82] S. Grenier E. Jal, N. Jaouen. How to use dyna, a matricial formalism to analyze x-ray magnetic reflectivity curves. `http://dyna.neel.cnrs.fr/wp-content/uploads/2020/09/Tuto_DYNA_XRMR_2018-09.pdf`.

[83] M. Elzo, E. Jal, O. Bunău, S. Grenier, Y. Joly, A. Ramos, H. Tolentino, J.-M. Tonnerre, and N. Jaouen. X-ray resonant magnetic reflectivity of stratified magnetic structures: Eigenwave formalism and application to a W/Fe/W trilayer. *Journal of Magnetism and Magnetic Materials*, 324:105–112, 2012.

[84] A. Ruosi, C. Raisch, A. Verna, R. Werner, B. A. Davidson, J. Fujii, R. Kleiner, and D. Koelle. Electron sampling depth and saturation effects in perovskite films

investigated by soft x-ray absorption spectroscopy. *Physical Review B*, 90:125120, 2014.

[85] J. Jaklevic, J.A. Kirby, M.P. Klein, A.S. Robertson, G.S. Brown, and P. Eisenberger. Fluorescence detection of exafs: Sensitivity enhancement for dilute species and thin films. *Solid State Communications*, 23(9):679–682, 1977.

[86] R. Nakajima, J. Stöhr, and Y. U. Idzerda. Electron-yield saturation effects in l-edge x-ray magnetic circular dichroism spectra of fe, co, and ni. *Physical Review B*, 59:6421–6429, 1999.

[87] K. Amemiya. Sub-nm resolution depth profiling of the chemical state and magnetic structure of thin films by a depth-resolved x-ray absorption spectroscopy technique. *Physical Chemistry Chemical Physics*, 14:10477–10484, 2012.

[88] S. Eisebitt, T. Böske, J.-E. Rubensson, and W. Eberhardt. Determination of absorption coefficients for concentrated samples by fluorescence detection. *Physical Review B*, 47:14103–14109, 1993.

[89] C. Piamonteze, U. Flechsig, S. Rusponi, J. Dreiser, J. Heidler, M. Schmidt, R. Wetter, M. Calvi, T. Schmidt, H. Pruchova Blaettler, J. Krempaský, C. Quitmann, H. Brune, and F. Nolting. X-treme beamline at sls: X-ray magnetic circular and linear dichroism at high field and low temperature. *Journal of synchrotron radiation*, 19:661–74, 2012.

[90] N. Ortiz Hernandez. *Investigation of strongly correlated electron systems with resonant X-ray scattering techniques*. PhD thesis, ETH Zurich, 2021.

[91] U. Staub, V. Scagnoli, Y. Bodenthin, M. García-Fernández, R. Wetter, A. Mulders, H. Grimmer, and M. Horisberger. Polarization analysis in soft x-ray diffraction to study magnetic and orbital ordering. *Journal of synchrotron radiation*, 15:469–76, 2008.

[92] R. Eason, S. Barrington, C. Grivas, T. May-Smith, and D. Shepherd. *Pulsed Laser Deposition of Thin Films: Applications-Led Growth of Functional Materials*, pages 383–420. 03 2006.

[93] J. Vijayakumar. *Artificial multiferroic heterostructures: Magnetoelectric coupling and dynamics*. PhD thesis, Basel University, 2019.

[94] S. Das. *Growth of* $La_{2x}Sr_xCuO_4/La_{2/3}Ca_{1/3}MnO_3$ *superlattices and characterization of their structural, electronic and magnetic properties*. PhD thesis, University of Fribourg, 2014.

[95] J. Als-Nielsen. *Elements of Modern X-Ray Physics*, volume 55. 01 2002.

[96] M. Birkholz, P. Fewster, and C. Genzel. *Thin Film Analysis by X-ray Scattering*, volume 58. 2005.

[97] D. Pesquera. *Strain and interface-induced charge, orbital and spin orderings in transition-metal oxide perovskites*. PhD thesis, Universidad Autónoma de Barcelona, 2014.

[98] E. Muller. *TEM Primer*. 2021.

[99] D. Williams and C. Carter. *Transmission Electron Microscopy: A Textbook for Materials Science*, volume III. 2009.

[100] M. Buchner, K. Höfler, B. Henne, V. Ney, and A. Ney. Tutorial: Basic principles, limits of detection, and pitfalls of highly sensitive squid magnetometry for nanomagnetism and spintronics. *Journal of Applied Physics*, 124(16):161101, 2018.

[101] M. McElfresh. Fundamentals of magnetism and magnetic measurements featuring quantum design's magnetic property measurement system. *Quantum Design*, 11578, 1994.

[102] M. Bibes, Ll. Balcells, S. Valencia, J. Fontcuberta, M. Wojcik, E. Jedryka, and S. Nadolski. Nanoscale multiphase separation at $La_{2/3}Ca_{1/3}MnO_3/SrTiO_3$ interfaces. *Physical Review Letters*, 87:067210, 2001.

[103] M. Huijben, L. W. Martin, Y.-H. Chu, M. B. Holcomb, P. Yu, G. Rijnders, D. H. A. Blank, and R. Ramesh. Critical thickness and orbital ordering in ultrathin $La_{0.7}Sr_{0.3}MnO_3$ films. *Physical Review B*, 78:094413, 2008.

[104] L. Chen, Z. Wang, G. Wang, H. Guo, M. Saghayezhian, Z. Liao, Y. Zhu, E. W. Plummer, and J. Zhang. Surface and interface properties of $La_{2/3}Sr_{1/3}MnO_3$ thin films on $SrTiO_3$ (001). *Physical Review Materials*, 3:044407, 2019.

[105] M. Angeloni, G. Balestrino, N. G. Boggio, P. G. Medaglia, P. Orgiani, and A. Tebano. Suppression of the metal-insulator transition temperature in thin $La_{0.7}Sr_{0.3}MnO_3$ films. *Journal of Applied Physics*, 96(11):6387–6392, 2004.

[106] J. Z. Sun, D. W. Abraham, R. A. Rao, and C. B. Eom. Thickness-dependent magnetotransport in ultrathin manganite films. *Applied Physics Letters*, 74(20):3017–3019, 1999.

[107] H. Boschker, J. Kautz, E. P. Houwman, W. Siemons, D. H. A. Blank, M. Huijben, G. Koster, A. Vailionis, and G. Rijnders. High-temperature magnetic insulating phase in ultrathin $La_{0.7}Sr_{0.3}MnO_3$ films. *Physical Review Letters*, 109:157207, 2012.

[108] J.-S. Lee, D. A. Arena, P. Yu, C. S. Nelson, R. Fan, C. J. Kinane, S. Langridge, M. D. Rossell, R. Ramesh, and C.-C. Kao. Hidden magnetic configuration in epitaxial $La_{1-x}Sr_xMnO_3$ films. *Physical Review Letters*, 105:257204, 2010.

[109] N. Mottaghi, M. S. Seehra, R. Trappen, S. Kumari, C.-Y. Huang, S. Yousefi, G. B. Cabrera, A. H. Romero, and M. B. Holcomb. Insights into the magnetic dead layer in $La_{0.7}Sr_{0.3}MnO_3$ thin films from temperature, magnetic field and thickness dependence of their magnetization. *AIP Advances*, 8(5):056319, 2018.

[110] C. Aruta, G. Ghiringhelli, V. Bisogni, L. Braicovich, N. B. Brookes, A. Tebano, and G. Balestrino. Orbital occupation, atomic moments, and magnetic ordering at interfaces of manganite thin films. *Physical Review B*, 80:014431, 2009.

[111] A. Tebano, A. Orsini, P. G. Medaglia, D. Di Castro, G. Balestrino, B. Freelon, A. Bostwick, Young Jun Chang, G. Gaines, E. Rotenberg, and N. L. Saini. Preferential occupation of interface bands in $La_{2/3}Sr_{1/3}MnO_3$ films as seen via angle-resolved photoemission. *Physical Review B*, 82:214407, 2010.

[112] S. Valencia, L. Peña, Z. Konstantinovic, L. Balcells, R. Galceran, D. Schmitz, F. Sandiumenge, M. Casanove, and B. Martínez. Intrinsic antiferromagnetic/insulating phase at manganite surfaces and interfaces. *Journal of Physics: Condensed Matter*, 26(16):166001, 2014.

[113] A. Tebano, C. Aruta, S. Sanna, P. G. Medaglia, G. Balestrino, A. A. Sidorenko, R. De Renzi, G. Ghiringhelli, L. Braicovich, V. Bisogni, and N. B. Brookes. Evidence of orbital reconstruction at interfaces in ultrathin $La_{0.67}Sr_{0.63}MnO_3$ films. *Physical Review Letters*, 100:137401, 2008.

[114] Z. Liao, N. Gauquelin, R. J. Green, S. Macke, J. Gonnissen, S. Thomas, Z. Zhong, L. Li, L. Si, S. Van Aert, P. Hansmann, K. Held, J. Xia, J. Verbeeck, G. Van Tendeloo, G. A. Sawatzky, G. Koster, M. Huijben, and G. Rijnders. Thickness dependent properties in oxide heterostructures driven by structurally induced metal–oxygen hybridization variations. *Advanced Functional Materials*, 27(17):1606717, 2017.

[115] X. Li, I. Vrejoiu, M. Ziese, A. Gloter, and P. Aken. Impact of interfacial coupling of oxygen octahedra on ferromagnetic order in $La_{0.7}Sr_{0.3}MnO_3/SrTiO_3$ heterostructures. *Scientific Reports*, 7:40068, 2017.

[116] J.-S. Lee, D. A. Arena, T. S. Santos, C. S. Nelson, S. I. Hyun, J. H. Shim, and C.-C. Kao. Controlling competing interactions at oxide interfaces: Enhanced anisotropy in $La_{0.7}Sr_{0.3}MnO_3$ films via interface engineering. *Physical Review B*, 85:235125, 2012.

[117] D. Pesquera, G. Herranz, A. Barla, E. Pellegrin, F. Bondino, E. Magnano, and F. Sanchez. Surface symmetry-breaking and strain effects on orbital occupancy in transition metal perovskite epitaxial films. *Nature communications*, 3:1189, 2012.

[118] C. Piamonteze, F. Bern, S.R V. Avula, M. Studniarek, C. Autieri, M. Ziese, and I. Lindfors-Vrejoiu. Ferromagnetic order of ultra-thin $La_{0.7}Ba_{0.3}MnO_3$ sandwiched between $SrRuO_3$ layers. *Applied Physics Letters*, 118(15):152408, 2021.

[119] M. Ziese, I. Vrejoiu, E. Pippel, P. Esquinazi, D. Hesse, C. Etz, J. Henk, A. Ernst, I. V. Maznichenko, W. Hergert, and I. Mertig. Tailoring magnetic interlayer coupling in $La_{0.7}Sr_{0.3}MnO_3/SrRuO_3$ superlattices. *Physical Review Letters*, 104:167203, 2010.

[120] F. Bern, M. Ziese, I. Vrejoiu, X. Li, and P. A. van Aken. Magnetic and magneto-transport properties of ultrathin $La_{0.7}Ba_{0.3}MnO_3$ films embedded in SrRuO. *New Journal of Physics*, 18(5):053021, 2016.

[121] M. Ziese, F. Bern, E. Pippel, D. Hesse, and I. Vrejoiu. Stabilization of ferromagnetic order in $La_{0.7}Sr_{0.3}MnO_3$-SrRuO superlattices. *Nano letters*, 12:4276–81, 2012.

[122] Y. Lee, B. Caes, and B.N. Harmon. Role of oxygen 2p states for anti-ferromagnetic interfacial coupling and positive exchange bias of ferromagnetic LSMO/SRO bilayers. *Journal of Alloys and Compounds*, 450(1):1–6, 2008.

[123] K. Lv, H. P. Zhu, W. Q. Zou, F. M. Zhang, and X. S. Wu. Charge transfer and orbital reconstruction in the $(La_{0.7}Sr_{0.3}MnO_3)m/(SrRuO_3)n$ superlattices. *Journal of Applied Physics*, 117(18):185305, 2015.

[124] R. Herger, P. R. Willmott, C. M. Schlepütz, M. Björck, S. A. Pauli, D. Martoccia, B. D. Patterson, D. Kumah, R. Clarke, Y. Yacoby, and M. Döbeli. Structure determination of monolayer-by-monolayer grown $La_{1-x}Sr_xMnO_3$ thin films and the onset of magnetoresistance. *Physical Review B*, 77:085401, 2008.

[125] J. Heidler, C. Piamonteze, R. V. Chopdekar, M. A. Uribe-Laverde, A. Alberca, M. Buzzi, A. Uldry, B. Delley, C. Bernhard, and F. Nolting. Manipulating magnetism in $La_{0.7}Sr_{0.3}MnO_3$ via piezostrain. *Physical Review B*, 91:024406, 2015.

[126] J. Garcia-Barriocanal, J.C. Cezar, F. Bruno, P. Thakur, N.B. Brookes, C. Utfeld, A. Rivera-Calzada, S.R. Giblin, J. Taylor, J. Duffy, S. Dugdale, T. Nakamura, K. Kodama, C. Leon, S. Okamoto, and J. Santamaria. Spin and orbital Ti magnetism at $LaMnO_3/SrTiO_3$ interfaces. *Nature communications*, 1:82, 2010.

[127] X. Ning, Z. Wang, and Z. Zhang. Fermi level shifting, charge transfer and induced magnetic coupling at $La_{0.7}Ca_{0.3}MnO_3/LaNiO_3$ interface. *Scientific Reports*, 5:8460, 2015.

[128] J. Peng, C. Song, F. Li, B. Cui, H. Mao, Y. Wang, G. Wang, and F. Pan. Charge transfer and orbital reconstruction in strain-engineered $(La, Sr)MnO_3/LaNiO_3$ heterostructures. *ACS Applied Materials & Interfaces*, 7(32):17700–17706, 2015.

[129] R. Scherwitzl, P. Zubko, I. G. Lezama, S. Ono, A. F. Morpurgo, G. Catalan, and J.-M. Triscone. Electric-field control of the metal-insulator transition in ultrathin $NdNiO_3$ films. *Advanced Materials*, 22(48):5517–5520, 2010.

[130] C. Piamonteze, Y. Windsor, S. Avula, E. Kirk, and U. Staub. Soft x-ray absorption of thin films detected using substrate luminescence: a performance analysis. *Journal of Synchrotron Radiation*, 27:1289–1296, 09 2020.

[131] K. Chen, C. Luo, B. B. Chen, R. M. Abrudan, G. Koster, S. K. Mishra, and F. Radu. Charge-transfer-induced interfacial ferromagnetism in $La_{0.7}Sr_{0.3}MnO_3/NdNiO_3$. *Physical Review Materials*, 4:054408, 2020.

[132] L. Wang, S. Ju, L. You, Y. Qi, Y. Guo, P. Ren, Y. Zhou, and J. Wang. Competition between strain and dimensionality effects on the electronic phase transitions in $NdNiO_3$. *Scientific Reports*, 5:18707, 2015.

[133] J. Shi, Y. Zhou, and S. Ramanathan. Colossal resistance switching and band gap modulation in a perovskite nickelate by electron doping. *Nature communications*, 5:4860, 2014.

[134] M. Hepting, R. Green, Z. Zhong, M. Bluschke, E. Suyolcu, S. Macke, A. Frano, S. Catalano, M. Gibert, R. Sutarto, F. He, G. Cristani, G. Logvenov, Y. Wang, P. Aken, P. Hansmann, M. Le Tacon, J.-M. Triscone, G. Sawatzky, and E. Benckiser. Complex magnetic order in nickelate slabs. *Nature Physics*, 2019.

[135] C. Piamonteze, F. M. F. de Groot, H. C. N. Tolentino, A. Y. Ramos, N. E. Massa, J. A. Alonso, and M. J. Martínez-Lope. Spin-orbit-induced mixed-spin ground state in $RNiO_3$ perovskites probed by x-ray absorption spectroscopy: Insight into the metal-to-insulator transition. *Physical Review B*, 71:020406, 2005.

[136] A. Galdi, C. Aruta, P. Orgiani, C. Adamo, V. Bisogni, N. B. Brookes, G. Ghiringhelli, D. G. Schlom, P. Thakur, and L. Maritato. Electronic band redistribution probed by oxygen absorption spectra of $(SrMnO_3)_n(LaMnO_3)_{2n}$ superlattices. *Physical Review B*, 85:125129, 2012.

[137] G. Zhou, Y. Bai, Z.-Y. Quan, F. Jiang, W. Liu, Y. Xu, S. Dhesi, and X. Xu. Robust interfacial exchange bias and metal-insulator transition influenced by the $LaNiO_3$ layer thickness in $La_{0.7}Sr_{0.3}MnO_3/LaNiO_3$ superlattices. *ACS Applied Materials Interfaces*, 9, 2017.

[138] G. Fabbris, N. Jaouen, D. Meyers, J. Feng, J. D. Hoffman, R. Sutarto, S. G. Chiuzbăian, A. Bhattacharya, and M. P. M. Dean. Emergent *c*-axis magnetic helix in manganite-nickelate superlattices. *Physical Review B*, 98:180401, 2018.

[139] S. Wang, X. Dash, M. Yu, J. Breese, A. Wang, N. Palina, L. Wang, S. Dash, X. Yu, M. Breese, J. Wang, and A. Rusydi. Investigation of the metal-insulator transition in $NdNiO_3$ films by site-selective x-ray absorption spectroscopy. *Nanoscale*, 9, 2017.

[140] N. Mottaghi, M. S. Seehra, J. Shi, M. Jain, and M. B. Holcomb. Spin dynamics and relaxation in 7.6 nm thin film of $La_{0.7}Sr_{0.3}MnO_3/SrTiO_3$: ac magnetic susceptibility and magnetic viscosity investigations. *Journal of Applied Physics*, 128(7):073903, 2020.

[141] R. I. Dass, J.-Q. Yan, and J. B. Goodenough. Oxygen stoichiometry, ferromagnetism, and transport properties of $La_{2-x}NiMnO_{6+\delta}$. *Physical Review B*, 68:064415, 2003.

[142] T. F. Creel, J. Yang, M.t Kahveci, S. K. Malik, S. Quezado, O. A. Pringle, W. B. Yelon, and W. J. James. Structural and magnetic properties of $La_{0.7}Sr_{0.3}Mn_{1-x}Ni_xO_3$ ($x \leq 0.4$). *Journal of Applied Physics*, 114(1):013911, 2013.